Direct Numerical Simulation of Bubbly Flows and Interfacial Dynamics of Phase Transitions

A Dissertation Presented

by

Tianshi Lu

to

The Graduate School in Partial Fulfillment of the Requirements for the

Degree of

Doctor of Philosophy

in

Applied Mathematics and Statistics

Stony Brook University

August 2005

Stony Brook University

The Graduate School

Tianshi Lu

We, the dissertation committee for the above candidate for the Doctor of
Philosophy degree, hereby recommend acceptance of this dissertation.

James Glimm
Advisor
Department of Applied Mathematics and Statistics

Xiaolin Li
Chairman
Department of Applied Mathematics and Statistics

Yongmin Zhang
Member
Department of Applied Mathematics and Statistics

Roman Samulyak
Outside Member
Brookhaven National Laboratory
Center for Scientific Computing

This dissertation is accepted by the Graduate School.

Graduate School

Abstract of the Dissertation

Direct Numerical Simulation of Bubbly Flows and Interfacial Dynamics of Phase Transitions

by

Tianshi Lu

Doctor of Philosophy

in

Applied Mathematics and Statistics

Stony Brook University

2005

We studied the propagation of acoustic and shock waves in bubbly fluids using the Front Tracking hydrodynamic simulation code FronTier for axisymmetric flows. We compared the simulation results with the theoretical predictions and the experimental data. The method was applied to an engineering problem on the mitigation of cavitation erosion in the container of the Spallation Neutron Source liquid mercury target. The simulation of the pressure wave in the container and the subsequent analysis on the collapse of the cavitation bubbles confirmed the effectiveness of the non-condensable gas bubble injection method on reducing cavitation damage.

Then we analyzed the interfacial dynamics of liquid-vapor phase transi-

tions and the wave equations for immiscible thermal conductive fluids. The phase transition rate is associated by the kinetic theory with the deviation of the vapor pressure from the saturated pressure. Analytical solutions to the linearized equations have been explored. The adiabatic and the isothermal limits have been investigated for both the linearized and the nonlinear equations, for latter the method of travelling wave solutions has been used. The wave structure of the solution to the problem with Riemann data has been discussed.

We also implemented a numerical scheme for solving the Euler equations with thermal conduction and phase transitions in the frame of front tracking. Heat conduction has been added to the interior state update with second order accuracy. Phase boundary propagation has been handled according to the interfacial dynamics. A numerical technique has been introduced to account for the thermal layer thinner than a grid cell. The scheme has been validated, extended to multi-dimension, adapted for cylindrical and spherical symmetry, and applied to the simulation of condensing and cavitating processes.

Key Words: bubbly flow, cavitation mitigation, phase transition, Riemann problem.

To my parents, wife and daughter

Table of Contents

List of Figures

List of Tables

Acknowledgements

I would like to express my profound gratitude to my advisor, Doctor James Glimm, for his advice, support and guidance toward my Ph. D. degree. He taught me not only the way to do scientific research, but also the way to become a professional scientist. He is my advisor and a lifetime role model for me.

I am also deeply indebted to the support of Doctor Roman Samulyak, especially for suggesting this important and exciting thesis topic. His scientific vigor and dedication makes him a great mentor and a good friend.

I would like to thank Drs. Xiaolin Li, Zhiliang Xu and Yongming Zhang, from whom I have learned many important scientific and mathematical skills. Work has been more productive and life a little easier thanks to them.

I would also like to thank all my friends for their friendship and encouragement during my four year study as a graduate student at Stony Brook. It has been great to have so many friends who can share my problem and happiness, only a few yards away. In particular, I would like to mention Xinfeng Liu and Jinjie Liu. They have shared with me many interesting and inspiring ideas.

Throughout my academic career, the constant support of my parents and

my wife has always motivated me to strive forward. The unconditional love of my parents has never been affected by the physical distance between us. Without my wife, dear Xiyue, I could never have been able to accomplish the work as torturing as writing a thesis. Last but not least, I want to thank my one-year-old daughter Vivian for cheering me up from the exhaustion after weeks of continuous work by calling me daddy. My dissertation is dedicated to them.

During my years here at Stony Brook I have grown and matured both personally and professionally. I am grateful to have gone through it all, and I look forward to what comes next. I thank all who have helped me through this leg of journey.

Chapter 1

Introduction

1.1 Direct Numerical Simulation of Bubbly Flows

Wave propagation in bubbly fluids has attracted investigators for many decades because of its special properties. Bubbly fluids have the unique feature that even a minute bubble concentration (volume fraction less than one percent) increases the compressibility of the system drastically. The system transports energy at a speed considerably lower than the sound speeds in both phases as a result of the energy exchange between the liquid and the bubbles. When additional effects such as vaporization and condensation play a role, *e.g.* in cavitating flows, further phenomena, still little understood, are superimposed upon the basic behavior of bubbly flows. The rich internal structure of bubbly flows endows the medium strikingly complex behavior.

One of the reasons for the study of bubbly flows is their wide applications ranging from hydraulic engineering to high energy physics experiments. In particular, we are interested in a recent application of bubbly fluids in the mitigation of cavitation damages in the Spallation Neutron Source (SNS)[1],

1

which will be discussed in details in Chapter 3. Another important motivation is to connect the microscopic behavior of individual bubbles to the macroscopic behavior of the mixed medium that one directly observes. Since the microstructure in this case is made up of a complex substructure, the task is much more complicated than that of classical kinetic theory.

The wave propagation in bubbly fluids has been studied using a variety of methods. Extensive investigation has been done on the subject based on various mathematical models. Significant progress has been achieved on the study of systems consisting of non-condensable gas bubbles (see for example [46, 6, 4, 44]) and of vapor bubbles (see for example [15, 24]). The treatment of the kinetic and thermal properties of the medium, *e.g.* the compressibility of the liquid and the thermal conduction, by different authors varies. But they shared a common feature that the two phases were not separated explicitly, *i.e.* the bubble radius and concentration were considered as functions of time and space. The Rayleigh-Plesset equation or the Keller equation governing the evolution of spherical bubbles has been used as the kinetic connection between the bubbles and fluid. These models include many important physical effects in bubbly systems such as the viscosity, the surface tension and thermal conduction. Numerical simulations of such systems requires relatively simple algorithms and are computational inexpensive. Nevertheless, such models treat the system as a pseudo-fluid and cannot capture all features of the rich internal structure of the bubbles. They exhibit sometimes large discrepancies with experiments [44] even for systems of non-condensable gas bubbles. These models are also not suitable if the bubbles are distorted severely by the flow or

even fission into smaller bubbles, as it may happen in cavitating and boiling flows [7, 13].

A powerful method for the multiphase problem, direct numerical simulation (DNS), is based on techniques developed for free surface flows. Welch [45] investigated numerically the evolution of a single vapor bubble using interface tracking method. Juric and Tryggvason [29] simulated the boiling flows using the incompressible flow approximation for both liquid and vapor and a simplified version of interface tracking. In the thesis, we describe a DNS method for the simulation of bubbly fluid using front tracking. Our FronTier code is capable of tracking and resolving topological changes of a large number of interfaces in two- and three-dimensional spaces. Both the bubbles and the fluid are compressible in the simulation because we are interested in the speed of wave propagations. We simulated the propagation of acoustic and shock waves in bubbly fluids and compared them with the theory and the experiments in Chapter 2.

After the validation of the FronTier code on the bubbly flows, it was applied to the engineering problem of cavitation mitigation in the Spallation Neutron Source. In Chapter 3, after the description of SNS and the related bubble injection technique for the mitigation of the cavitation, the problem was tackled in two steps. First, the pressure wave propagation in the container of the mercury target for the SNS was simulated using the front tracking method. Then the collapse pressure of cavitation bubbles was calculated by solving the Keller equation under the ambient pressure whose profile was obtained in the first step. Finally the efficiency of the cavitation damage mitigation

was estimated by comparing the average collapse pressure with and without injected bubbles.

1.2 Interfacial Dynamics of Phase Transitions

The dynamics of gas bubbles and the wave propagation in fluid filled with non-condensable bubbles have been investigated theoretically and experimentally for many decades, but the research on the corresponding problem for vapor bubbles is relatively new and the understanding is less developed. The interest on the dynamics of vapor bubbles is twofold.

Due to the large amount of energy absorbed or liberated in the form of latent during phase transitions, boiling and condensation are key processes in the extraction of energy from fuels for daily life. Heat exchanger equipment and piping in power plants and oil refineries are examples of traditional applications. A more recent issue coming from the space shuttles is the enhancement of heat transfer during boiling in microgravity. Another area that phase transitions play an important role is the cavitating flows, *e.g.* in the jet simulation in a diesel engine [22]. All these applications require detailed understanding of the phase transition process. Despite its importance and the vast body of research on boiling, the fundamental physical mechanisms involved are far from being understood, as pointed out by Juric *et. al.* [29] and Welch[45]. Not much experimental measurement on the dynamics of phase transitions is available because of the small time and spatial scale of the process.

The dynamics of phase transitions is of great scientific interest too. Analytical and numerical efforts to understand the boiling have been focused

mainly on simple models of vapor bubble dynamics until recently. Rayleigh [41] formulated a simplified equation of motion for inertia controlled growth of a spherical vapor bubble. Plesset and Zwick [37] and later Prosperetti and Plesset [40], among others, extended Rayleigh's analysis. Most models have been based on the Rayleigh-Plesset equation for incompressible liquid or the Keller equation of first order in c_l^{-1} for weakly compressible liquid. Phase transitions with full compressibility of both phases have been discussed by Menikoff and Plohr [36] with the transition zone treated as the macroscopic mixture of the two phases at equilibrium. More recently, Welch [45] studied the two-phase flows including interface tracking with mass transfer while the phase interface was assumed to exist in thermal and chemical (Gibbs potential) equilibrium. Juric and Tryggvason [29] simulated the boiling flows in incompressible fluids using the non-equilibrium phase transition model with a parameter called kinetic mobility whose value was measured experimentally. Hao and Prosperetti [24] investigated the dynamics of bubbles in acoustic pressure fields assuming the vapor was saturated. Matsumoto and Takemura [35] studied numerically the influence of internal phenomena on gas bubble motion with complete mass, momentum and energy conservation laws for compressible fluids and the interfacial dynamics of phase transitions, in which they referred to the value 0.4 for the evaporation coefficient measured by Hatamiya and Tanaka [25]. Later Preston, Colonius and Brennen [2], in the development of simpler and more efficient bubble dynamic models that capture the important aspects of the diffusion precesses, computed the growth and collapse of a vapor bubble under pressure waves in incompressible liquid with the interfacial dynamics of

5

phase transitions using a Chebychev spectral method to solve the temperature equation for the bubble.

The equations of the conservation laws and the interfacial dynamics of phase transitions have been studied numerically by the authors listed above. Hao and Prosperetti also investigated the linear theory of bubble oscillation in acoustic waves. However, the system of non-equilibrium phase transitions, as far as we know, has not been studied as a problem with Riemann data. As a contrast, the Riemann problem for reacting gas has been studied extensively [43]. For combustion flows, the energy difference between the phases (burnt and unburnt) is a fixed constant, namely, the heat released or absorbed in the chemical reaction, so the Riemann problem has not been changed by much. While for phase transitions, there is complicated interfacial dynamics involving the latent heat and Clausius-Clapeyron equation. Furthermore, the heat conduction makes the conservational laws no longer purely hyperbolic, thus the solution to the problem with Riemann data does not have the self similarity in the classical Riemann solution. In the adiabatic limit (thermal conductivity goes to zero), according to the theory of viscous profile, the solution should approach the Riemann solution, which we will show is correct for nonlinear equations but not for linearized equations. The theory of viscous profile usually deals with a hyperbolic field coupled to its own parabolic equation, while for Euler equations with thermal conduction the hyperbolic fields (pressure and velocity) are coupled to a different parabolic field (temperature), which complicates the problem by allowing jump discontinuity in certain fields while disallowing in others. The qualitative and quantitative properties of the

solution to the phase transition problem with Riemann data are our main subjects. The simpler case of two immiscible thermal conductive fluids was also investigated, in which the interface between the two fluids was a contact with thermal flux, or the so called thermal contact.

In Chapter 4 we analyzed the interfacial dynamics of phase transitions and the wave equations for immiscible fluids. The phase transition rate is associated by the kinetic theory with the deviation of the vapor pressure from the saturated pressure. Analytical solutions to the linearized equations have been explored. The adiabatic and the isothermal limits have been investigated for both the linearized and the nonlinear equations, for latter the method of travelling wave solutions has been used. The wave structure of the solution to the problem with Riemann data has been discussed.

In Chapter 5 we implemented a numerical scheme for solving the Euler equations with thermal conduction and phase transitions in the frame of front tracking. Heat conduction has been added to the interior state update with second order accuracy. Phase boundary propagation has been handled according to the interfacial dynamics. A numerical technique has been introduced to account for the thermal layer thinner than a grid cell. The algorithm has been validated and applied to sample physical problems.

Chapter 2

Direct Numerical Simulation of Bubbly Flows

In Section 2.1, we give a brief review of the theory and the experiments on bubbly flows. Section 2.2 is the description of the numerical method. Section 2.3 lists the results of the direct numerical simulations on linear and shock wave propagations in bubbly fluids along with the comparison to the theory and the experiments.

2.1 Theory and Experiments on Bubbly Flows

2.1.1 Wave Equations

The theory on bubbly flows is based on the homogenized model, in which the fluid and the bubbles are treated a single mixed phase, as opposed to the two separated phases in the direct numerical simulations. In compressible fluids with gas bubbles, the conservation of mass and momentum in one spatial

dimension give

$$\frac{1}{\rho_f c_f^2}\frac{\partial p}{\partial t} + \frac{\partial u}{\partial x} = \frac{\partial \beta}{\partial t},$$

$$\frac{\partial(\rho u)}{\partial t} + \frac{\partial(\rho u^2 + p)}{\partial x} = 0,$$

where β is the bubble volume fraction, and ρ is the averaged density of the mixed phase that equals $\rho_f(1-\beta) + \rho_g\beta$. The bubble oscillation in weakly compressible fluids is governed by the Keller equation [31, 32, 39],

$$(1-\frac{1}{c_f}\frac{\mathrm{d}R}{\mathrm{d}t})R\frac{\mathrm{d}^2R}{\mathrm{d}t^2} + \frac{3}{2}(1-\frac{1}{3c_f}\frac{\mathrm{d}R}{\mathrm{d}t})(\frac{\mathrm{d}R}{\mathrm{d}t})^2 = \frac{1}{\rho_f}(1+\frac{1}{c_f}\frac{\mathrm{d}R}{\mathrm{d}t}+\frac{R}{c_f}\frac{\mathrm{d}}{\mathrm{d}t})(p_B-p). \quad (2.1)$$

The bubble pressure p_g is approximately uniform except for sound waves of frequency far above the resonance. For bubbles of diameter $0.1mm$ and above, the thermal diffusivity $\nu << \omega R^2$ except for sound waves of frequency far below resonance. Therefore the bubbles are almost adiabatic for near-resonant sound waves. For bubbles consisting of γ-law gases,

$$p_g R^{3\gamma} = \text{constant}.$$

Neglecting the viscosity, the difference between p_g and p_B, the liquid pressure at the bubble surface, is from the surface tension,

$$p_g = p_B + \frac{2\sigma}{R}.$$

9

2.1.2 Linear Waves

The following dispersion relation for linear sound waves in bubbly fluids was derived from the wave equations [46].

$$\frac{k^2}{\omega^2} = \frac{1}{c_f^2} + \frac{1}{c^2}\frac{1}{1 - i\delta\frac{\omega}{\omega_B} - \frac{\omega^2}{\omega_B^2}}, \tag{2.2}$$

where ω_B is the resonant frequency of single bubble oscillation, δ is the damping coefficient accounting for the various dissipation mechanisms. c_f is the sound speed in bubble free fluid and c is the sound speed in the low-frequency limit, which is given by

$$\frac{1}{c^2} = (\beta\rho_g + (1-\beta)\rho_f)(\frac{\beta}{\rho_g c_g^2} + \frac{1-\beta}{\rho_g c_f^2}),$$

where ρ_g and ρ_f are the densities of the gas and the fluid, c_g and c_f are the sound speeds of the two phases. For adiabatic bubbles,

$$c = \sqrt{\frac{\gamma p}{\beta\rho_f}},$$
$$\omega_B = \frac{1}{R}\sqrt{\frac{3\gamma p}{\rho_f}}. \tag{2.3}$$

Chapman and Plesset [8] formulated δ as the sum of the acoustic, viscous and thermal contributions. It has been pointed out by Prosperetti *et. al.* [38, 12] that δ depends on the frequency of the sound wave. Nevertheless, Eq. (2.2) has been widely used for the dispersion relation. The dispersion relation for near-resonant sound waves measured in different experiments [16, 34, 42]

10

agreed with the theoretical predictions.

2.1.3   Shock Waves

The shock profile in the bubbly fluid evolves into a smooth steady form in contrast to the sharp discontinuity in the pure fluid. The steady state shock speed was obtained from the Rankine-Hugoniot relation [44],

$$\frac{1}{U^2} = \frac{1}{c_f^2} + \rho_f \frac{\beta_b - \beta_a}{P_a - P_b}$$

where subscripts a and b stand for ahead and behind the shock front. The steady state reaches thermal equilibrium, so for ideal gas bubbles with surface tension neglected, $P_a\beta_a = P_b\beta_b$. Therefore

$$\frac{1}{U^2} = \frac{1}{c_f^2} + \rho_f \frac{\beta_a}{P_b} \tag{2.4}$$

The evolution into a steady wave can take very long time and distance, and the unsteady waves move at higher velocities [44]. The shock profiles were measured for various gas bubbles by Beylich and Gülhan [4].

2.2   Numerical Method

We have been studying bubbly fluids as a system of one-phase domains separated by free interfaces using FronTier, a front tracking compressible hydrodynamics code. Front tracking is an adaptive computational method in which a lower dimensional moving grid is fit to and follows distinguished waves

in a flow. The front propagates according to the dynamics around it (*i.e.* Lagrangian) while the regular spatial grid is fixed in time (*i.e.* Eulerian). The discontinuities across the interfaces are kept sharp so as to eliminate the interfacial numerical diffusion which plagues traditional finite difference schemes.

In each time step, the front is first propagated then the interior states are updated. For the front propagation, the interfaces are first propagated in the normal direction for each point on the fronts and the states on either side evolve according to the solution of non-local Riemann problems. The hyperbolic solver has three steps: slope reconstruction, prediction using local Riemann solver, and correction by nonlocal solver. Then the states on the propagated fronts are updated in the tangential direction while the fronts are fixed. After that the fronts are tested for intersection and then untangled or redistributed if necessary to resolve the topological change or the clustering/sparsity of grid points on the interfaces due to front contract/expand.

For the subsequent interior state update, FronTier uses high resolution shock-capturing hyperbolic schemes on a spatial grid. Among the various shock capturing methods currently implemented in FronTier, a second order monotone upwind scheme for conservation laws (MUSCL) scheme developed by Van Leer and adapted for FronTier by I-L. Chern was used for the simulation here. MUSCL scheme is similar to the piecewise parabolic method described in [11], and a detailed description can be found in [10]. The two-pass implementation currently being used in FronTier, namely, first *regular* cells then *irregular* cells update, is well documented in [21]. Different equation of state models are used for gas/vapor bubbles and the ambient fluid.
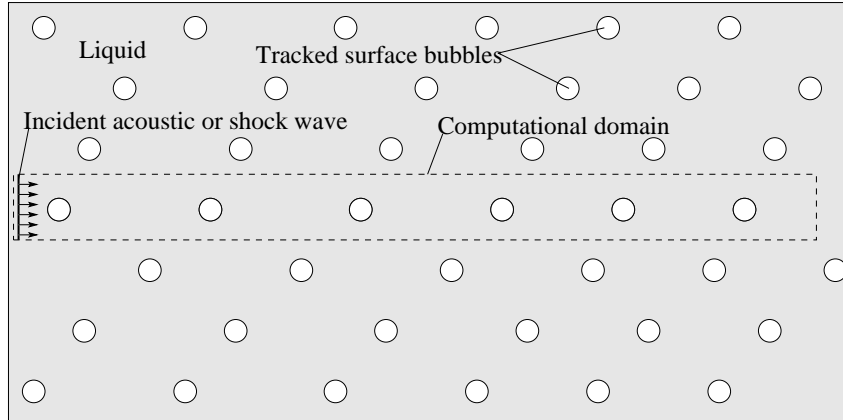
Figure 2.1: Schematic of the numerical experiments on the propagation of linear and shock waves in bubbly fluids.

FronTier can handle multidimensional wave interactions in both two- [20] and three- [19] dimensional spaces. Although computationally intensive, front tracking is potentially very accurate in treating many physical effects in bubbly flows, such as the compressibility of the fluid, surface tension and viscosity. Since the FronTier code is capable of tracking simultaneously a large number of interfaces and resolving their topological changes, many effects that are difficult to handle in mathematical models for bubbly flows are now naturally included in the simulations, *e.g.* the bubbles' deviation from sphericity, bubble-fluid relative motion, bubble merge/fissure and bubble size/spatial distribution. This approach has numerous potential advantages for modelling the phase transitions in boiling and cavitation flows. We have implemented a model for the phase transitions induced mass transfer across free interfaces [22]. FronTier is implemented for distributed memory parallel computers.

For the application of FronTier to the simulation of bubbly flows, the

region around a long column of bubbles (tens to hundreds) has been chosen as the computational domain, as shown in Figure 2.1. Two approximations were used in the simulations. The flow inside the column was assumed to be axisymmetric and the influence from the neighboring bubbles was approximated by the Neumann boundary condition on the domain wall. Thus the wave propagation in bubbly flows was reduced to an axisymmetric two-dimensional problem. An extensive introduction to the FronTier code for axisymmetric flows can be found in [21].

The axisymmetric flow approximation is crude although it is exact for the scattering of the planar wave by an isolated column of bubbles that are initially spherical. The Neumann boundary condition between adjacent bubbles is also too strong because the scattered pressure wave is only partially reflected. As a contrast, the scattering theory, on which the Keller equation is based, completely neglects the reflection between bubbles and the secondary scattering. Therefore the scattering theory only holds for the case of small β such that bubble interaction is negligible. For moderate β, the secondary scattering can not be neglected, and the Neumann boundary condition between adjacent bubbles is a better approximation.

2.3 Simulation Results on Bubbly Flows

In this section, we present the results of the DNS on the linear and shock wave propagations in bubbly fluids. The dispersion relation measured from the simulations were compared to the theory in Section 2.3.1. The shock speeds measured from the simulations were compared to the steady-state values, and

the shock profiles for various gas bubbles were compared to the experiments [4] in Section 2.3.2.

2.3.1 Linear Waves

To compare the simulation results with the theory we measured the dispersion relation. Writing down the complex wave number k in Eq. (2.2) as $k = k_1 + ik_2$, we have

$$e^{i(kx-\omega t)} = e^{-k_2 x} e^{i(k_1 x - \omega t)},$$

from which the phase velocity of the sound wave is defined as

$$V = \frac{\omega}{k_1}, \tag{2.5}$$

and the attenuation coefficient α in dB per unit length defined as

$$\alpha = 20 \log_{10} e \cdot k_2. \tag{2.6}$$

The bubble radius in the simulation was $R = 0.06mm$. From Eq. (2.3), we have

$$f_B = \frac{\omega_B}{2\pi} = \frac{1}{2\pi R} \sqrt{\frac{3\gamma p}{\rho_f}} = 54.4 \text{ KHz}.$$

We simulated the sound waves of frequencies ranging from 30 to 300 KHz. The volume fraction $\beta = 0.02\%$. The amplitude of the pressure wave was chosen to be 0.1 bar, one tenth of the ambient pressure. The linearity was ensured by comparison with sound waves of half amplitude, from which the dispersion relation measured was virtually the same. For each frequency, the

15

λ(cm)	f(KHz)	V(cm/ms)	V_{th}(cm/ms)	α(dB/cm)	α_{th}(dB/cm)
0.5	290	155	153	2.2	0.9
1.0	145	183	194	5.7	5.0
1.5	96.7	220	274	18.4	20.7
2.0	72.5	160	173	28.5	30.9
2.5	58.0	100	100	21.8	29.4
2.75	52.7	75	84	18.9	25.2
3.0	48.3	68	75	17.8	20.4
4.0	36.3	62	68	10.7	8.5
5.0	29.0	66	69	3.9	4.4

Table 2.1: Phase velocities(V) and attenuation coefficients(α) from the simulation and the theory. λ is the wavelength in pure water. V and α are the simulation results, V_{th} and α_{th} are the theoretical predictions from Eq. (2.2) with $\delta = 0.7$. $R = 0.06mm$, $\beta = 0.02\%$.

sound wave of up to 8 wavelengths was propagated from the pure fluid into the bubbly region. The cross sectional averaged pressure in the bubbly region was recorded at selected times and positions, from which the phase velocity and the attenuation coefficient were measured. The phase velocity was obtained by measuring the propagation speed of the first pressure node in the bubbly region. The envelope of the oscillating pressure wave was plotted and the attenuation coefficient was measured in the $1cm$-long bubbly fluid region next to the incident plane by fitting the envelope to an exponential curve. A shorter region was used for the frequency with the strongest attenuation ($\lambda = 2cm$).

The phase velocities and attenuation coefficients measured from the simulations were listed in Table 2.1 along with the theoretical predictions. For the theoretical prediction 0.7 was used for the damping coefficient δ in Eq. (2.2). The measured dispersion relation was compared to the theoretical curves in Figure 2.2. It can be seen that the simulation agrees well with the theory.
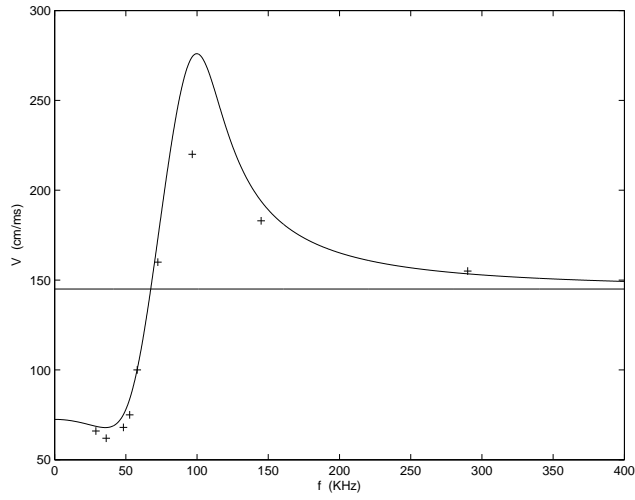
(a)
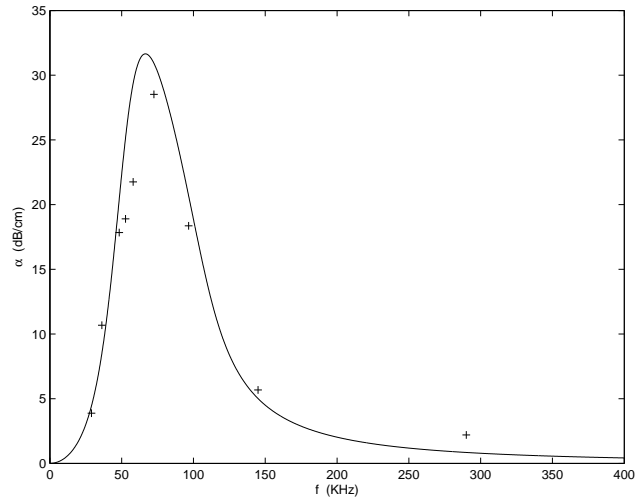
(b)

Figure 2.2: Comparison of the dispersion relation between the simulation and the theory. $R = 0.06mm$, $\beta = 0.02\%$. (a) is the phase velocity, (b) is the attenuation coefficient. In both figures, the crosses are the simulation data and the solid line is the theoretical prediction from Eq. (2.2) with $\delta = 0.7$. The horizontal line in figure (a) is the sound speed in pure water.
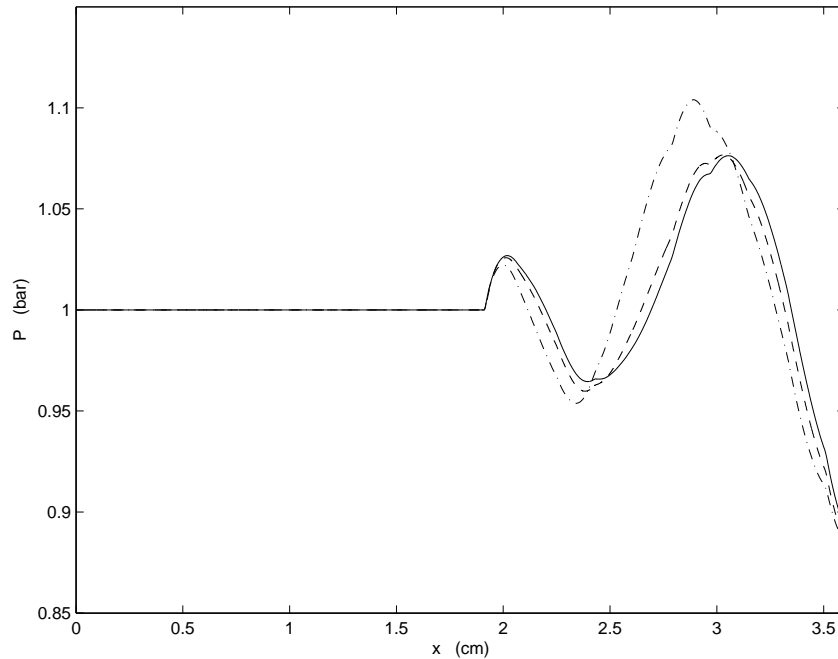
Figure 2.3: The pressure profile in bubbly water 23 μs after the incidence of the sound wave with wavelength 1 cm in pure water. The default resolution used in the simulations was 100 grid/mm, under which the bubble radius $R = 0.06mm$ corresponds to 6 grids. Symbols: solid line is the default resolution 100 grid/mm, dash-dotted line is 50 grid/mm, dashed line is 200 grid/mm.

However, the point in Figure 2.2(a) with frequency about 100 KHz has large deviation from the theoretical value. Most likely it is because the measurement of the sound speed was inaccurate in the presence of strong attenuation, which is a phenomenon also observed in the experiment [16].

The grid resolution for most of our simulations on linear wave propagations was 100 grids per millimeter. To ensure the accuracy of the simulation results, a mesh refinement check has been carried out. Figure 2.3 shows a

typical result. It can be seen that the results were reasonably accurate at the default grid resolution (100 grid/mm). It has also been noticed that near the resonant frequency f_B the resolution requirement is higher. More specifically, higher resolution would give larger attenuation coefficients, which explains in part why the points in the Figure 2.2(b) are all below the theoretical curve near the peak. Another important reason for the deviation is, as pointed out by Prosperetti *et. al.* [38, 12], the dependence of δ on the frequency. The simplification used in the simulation, such as axisymmetric approximation and Neumann boundary condition, also contributed to the error.

2.3.2   Shock Waves

Beylich and Gülhan [4] studied the propagation of shock waves in glycerol filled with bubbles of various gases. We carried out the numerical simulations using their experimental settings. We have also varied the sound speed in the pure fluid to measure the corresponding shock speeds and compares them to the steady-state values given by Eq. (2.4). In the simulations, the pressure behind the shock was either fixed at the boundary or set as the initial pressure in an air layer next to the bubbly fluid. The results from the two methods have been compared and found to be very close.

The measured shock speeds are listed in Table 2.2. The speeds were measured about 10 cm away from the shock incident plane. It is seen from the table that the measured shock speeds differ from the steady state values by no more than 10% and in general the measured values are larger. The reason for the deviation is that the shock waves in the simulations had not reached

gas(γ)	c_f(m/s)	β_a(%)	P_b(bar)	U(m/s)	U_{th}(m/s)
SF_6(1.09)	1450	0.25	1.9	26.20	24.60
SF_6(1.09)	458	0.25	1.9	22.52	21.92
SF_6(1.09)	145	0.25	1.9	13.47	12.54
N_2(1.4)	1450	0.25	1.7	25.56	23.30
N_2(1.4)	458	0.25	1.7	22.21	20.98
N_2(1.4)	145	0.25	1.7	12.29	12.36
He(1.67)	1450	0.25	1.9	25.68	24.60
He(1.67)	458	0.25	1.9	22.69	21.92
He(1.67)	145	0.25	1.9	13.52	12.54
SF_6(1.09)	1450	2.17	1.8	8.72	8.23
SF_6(1.09)	458	2.17	1.8	8.04	8.12
SF_6(1.09)	145	2.17	1.8	7.10	7.17
N_2(1.4)	1312	2.17	1.8	8.60	8.23
N_2(1.4)	458	2.17	1.8	9.09	8.12
N_2(1.4)	145	2.17	1.8	7.80	7.17
He(1.67)	1450	1.04	1.9	13.92	12.19
He(1.67)	458	1.04	1.9	12.70	11.82
He(1.67)	145	1.04	1.9	9.70	9.35

Table 2.2: Shock speeds measured from the simulations are compared to the steady state values. β_a is the bubble volume fraction ahead of the shock, P_b is the pressure behind the shock, U and U_{th} are the measured shock speed and corresponding steady-state value given by Eq. (2.4). $p_a = 1.11$bar, $\rho_f = 1.22 g/cm^3$, $R_a = 1.15mm$.

the steady state, and the unsteady shock speeds were higher than the steady state values (*cf.* Section 2.1.3).

We have also plotted the shock profiles with bubbles of different content in Figure 2.4. The results were compared to those measured in the experiment of Beylich *et. al.* [4]. The profiles were measured at 50 cm away from the shock incident plane. From the figures we noticed the pressure in the bubbly fluid oscillates after the passage of the shock front. The oscillation amplitude was smaller for gas with larger polytropic index γ, which agrees with the experiment. The period of the oscillation differed from experimental data by 10 to 20 percent, while the amplitude was much smaller in the simulations.

There were several sources of error that could be responsible for the deviation. The main source of error is numerical dissipation at the bubble surface. The default grid resolution for the simulations on shock wave propagation was 50 grids per centimeter, the bubble radius was also 6-grid wide. It has been found that increasing resolution did increase the oscillation amplitude but not drastically. Other sources of error include the axisymmetric approximation and the Neumann boundary condition on the domain wall. As a summary, the shock velocity measurement agreed well with the theory, while the shock profiles agreed with the experiment qualitatively and partly quantitatively.
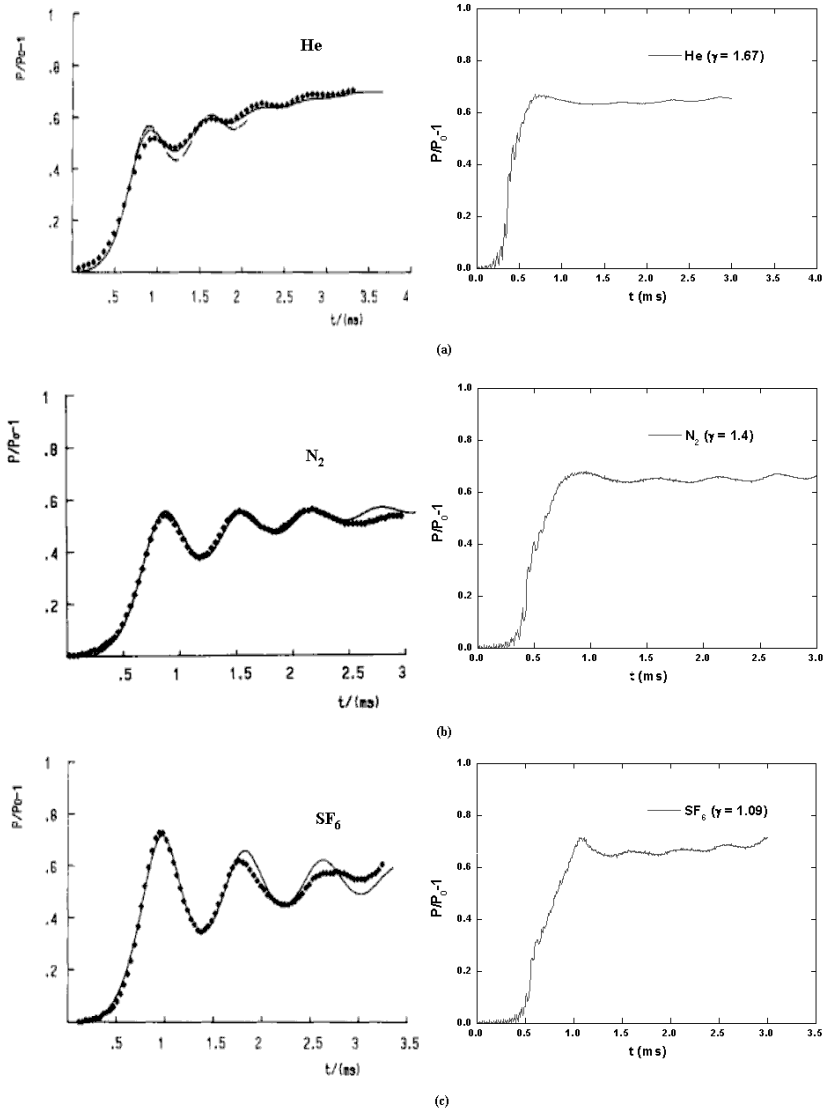
Figure 2.4: The shock profiles in bubbly glycerol. The parameters in the simulations were from the experiments [4]. $p_a = 1.11$ bar, $\rho_f = 1.22 \ g/cm^3$, $R_a = 1.15mm$. Left figures are from the simulations, right ones are from the experiments. (a) He($\gamma = 1.67$), $\beta = 0.27\%$, $P_b = 1.9$bar. (b) N$_2$($\gamma = 1.4$), $\beta = 0.25\%$, $P_b = 1.7$bar. (c) SF$_6$($\gamma = 1.09$), $\beta = 0.25\%$, $P_b = 1.9$bar. The curves in the experimental figures are the author's original fitting with artificial turbulent viscosity.

Chapter 3

Application of Bubbly Flows to Cavitation Mitigation

Having validated to some extent the FronTier code for the direct numerical simulation of bubbly flows, we applied it to the cavitation mitigation problem in the Spallation Neutron Source. In Section 3.1 the design of the SNS target and associated fluid dynamical issue were described. The description of the method we used to estimate the collapse pressure of cavitation bubbles was given in Section 3.2. Section 3.3 listed the results of the simulations using the front tracking method on the pressure wave propagation in the pure mercury and the mercury injected with non-condensable gas bubbles. In Section 3.4 the collapse pressure of cavitation bubbles was calculated by solving the Keller equation in the ambient pressure whose profile was obtained from the simulations. Finally, in Section 3.5 the average collapse pressure with and without injected bubbles were compared to estimate the cavitation mitigation efficiency.

3.1 Spallation Neutron Source

The Spallation Neutron Source (SNS) is an accelerator-based neutron source being built at Oak Ridge National Lab. The SNS will provide the most intense pulsed neutron beam in the world for scientific research and industrial development. In SNS, 800MeV proton beams bombarding the mercury target in a steel container deposit totally 2.1 kJ of energy per pulse in less than $300ns$ which results in the rapid pressure increase in the mercury (see Figure 3.1). The peak deposited energy density is 19 J/cc, corresponding to 500 bar in mercury. The subsequent pressure waves induces severe cavitation on the container, so much so that the lifetime of the container was only two weeks with 1MW proton pulses at the frequency of 60Hz [1]. In order to mitigate the cavitation erosion, research is being done on the evaluation of cavitation-resistant materials and coatings. It has also been suggested that the injection of non-dissolvable gas bubbles into the container could absorb the energy of the pressure wave. Our goal is to estimate the efficiency of the cavitation mitigation by the bubble injection method.

The SNS target prototype tested at the Los Alamos National Laboratory was a cylinder of 10 cm diameter and 30 cm length [1]. The initial pressure rise occurred essentially instantaneously compared to acoustic time scales. The pressure distribution, as shown in Figure 3.1, has a Gaussian profile in the transverse direction with $\sigma = 1.0$ cm and an exponential attenuation along the axis. The pressure profile can be described by

$$P_0(r, z) = 500e^{-r^2 - 0.1z} \text{ bar,} \tag{3.1}$$
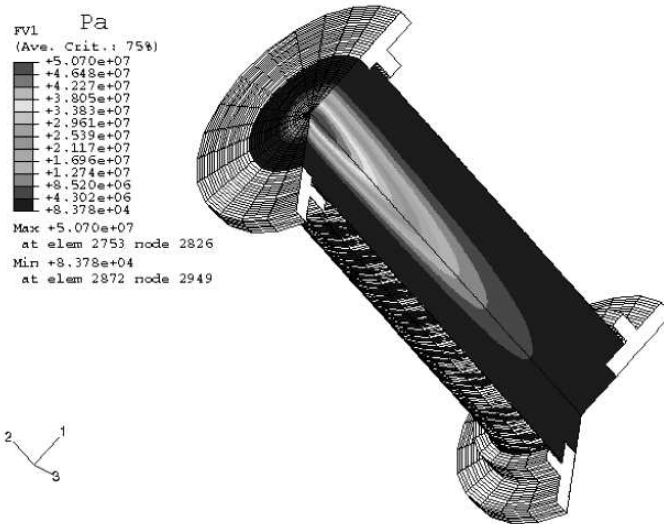
Figure 3.1: The pressure distribution right after a pulse of proton beams in the mercury target of the Spallation Neutron Source. Courtesy of SNS experimental facilities, Oak Ridge National Lab.

where r and z are in cm, and the origin of z axis is the window where proton beams enter.

3.2   Method of Approach

Before we compare the cavitation erosion in pure and bubbly mercury, a brief introduction to the mechanism of cavitation damage and the method we used to quantify it is given in this section. Cavitation is the process in which a bubble, consisting of vapor and non-condensable gas, expands and collapses according to the surrounding pressure which decreases and increases rapidly. Vapor bubbles are formed in the fluid when the pressure falls below the saturated vapor pressure of the fluid at the ambient temperature. They implode when the fluid pressure rises back above the saturated vapor pressure or when the bubbles move into a region with higher pressure. If the bubble is close to the container wall, the shock wave from the rebound of the collapse erodes the wall as in the SNS target container.

The attenuation of the pressure wave during the rebound phase of the cavitation bubbles was studied carefully in [26]. The pressure of the rebounded wave that hits the container wall is an indicator of the cavitation erosion. Since it is proportional to the first collapse pressure of cavitation bubbles, for the estimation of the cavitation mitigation efficiency we only need to compare the average collapse pressure in the pure mercury and the bubbly mercury. In order to calculate the collapse pressure, we need to know how the cavitation bubbles grow and collapse under the pressure wave in the container. Since the collapsed bubble size ($< 0.1 \mu m$) is less than a millionth of the container size

($10cm$), it is difficult to simulate directly the evolution of cavitation bubbles in the entire container. Instead we did it in two steps.

First, we simulated the propagation of the pressure wave in the container with the initial distribution given by Eq. (3.1). The simulation was carried out for both the pure mercury and the mercury injected with non-dissolvable gas bubbles. For the simulation of the bubbly mercury, the bubble surfaces were tracked explicitly via the front tracking method that we have described. The pressure relaxation caused by the cavitation was ignored in the simulation of pressure waves in the container. We assumed that the growth and collapse of cavitation bubbles is uncorrelated, namely that the far field liquid pressure for a cavitation bubble is not significantly perturbed by relaxation waves from neighboring cavitation bubbles. Since the distribution of cavitation centers is unknown for mercury under such conditions, accounting for pressure relaxation processes would contain a large amount of uncertainty.

In the second step, the collapse pressure of cavitation bubbles was calculated by solving the Keller equation (Eq. (2.1)) under the liquid pressure whose profile was obtained in the first step. A cavitation bubble consists of vapor and non-condensable gas. The partial pressure of the vapor in the bubbles remains negligible compared to the pressure wave in the SNS, while the partial pressure of the gas (typically air) changes violently. As a result, for the estimation of the collapse pressure it suffices to calculate the growth and collapse of the cavitation bubbles that consist of air only.

27

3.3   Pressure Wave Propagation in the Container

Inferred from Eq. (3.1) for the initial pressure distribution, the strongest pressure oscillation and consequently the most severe cavitation might be located at the center of the entrance window, which was confirmed by the simulation. Therefore we compared the pressure profile at the spot in the pure and the bubbly mercury. The pressure profile in the pure mercury is shown in Figure 3.2, while the pressure profile in the mercury filled with air bubbles is shown in Figure 3.3. It is readily seen that the pressure decayed much faster with bubble injected as expected, since the bubbles absorbed the energy from the pressure wave and spread it away from the entrance window. The pressure oscillation in bubbly mercury was also more rapid due to the reflections between bubbles. Both profiles can be approximately described by the formula

$$P_w(t) = P_{w0}e^{-\frac{t}{\tau}}\cos(\frac{2\pi t}{T}), \qquad (3.2)$$

where P_{w0} is the pressure oscillation amplitude on the window right after the bombard of the proton pulse, τ is the inverse of the attenuation rate, and T is the oscillation period. From Figure 3.2 we found $P_{w0} = 500$ bar, $\tau = 0.94ms$, $T = 70\mu s$ for pure mercury. From Figure 3.3 we found $P_{w0} = 600$ bar, $\tau = 50\mu s$, $T = 12\mu s$ for mercury filled with air bubbles of radius $1.0mm$ and volume fraction 2.5%.
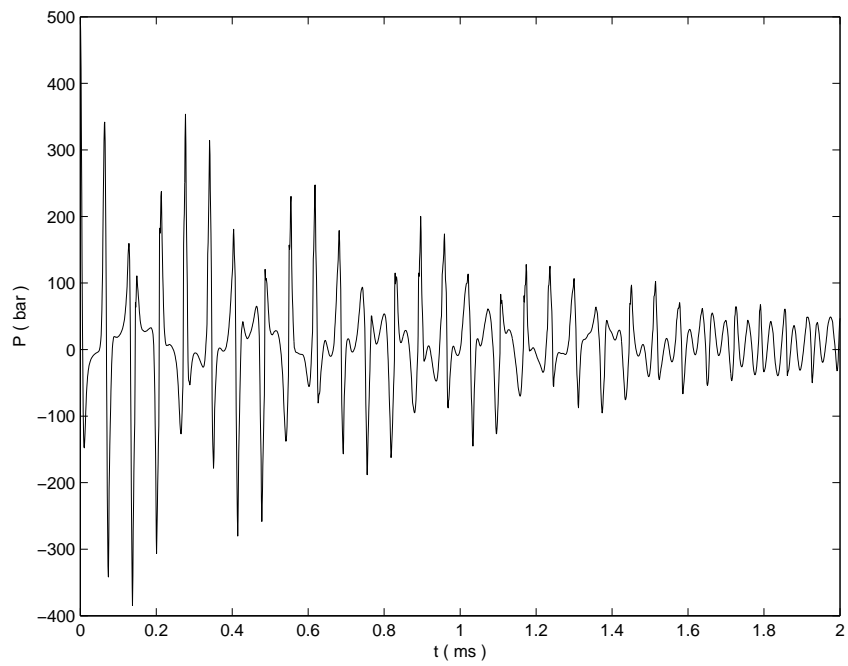
Figure 3.2: The pressure profile at the center of the entrance window in the pure mercury.
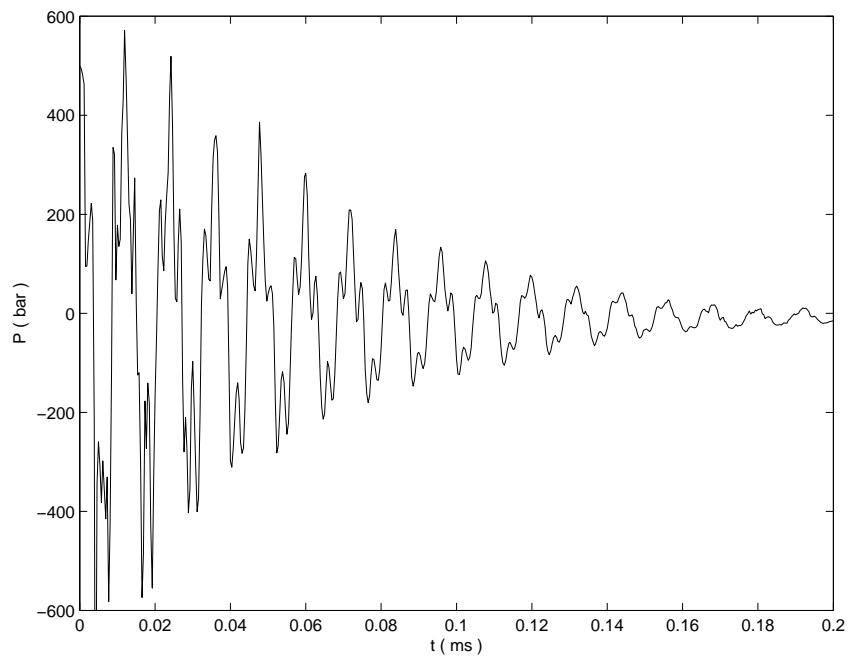
Figure 3.3: The pressure profile at the center of the entrance window in the mercury filled with air bubbles. Bubble radii are $1.0mm$ and the volume fraction is 2.5%.

3.4 Collapse Pressure of Cavitation Bubbles

The second step is the calculation of the collapse pressure of cavitation bubbles. The Keller equation for the bubble growth and collapse in the weakly compressible liquid was used for that purpose. With the ambient liquid pressure obtained in the first step, the closed system of equations is

$$(1 - \frac{1}{c_f}\frac{dR}{dt})R\frac{d^2R}{dt^2} + \frac{3}{2}(1 - \frac{1}{3c_f}\frac{dR}{dt})(\frac{dR}{dt})^2 = \frac{1}{\rho_f}(1 + \frac{1}{c_f}\frac{dR}{dt} + \frac{R}{c_f}\frac{d}{dt})(p_B - p),$$

$$p_g = p_B + \frac{2\sigma}{R},$$

$$p_g R^3 = p_{g0} R_0^3.$$

The p in the equation above is the difference between the ambient pressure and the vapor pressure of mercury in the bubble, however the latter is much smaller in our case and can be neglected. In the last equation, the gas pressure in the bubble is associated with the bubble radius by the isothermal relation, which is valid for the cavitation bubbles in SNS with $R_0 < 1\mu m$.

To verify that $R_0 < 1\mu m$ for the majority of the cavitation bubbles, recall that the cavitation bubble grows from a nucleus whose radius is bounded below by the surface tension condition

$$\frac{2\sigma}{R_0} < -p.$$

For liquid mercury, $\sigma = 0.48 kg/s^2$, in SNS a typical tension of 100 bar gives $R_0 > 0.1\mu m$. So it is reasonable to assume the R_0 of most cavitation bubbles are between $0.1\mu m$ and $1\mu m$.

The pressure waves in both the pure mercury and the bubbly mercury take on an attenuating sinusoidal form. Since the attenuation is slower than the oscillation, to obtain the overall collapse pressure of cavitation bubbles we could calculate it in the purely sinusoidal pressure wave and add it up over the periods with an attenuating amplitude. The purely sinusoidal pressure wave has the following form,

$$p(t) = P \sin(\frac{2\pi t}{T} + \phi_0), \tag{3.3}$$

where ϕ_0 is the initial phase angle when the cavitation bubble starts to grow from a nucleus. ϕ_0 must be within [-π,0] because for the bubbles to grow the initial pressure must be below the saturated pressure of mercury, which is almost 0 compared the the pressure wave in the SNS.

The typical bubble size evolutions with various ϕ_0 are shown in Figure 3.4. It's interesting to notice that the bubble does not always collapse – the bubbles beginning to grow at $\phi_0 < -0.8\pi$ continues to grow after a period. Although they may collapse after two or more periods according to the Keller equation, the associated collapse pressure is smaller since the ambient pressure has attenuated. On the other hand, for ϕ_0 within [-0.8π,0] the bubble collapses to a small bubble within about a period. We are only interested in the first collapse because it has the largest pressure and after that the bubble often fissures into a cloud of tiny bubbles (*cf.* [5]) and the Keller equation no longer applies. Figure 3.5 shows the dependence of the first collapse pressure P_c on ϕ_0. It is seen that the collapse pressure is highest for ϕ_0 around -0.63π,
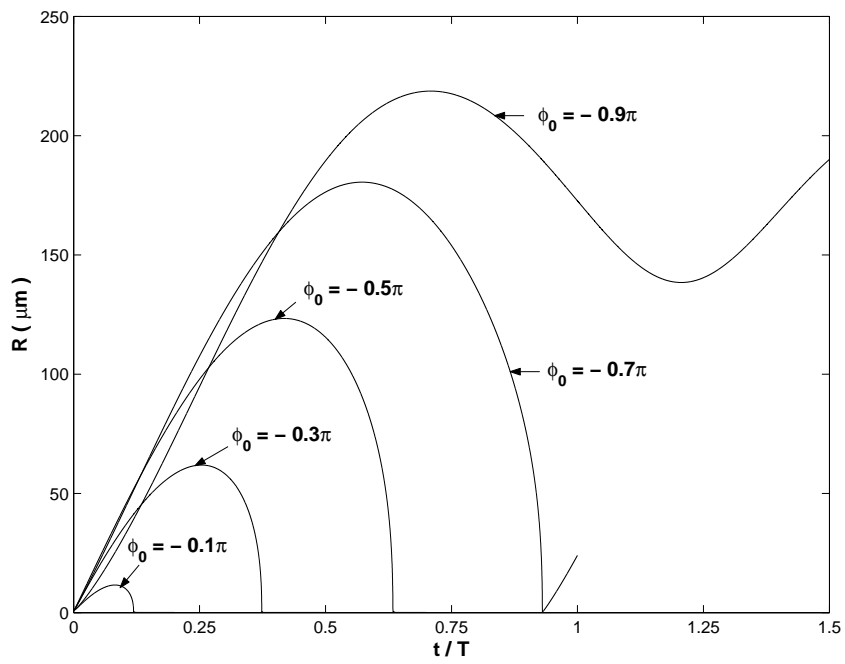
Figure 3.4: Bubble size evolution with different ϕ_0. $R_0 = 1.0\mu m$, $p_{g0} = 0.01$ bar, $P = 100$ bar, $T = 20\mu s$.

33
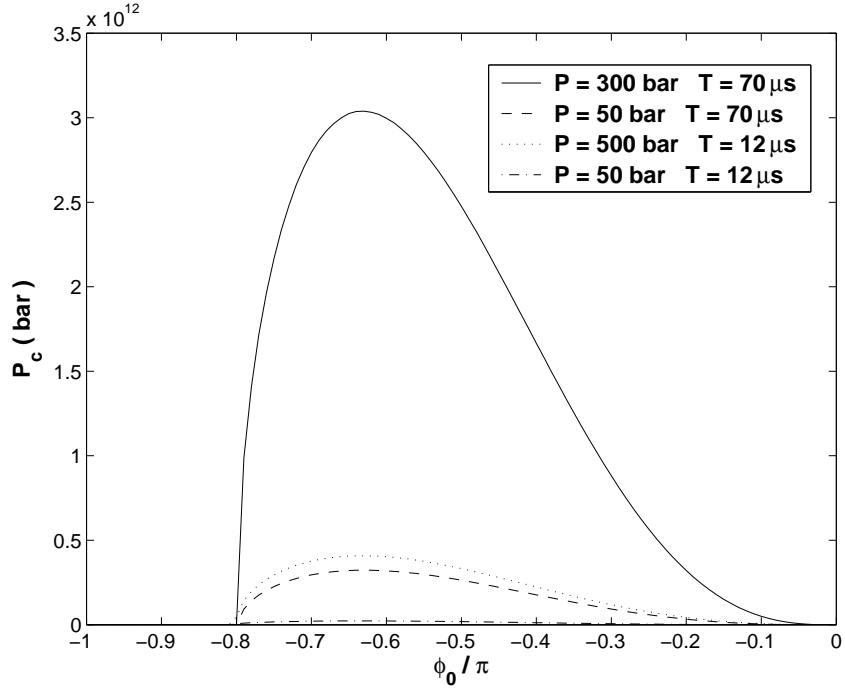
Figure 3.5: The first collapse pressure P_c *vs.* ϕ_0 under the sinusoidal pressure waves with different amplitude P and period T. The solid line and the dashed line correspond to the pure mercury, the dotted line and the dash-dotted line correspond to the mercury filled with air bubbles of radii $1.0mm$ and volume fraction 2.5%.

and the average collapse pressure $\overline{P_c}$ is roughly one half of the peak value at $\phi_0 = -0.63\pi$.

Neglecting the surface tension and the viscosity, which is justified by the high pressure wave in the liquid, the Keller equation becomes a purely acoustic equation so that P_c is a function of $R_0/c_f T$. On the other hand, so long as $p_{g0} \ll |p|$, the bubble grows before the first collapse to a maximum size that depends only on the gas content $p_{g0}R_0^3$ and the ambient pressure wave. Therefore P_c is determined by the gas content $p_{g0}R_0^3$ of the cavitation bubble

34

rather than by R_0 and p_{g0} independently. Combining the two observations, we see that $\overline{P_c}$ is a function of P and $p_{g0}(R_0/c_f T)^3$. In fact, in the range of $P < 10$ Kbar and $T < 1ms$, an empirical formula for $\overline{P_c}$ with P, T as variables and p_{g0}, R_0 as parameters was obtained,

$$
\begin{aligned}
\overline{P_c}(P,T) &\doteq \frac{1}{2} P_c(P, T, \phi_0 = -0.63\pi) \\
&\doteq \frac{93.0}{2} (\frac{P}{\rho_f c_f^2})^{1.25} (\frac{p_{g0}}{\rho_f c_f^2} (\frac{R_0}{c_f T})^3)^{-0.50} \text{ Kbar,}
\end{aligned} \tag{3.4}
$$

with error less than 1%. The result agreed with the fact that the higher the rate of stressing the fluid is experiencing, the higher tension can be sustained. In the bubble injection regime, the period of pressure oscillation T decreases which in turn reduces the cavitation bubble collapse pressure.

3.5   Efficiency of Cavitation Damage Mitigation

Our goal was to evaluate the mitigation of the cavitation damage by the bubble injection, *i.e.* to find the ratio between the overall impact on the container from the collapses of cavitation bubbles in the pure mercury and the mercury with non-dissolvable gas bubbles. As mentioned in Section 3.2, we needed only to compare the average collapse pressure $\overline{P_c}$. It's worth pointing out that, according to Eq. (3.4), $\overline{P_c}$ can be factored into two parts, one depending on P and T, and the other one on p_{g0}, R_0. This implies that the ratio between the two cases (with and without bubble injection) is *independent* of the size of the initial nucleus and amount of gas in it as long as $p_{g0} \ll P$.

To estimate quantitatively the efficiency of the cavitation mitigation on

the entrance window by bubble injection, we found the average collapse pressure in each period and took the sum over all the periods of the attenuating sinusoidal pressure wave given in Eq. (3.2). In other words, we defined

$$S = \sum_{n=0}^{\infty} \overline{P_c}(P_w(nT), T) = \sum_{n=0}^{\infty} \overline{P_c}(P_{w0}e^{-\frac{nT}{\tau}}, T), \qquad (3.5)$$

where the summand is the average collapse pressure in the n'th period. The overall cavitation damage is proportional to S. The ratio of S in pure mercury and S in bubbly mercury was defined to be the mitigation efficiency, $i.e.$

$$E(\beta, R) = \frac{S(\beta = 0)}{S(\beta, R)}, \qquad (3.6)$$

where β and R are the volume fraction and mean radius of the injected bubbles. Combining Eqs. (3.4) and (3.5), we obtain

$$S \doteq K P_{w0}^{1.25} T^{1.50} \sum_{n=0}^{\infty} e^{-1.25\frac{nT}{\tau}} = K \frac{P_{w0}^{1.25} T^{1.50}}{1 - e^{-1.25\frac{T}{\tau}}}, \qquad (3.7)$$

where K is a coefficient depending only on the cavitation nucleus and cancels in E.

Using the data in the paragraph following Eq. (3.2), we found that $E(\beta = 2.5\%, R = 1.0mm) = 32.7$, which means the overall cavitation bubble collapse pressure is reduced by more than 32 times. Varying β and R in the simulation of pressure wave propagation we can easily measure the corresponding efficiency. For example, when $\beta = 0.53\%$ and $R = 0.5mm$, we found $P_{w0} = 450$ bar, $\tau = 44$ μs, T = 16 μs. From Eqs. (3.6) and (3.7),

36

$E(0.53\%, 0.5mm) = 42.9.$

As a conclusion, we have confirmed the mitigation of cavitation by the injection of non-dissolvable bubbles. More specifically, we have found that the injection of bubbles with the volume fraction of order 1% reduces the cavitation erosion by more than order of magnitude. At the same time, bubbles absorb/disperse the energy and rapidly attenuate the pressure on the entrance window of the SNS target so that the cavitation lasts for much shorter time.

Chapter 4

Interfacial Dynamics of Phase Transitions

In Section 4.1 the governing equations and boundary conditions are listed. Section 4.2 gives the alternative forms of the equations. In Section 4.3 and Section 4.4 we present the analytical solutions to the problem with Riemann data for the linearized equations with the temperature field decoupled, for immiscible fluids and phase transitions respectively. In Section 4.5 we explored the linearized equations with the pressure field decoupled. For both cases, the solutions to the problem with Riemann data in the two limits $\kappa \to 0$ and $t \to 0$ are discussed. In Section 4.6 the problem with Riemann data for the nonlinear equations are solved in both limits. The convergence of the solution to the classical Riemann solution are analyzed using the method of travelling wave solutions. Finally the wave structure of the solution are discussed.

4.1 Governing Equations and Boundary Conditions

The governing equations and boundary conditions at the vapor-liquid or gas-liquid interface are described in detail in [27] and [35]. Away from the in-

terface the governing equation is the Navier-Stokes equations for compressible fluids with body force term. Since the thermal effect is normally dominant over the viscous effect in bubbly flows [12] and phase transitions [29], viscosity is neglected in our equations and the numerical algorithm. In the following equations subscript $i = v$ stands for vapor phase and $i = l$ for liquid phase.

4.1.1   Governing Equations

The conservation equation of mass is

$$\frac{\partial \rho_i}{\partial t} + \nabla \cdot (\rho_i \mathbf{u}_i) = 0, \tag{4.1}$$

where ρ_i is the density and $\mathbf{u}_i$ is the velocity. The conservation equation of momentum is

$$\frac{\partial (\rho_i \mathbf{u}_i)}{\partial t} + \nabla \cdot (\rho_i \mathbf{u}_i \mathbf{u}_i) + \nabla p_i = -\rho_i \nabla \phi, \tag{4.2}$$

where p_i is the pressure, ϕ the time-independent specific potential of conservative force, *e.g.* $\phi = -\mathbf{g} \cdot \mathbf{r}$ for constant gravitational force. The conservation equation of energy is

$$\frac{\partial (\rho_i E_i)}{\partial t} + \nabla \cdot ((\rho_i E_i + p_i) \mathbf{u}_i) = -\nabla \cdot \mathbf{q}_i, \tag{4.3}$$

where E_i is the specific total energy

$$E = \frac{\mathbf{u}^2}{2} + \phi + \text{specific internal energy},$$

and $\mathbf{q}_i$ is the heat flux, which satisfies Fourier's law of thermal conduction,

$$\mathbf{q} = -\kappa \nabla T,$$

where T is the temperature and κ is the thermal conductivity.

The gas is considered as the ideal gas with γ-law property. The equation of state for the liquid is of the stiffened polytropic (SPOLY) type, whose parameters are chosen to fit the thermodynamical quantities at the specific temperature and pressure. More details are given in Appendix A.

4.1.2 Boundary Conditions at Material Interface

Denote the mass flux across the interface from left to right by M and the flux from liquid to vapor by M_{ev}. $M_{ev} > 0$ means evaporation and $M_{ev} < 0$ means condensation. If the liquid is on the left side then $M = M_{ev}$, otherwise $M = -M_{ev}$. In the following equations subscript n and τ stands for normal and tangential respectively, Δ denotes right side minus left side, bar stands for arithmetic average between the two sides.

The boundary conditions for mass conservation is

$$\Delta u_n = M \Delta \frac{1}{\rho} = M \Delta V, \tag{4.4}$$

where the positive direction of u_n points from left to right, and V stands for the specific volume, *i.e.* the reciprocal of ρ. For the momentum conservation

at boundary, Eq. (4.2) should be modified to include the surface tension

$$\frac{\partial(\rho_i \mathbf{u}_i)}{\partial t} + \nabla \cdot (\rho_i \mathbf{u}_i \mathbf{u}_i) + \nabla p_i + \int_\Gamma p_s \delta(\mathbf{r} - \mathbf{r}_s)\mathbf{n}ds = -\rho_i \nabla \phi,$$

where Γ is the interface and p_s is the pressure jump due to surface tension that equals

$$p_s = \sigma(\kappa_1 + \kappa_2),$$

where σ is the surface tension, while κ_1 and κ_2 are the principal curvatures of the interface, which are positive when interface is convex toward the positive $\mathbf{n}$ direction. Integrating the equation in an infinitesimally thin slice co-moving with the interface, we can find the boundary condition for the momentum conservation to be

$$\Delta p + p_s + M\Delta u_n \;\; = \;\; 0, \tag{4.5}$$

$$M\Delta \mathbf{u}_\tau \;\; = \;\; 0, \tag{4.6}$$

The energy conservation at boundary should also contain the surface energy as following

$$\frac{\partial(\rho_i E_i)}{\partial t} + \nabla \cdot ((\rho_i E_i + p_i)\mathbf{u}_i) + \int_\Gamma \bar{u}_n p_s \delta(\mathbf{r} - \mathbf{r}_s)ds = \nabla \cdot (\kappa_i \nabla T_i).$$

Integrating again, we have the boundary condition for the energy conservation

$$M(\Delta H - \bar{V}\Delta p) + \Delta \mathbf{q}_n = 0, \tag{4.7}$$

41

where H stands for the specific enthalpy

$$H = \text{specific internal energy} + pV.$$

Due to the thermal conduction, the temperature is continuous across the interface, so

$$\Delta T = 0. \tag{4.8}$$

Thermal contact

If the interface is the contact between two immiscible fluids, then by definition there is no mass flux across the interface (yet the thermal conduction is allowed, hence the name "thermal contact").

$$M = 0, \tag{4.9}$$

so the quantity $\Delta H - \bar{V}\Delta p$ on the left side of Eq. (4.7) is arbitrary. The governing equations combined with the boundary conditions listed above Eqs. (4.1)–(4.9) are closed. The normal velocity of the two phases are equal at the contact, and also equal to the normal velocity of the interface.

$$U_{ph} = u_n.$$

The interface is propagated at such velocity in the computation.

Phase boundary

In case of phase transitions, $M \neq 0$ so the value of $\Delta H - \bar{V} \Delta p$ plays an important role in the interfacial dynamics. At equilibrium ΔH is defined as the latent heat L. In some literatures, *e.g.* [35], ΔH is fixed to a constant, though in reality L is not a constant. A better approximation of ΔH is obtained by linearization near the ambient temperature as in [29], which gives

$$\Delta H(T) = L(T_{amb}) + (T - T_{amb})\Delta c_p(T_{amb}),$$

where $c_p(T_{amb})$ is evaluated at ambient temperature on the phase coexistence curve. In fact, when the mass flux M is nonzero, the states on both sides of the phase boundary are not on the phase coexistence curve simultaneously, and so ΔH deviates from the value at equilibrium. Strictly speaking, the value of ΔH should be calculated from the EOS of the medium. Since our implementation has complete EOS's, specifically the SPOLY EOS for the liquid, we can embed the latent heat into the EOS parameters such that ΔH can be evaluated during phase transition at the correct pressure and temperature rather than on phase coexistence curve. The details are given in Appendix A. The correction over a constant ΔH may be small, but the energy is conserved exactly at least formally. In practice if the variation of interface temperature is so large that the latent heat cannot be regarded as a constant or directly embedded into the EOS parameters, both the latent heat and the phase coexistence curve should be tabulated and coded into the EOS as extra parameters.

Since the value of M is unknown, we need one more equation to close the

system. The kinetic theory of evaporation gives the evaporation rate with a coefficient determined experimentally. The derivation below follows Alty and Mackay [3].

Under certain temperature T and pressure p, the molecular velocity of the vapor, which is treated as ideal gas, has Maxwell distribution. So the number density

$$n(\mathbf{u}) \propto \exp(-\frac{m\mathbf{u}^2}{2k_BT}),$$

where m is the molecular mass and k_B the Boltzman constant. The total mass flux of vapor molecules hitting an interface is

$$m \int \int \int_{u_x>0} du_x du_y du_z n(\mathbf{u}) u_x$$
$$= \frac{mN}{2}\bar{u}_x = \frac{mN}{4}\bar{u} = \frac{p}{\sqrt{2\pi RT}},$$

where N is the total number of molecules per unit volume and $R = k_B/m$. Not all molecules hitting the phase boundary condense into liquid. The ratio of molecules condensing into liquid over the total number hitting the phase boundary is called *evaporation coefficient* or sometimes *condensation coefficient* and denoted by α, which is a number between 0 and 1. Then the mass flux of the condensing vapor is

$$\alpha \frac{p}{\sqrt{2\pi RT}}$$

at equilibrium. Since the net mass flux cancels at equilibrium, so the mass flux of evaporating liquid is the same as that of condensing vapor. Denote

44

the equilibrium pressure at temperature T by $p_{sat}(T)$, then the mass flux of evaporating liquid is

$$\alpha \frac{p_{sat}(T)}{\sqrt{2\pi RT}}.$$

If the temperature is sufficiently lower than the critical temperature of the material, the rate at which molecules leave the liquid is not affected appreciably by the presence of surrounding vapor, so that the mass flux of evaporating liquid is still as above even when the liquid is not at equilibrium with the vapor. Therefore, the net mass flux of evaporation is

$$M_{ev} = \alpha \frac{p_{sat}(T) - p_v}{\sqrt{2\pi RT}}. \tag{4.10}$$

The measurement of α is difficult and values ranges from 0.04 [3] and below [9, 17] to 0.4 [35] and above [23]. A nice review on the experiments and theories on the evaporation coefficient can be found in [23].

To implement Eq. (4.10) in the computation we need to know the function $p_{sat}(T)$, which can be derived from the well-known Clausius-Clapeyron equation

$$\frac{\mathrm{d}P}{\mathrm{d}T} = \frac{\Delta S}{\Delta V} = \frac{L}{T(V_v - V_l)},$$

where S stands for specific entropy. Provided the exact EOS for both phases with latent heat embedded, the phase coexistence curve can be determined exactly from the EOS's as the (p, T) pairs at which the specific Gibbs energy $G = H - TS$ of both phases equal. In practice, the phase coexistence curve is often tabulated. For temperature outside the tabulated range, we can extrap-

45

olate the curve by integrating the Clausius-Clapeyron equation with a fixed L, which gives

$$p_{sat}(T) = p_{sat}(T_0) \exp(\frac{L}{R_v}(\frac{1}{T_0} - \frac{1}{T})).$$

Eqs. (4.1)–(4.10) is a closed system of equations. The normal velocity of two phases are not equal at the phase boundary. An equivalent form of the boundary condition for mass conservation Eq. (4.4) gives the normal velocity of the phase boundary,

$$U_{ph} = \frac{\Delta(\rho u_n)}{\Delta \rho}.$$

The interface is propagated at such velocity in the computation.

4.2   Alternative Forms of the Conservation Laws

4.2.1   Conservation Laws with Rotational Symmetry

When the physical problem has geometrical symmetry it is often more efficient to reduce the dimension of the system by working in cylindrical or spherical geometry. The conservation laws Eqs. (4.1)–(4.3) in planar or rotational symmetric coordinates are

$$
\begin{aligned}
\frac{\partial \rho}{\partial t} + \frac{\partial \rho u}{\partial x_i} + \alpha_i \frac{\rho u}{x_i} &= 0, \\
\frac{\partial \rho u}{\partial t} + \frac{\partial (\rho u^2 + p)}{\partial x_i} + \alpha_i \frac{\rho u^2}{x_i} &= -\rho \frac{\partial \phi}{\partial x_i}, \\
\frac{\partial \rho \mathbf{u}'}{\partial t} + \frac{\partial \rho u \mathbf{u}'}{\partial x_i} + \alpha_i \frac{\rho u \mathbf{u}'}{x_i} &= 0, \\
\frac{\partial \rho E}{\partial t} + \frac{\partial (\rho E + p)u}{\partial x_i} + \alpha_i \frac{(\rho E + p)u}{x_i} &= -\frac{\partial q}{\partial x_i} - \alpha_i \frac{q}{x_i},
\end{aligned}
\qquad (4.11)
$$

where u and $\mathbf{u}'$ are the velocities along x_i and perpendicular to x_i respectively, q is the heat flux along x_i. α_i is the geometrical constant, which is nonzero only in rotational symmetry and when x_i is the first coordinate, *i.e.* r in cylindrical or spherical coordinates. In those two cases, $\alpha = 1$ for cylindrical geometry while $\alpha = 2$ for spherical geometry. Please be aware that this geometrical constant α has nothing to do with the evaporation coefficient in Eq. (4.10), which is usually also denoted by α.

4.2.2 Conservation Laws on the Interface

The conservation laws projected into the normal direction of the interface are

$$
\begin{aligned}
\frac{\partial \rho}{\partial t} + \frac{\partial \rho u}{\partial \mathbf{n}} + \alpha N_0 \frac{\rho u}{r} &= 0, \\
\frac{\partial \rho u}{\partial t} + \frac{\partial (\rho u^2 + p)}{\partial \mathbf{n}} + \alpha N_0 \frac{\rho u^2}{r} &= -\rho \frac{\partial \phi}{\partial \mathbf{n}}, \\
\frac{\partial \rho \mathbf{u}'}{\partial t} + \frac{\partial \rho u \mathbf{u}'}{\partial \mathbf{n}} + \alpha N_0 \frac{\rho u \mathbf{u}'}{r} &= 0, \\
\frac{\partial \rho E}{\partial t} + \frac{\partial (\rho E + p)u}{\partial \mathbf{n}} + \alpha N_0 \frac{(\rho E + p)u}{r} &= -\frac{\partial q}{\partial \mathbf{n}} - \alpha N_0 \frac{q}{r},
\end{aligned}
$$

where $\mathbf{n}$ is the normal direction of the interface, u and $\mathbf{u}'$ the normal and tangential velocity respectively, q is the normal heat flux. N_0 is the x component of the $\mathbf{n}$. $\frac{\partial}{\partial \mathbf{n}}$ is the directional derivative in the direction $\mathbf{n}$. The above equations are similar to those given in [21] except for the thermal conduction

terms. The noncharacteristic version of the above equations is

$$\frac{D\rho}{Dt} + \rho(\frac{\partial u}{\partial \mathbf{n}} + \alpha N_0 \frac{u}{r}) = 0,$$

$$\frac{Du}{Dt} + \frac{1}{\rho}\frac{\partial p}{\partial \mathbf{n}} = -\frac{\partial \phi}{\partial \mathbf{n}},$$

$$\frac{D\mathbf{u}'}{Dt} = 0,$$

$$\frac{De}{Dt} + p\frac{DV}{Dt} = -\frac{1}{\rho}(\frac{\partial q}{\partial \mathbf{n}} + \alpha N_0 \frac{q}{r}),$$

where e and V are the specific internal energy and specific volume, while $\frac{D}{Dt}$ is the Lagrangian derivative

$$\frac{D}{Dt} = \frac{\partial}{\partial t} + u\frac{\partial}{\partial \mathbf{n}}.$$

A convenient form of the conservation laws at the interface for numerical algorithms is the characteristic form.

$$\frac{dp}{d\lambda_+} + \alpha N_0 \frac{\rho c^2 u}{r} + \rho c\frac{du}{d\lambda_+} = -\rho c\frac{\partial \phi}{\partial \mathbf{n}} - \Gamma(\frac{\partial q}{\partial \mathbf{n}} + \alpha N_0 \frac{q}{r}), \qquad (4.12)$$

$$\frac{dp}{d\lambda_-} + \alpha N_0 \frac{\rho c^2 u}{r} - \rho c\frac{du}{d\lambda_-} = \rho c\frac{\partial \phi}{\partial \mathbf{n}} - \Gamma(\frac{\partial q}{\partial \mathbf{n}} + \alpha N_0 \frac{q}{r}), \qquad (4.13)$$

$$\frac{d\mathbf{u}'}{d\lambda_0} = 0, \qquad (4.14)$$

$$\frac{de}{d\lambda_0} + p\frac{dV}{d\lambda_0} = -\frac{1}{\rho}(\frac{\partial q}{\partial \mathbf{n}} + \alpha N_0 \frac{q}{r}). \qquad (4.15)$$

where

$$c = \sqrt{\left(\frac{\partial p}{\partial \rho}\right)_S}$$

is the sound speed and S is the specific entropy. Γ is the Gruneisen coefficient

48

$$\Gamma = V \left(\frac{\partial p}{\partial e}\right)_V = \frac{V}{T} \left(\frac{\partial p}{\partial S}\right)_V.$$

For both POLY and SPOLY EOS's, $\Gamma = \gamma - 1$, where γ is the polytropic index.

The characteristic derivatives $\lambda_\pm$ and λ_0 are defined by

$$\frac{\mathrm{d}}{\mathrm{d}\lambda_\pm} = \frac{\partial}{\partial t} + (u \pm c)\frac{\partial}{\partial \mathbf{n}},$$
$$\frac{\mathrm{d}}{\mathrm{d}\lambda_0} = \frac{\partial}{\partial t} + u\frac{\partial}{\partial \mathbf{n}}. \tag{4.16}$$

Notice the important difference in the characteristic equations that the entropy S is no longer conserved.

From the second law of thermodynamics, $TdS = de + pdV$, Eqs. (4.12) and (4.13) can be verified as following,

$$
\begin{aligned}
&\frac{\mathrm{d}p}{\mathrm{d}\lambda_\pm} + \alpha N_0 \frac{\rho c^2 u}{r} \pm \rho c \frac{\mathrm{d}u}{\mathrm{d}\lambda_\pm} \\
= \ &\frac{Dp}{Dt} \pm c\frac{\partial p}{\partial \mathbf{n}} + \alpha N_0 \frac{\rho c^2 u}{r} \pm \rho c(\frac{Du}{Dt} \pm c\frac{\partial u}{\partial \mathbf{n}}) \\
= \ &\frac{Dp}{Dt} + \rho c^2(\frac{\partial u}{\partial \mathbf{n}} + \alpha N_0\frac{u}{r}) \pm c(\rho\frac{Du}{Dt} + \frac{\partial p}{\partial \mathbf{n}}) \\
= \ &\frac{Dp}{Dt} - c^2\frac{D\rho}{Dt} \mp \rho c\frac{\partial \phi}{\partial \mathbf{n}} \\
= \ &\frac{Dp}{Dt} - \left(\frac{\partial p}{\partial \rho}\right)_S \frac{D\rho}{Dt} \mp \rho c\frac{\partial \phi}{\partial \mathbf{n}} \\
= \ &\left(\frac{\partial p}{\partial S}\right)_\rho \frac{DS}{Dt} \mp \rho c\frac{\partial \phi}{\partial \mathbf{n}} \\
= \ &-\left(\frac{\partial p}{\partial S}\right)_V \cdot \frac{V}{T}(\frac{\partial q}{\partial \mathbf{n}} + \alpha N_0\frac{q}{r}) \mp \rho c\frac{\partial \phi}{\partial \mathbf{n}} \\
= \ &-\Gamma(\frac{\partial q}{\partial \mathbf{n}} + \alpha N_0\frac{q}{r}) \mp \rho c\frac{\partial \phi}{\partial \mathbf{n}}.
\end{aligned}
$$

49

An equivalent form of Eq. (4.15) is

$$
\begin{aligned}
-(\frac{\partial q}{\partial \mathbf{n}} + \alpha N_0 \frac{q}{r}) &= \rho(\frac{\mathrm{d}e}{\mathrm{d}\lambda_0} + p\frac{\mathrm{d}V}{\mathrm{d}\lambda_0}) \\
&= \rho\frac{\mathrm{D}H}{\mathrm{D}t} - \frac{\mathrm{D}p}{\mathrm{D}t} \\
&= \rho c_p \frac{\mathrm{D}T}{\mathrm{D}t} + (\rho \left(\frac{\partial H}{\partial p} \right)_T - 1)\frac{\mathrm{D}p}{\mathrm{D}t} \\
&= \rho c_p \frac{\mathrm{D}T}{\mathrm{D}t} - \beta T \frac{\mathrm{D}p}{\mathrm{D}t},
\end{aligned}
\tag{4.17}
$$

where β is the coefficient of thermal expansion [36],

$$
\beta = \frac{1}{V} \left(\frac{\partial V}{\partial T} \right)_p.
$$

For ideal gas $\beta T \equiv 1$. For liquid, *e.g.* water in room temperature, $\beta T \ll 1$.

If the heat flux satisfies Fourier's law of thermal conduction, *i.e.* $\mathbf{q} = -\kappa \nabla T$, then the Eqs. (4.12)–(4.15) is a parabolic system. The problem with Riemann data does not have the classical self-similar solution.

To have a flavor of the solution, let us investigate the linearized equations without gravity in one-dimensional planar geometry. For clarity the equations are listed below, in which Eq. (4.17) has been substituted for Eq. (4.15).

$$
\begin{aligned}
\frac{\partial(p + mu)}{\partial t} + c\frac{\partial(p + mu)}{\partial x} &= \Gamma\kappa\frac{\partial^2 T}{\partial x^2}, \\
\frac{\partial(p - mu)}{\partial t} - c\frac{\partial(p - mu)}{\partial x} &= \Gamma\kappa\frac{\partial^2 T}{\partial x^2}, \\
\rho c_p\frac{\partial T}{\partial t} - \beta T\frac{\partial p}{\partial t} &= \kappa\frac{\partial^2 T}{\partial x^2},
\end{aligned}
$$

where $m = \rho c$ and all other coefficients c, κ, Γ, ρc_p and βT are taken to be

constants. If $\beta T \neq 0$ and $\Gamma \neq 0$, the equations above are coupled and hard to solve analytically. On the other hand, if βT is neglected, which is justified for most liquids, the system is decoupled. We can solve the temperature equation analytically and substitute the solution for the right-hand-side of the other two equations. In this case the parabolic (temperature) field revises the hyperbolic (pressure and velocity) fields. On the other hand, if Γ is taken to be zero, then the pressure and velocity can be solved directly and substituted for the $\frac{\partial p}{\partial t}$ term in the thermal equation. Here the hyperbolic fields revise the parabolic field. If neither βT nor Γ vanishes, the two types of fields closely interact. Closed form solution hasn't been derived even for linearized equations. However, from the observation on the solution in the two special cases mentioned above, aspects of the solution in certain limits can be derived. The following is the detail.

4.3 Analytical Solution for Immiscible Fluids: Temperature Field Decoupled

First let us consider the case that βT vanishes. The temperature field is decoupled from the hyperbolic fields, and the isentropes coincide with the isotherms. Since the thermal contact is simpler than phase boundary, we will begin with thermal contact. Assume the two phases to the left and right of the origin satisfy the linearized equations with different coefficients, and the Cauchy data in each phase is constant as in the Riemann problem. More

clearly,

$$\frac{\partial(p_l + m_l u_l)}{\partial t} + c_l \frac{\partial(p_l + m_l u_l)}{\partial x} = \Gamma_l \kappa_l \frac{\partial^2 T_l}{\partial x^2}, \qquad (4.18)$$

$$\frac{\partial(p_l - m_l u_l)}{\partial t} - c_l \frac{\partial(p_l - m_l u_l)}{\partial x} = \Gamma_l \kappa_l \frac{\partial^2 T_l}{\partial x^2}, \qquad (4.19)$$

$$(\rho c_p)_l \frac{\partial T_l}{\partial t} = \kappa_l \frac{\partial^2 T_l}{\partial x^2}, \qquad (4.20)$$

$$\frac{\partial(p_r + m_r u_r)}{\partial t} + c_r \frac{\partial(p_r + m_r u_r)}{\partial x} = \Gamma_r \kappa_r \frac{\partial^2 T_r}{\partial x^2}, \qquad (4.21)$$

$$\frac{\partial(p_r - m_r u_r)}{\partial t} - c_r \frac{\partial(p_r - m_r u_r)}{\partial x} = \Gamma_r \kappa_r \frac{\partial^2 T_r}{\partial x^2}, \qquad (4.22)$$

$$(\rho c_p)_r \frac{\partial T_r}{\partial t} = \kappa_r \frac{\partial^2 T_r}{\partial x^2}, \qquad (4.23)$$

with Cauchy data

$$(p_l, u_l, T_l)(t = 0) = (p_{l0}, u_{l0}, T_{l0})$$

$$(p_r, u_r, T_r)(t = 0) = (p_{r0}, u_{r0}, T_{r0}).$$

The condition at the interface is

$$p_l(x = 0) = p_r(x = 0) \qquad (4.24)$$

$$u_l(x = 0) = u_r(x = 0) \qquad (4.25)$$

$$T_l(x = 0) = T_r(x = 0) \qquad (4.26)$$

$$\kappa_l \left(\frac{\partial T_l}{\partial x}\right)_{x=0} = \kappa_r \left(\frac{\partial T_r}{\partial x}\right)_{x=0}. \qquad (4.27)$$

4.3.1 Analytical Solution

Temperature

From Eqs. (4.20), (4.23), (4.26), (4.27) and the Cauchy data we can derive the analytical solution for the temperature field.

$$T_l(t, x) = T_m - (T_{l0} - T_m)\mathrm{erf}(\frac{x}{\sqrt{4\nu_l t}}), \tag{4.28}$$

$$T_r(t, x) = T_m + (T_{r0} - T_m)\mathrm{erf}(\frac{x}{\sqrt{4\nu_r t}}), \tag{4.29}$$

where

$$T_m = \frac{T_{l0}\sqrt{(\rho c_p \kappa)_l} + T_{r0}\sqrt{(\rho c_p \kappa)_r}}{\sqrt{(\rho c_p \kappa)_l} + \sqrt{(\rho c_p \kappa)_r}}, \tag{4.30}$$

and $\nu = \kappa/(\rho c_p)$. Erf is the error function defined as

$$\mathrm{erf}(x) = \frac{2}{\sqrt{\pi}} \int_0^x e^{-y^2} dy.$$

From Eqs. (4.28) and (4.29) we know

$$\frac{\partial^2 T_l}{\partial x^2}(t, x) = (T_{l0} - T_m)\frac{x}{\nu_l t \sqrt{4\pi \nu_l t}} e^{-\frac{x^2}{4\nu_l t}},$$

$$\frac{\partial^2 T_r}{\partial x^2}(t, x) = -(T_{r0} - T_m)\frac{x}{\nu_r t \sqrt{4\pi \nu_r t}} e^{-\frac{x^2}{4\nu_r t}}.$$
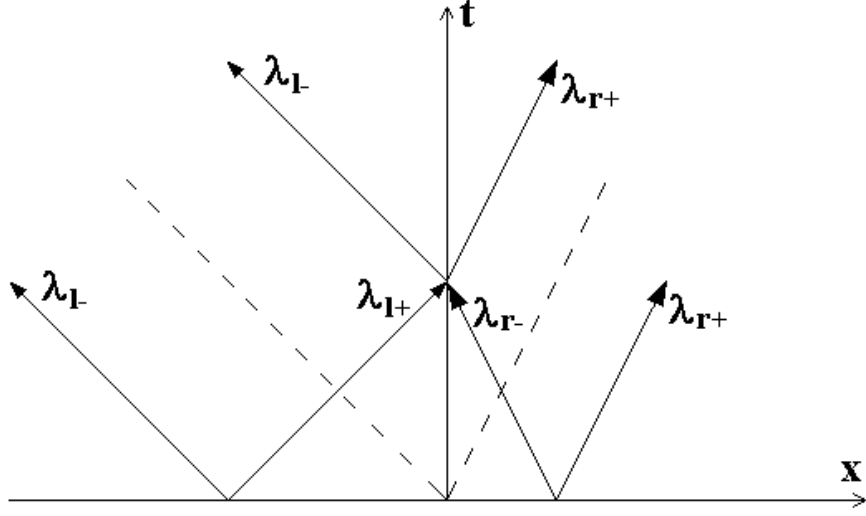
Figure 4.1: The characteristics of the linearized equations for two-phase flows.

Incoming waves

Substituting the equations into the right-hand-side of Eq. (4.18), integration along the characteristic λ_{l+} as shown in Figure 4.1, we have

$$
\begin{aligned}
& (p_l + m_l u_l)(t, x) \\
= & \ (p_l + m_l u_l)(0, x - c_l t) + \Gamma_l \kappa_l \int_0^t \frac{\partial^2 T_l}{\partial x^2}(\tau, x + c_l(\tau - t)) d\tau \\
= & \ p_{l0} + m_l u_{l0} + \Gamma_l \kappa_l (T_{l0} - T_m) \int_0^t \frac{x + c_l(\tau - t)}{\nu_l \tau \sqrt{4\pi \nu_l \tau}} e^{-\frac{(x + c_l(\tau - t))^2}{4\nu_l \tau}} d\tau,
\end{aligned}
$$

which is valid for $x < 0$.

Similarly, integrating Eq. (4.22) along the characteristic λ_{r-} in Figure

4.1, we have

$$
\begin{aligned}
& (p_r - m_r u_r)(t, x) \\
=\ & (p_r - m_r u_r)(0, x + c_r t) + \Gamma_r \kappa_r \int_0^t \frac{\partial^2 T_r}{\partial x^2}(\tau, x - c_r(\tau - t)) d\tau \\
=\ & p_{r0} - m_r u_{r0} - \Gamma_r \kappa_r (T_{r0} - T_m) \int_0^t \frac{x - c_r(\tau - t)}{\nu_r \tau \sqrt{4\pi \nu_r \tau}} e^{-\frac{(x - c_r(\tau - t))^2}{4\nu_r \tau}} d\tau,
\end{aligned}
$$

which is valid for $x > 0$.

Outgoing waves

For points below the left dashed line in Figure 4.1, *i.e.* $x < -c_l t$, we can integrate Eq. (4.19) along the characteristic λ_{l-} to obtain

$$
\begin{aligned}
& (p_l - m_l u_l)(t, x) \\
=\ & (p_l - m_l u_l)(0, x + c_l t) + \Gamma_l \kappa_l \int_0^t \frac{\partial^2 T_l}{\partial x^2}(\tau, x - c_l(\tau - t)) d\tau \\
=\ & p_{l0} - m_l u_{l0} + \Gamma_l \kappa_l (T_{l0} - T_m) \int_0^t \frac{x - c_l(\tau - t)}{\nu_l \tau \sqrt{4\pi \nu_l \tau}} e^{-\frac{(x - c_l(\tau - t))^2}{4\nu_l \tau}} d\tau.
\end{aligned}
$$

On the other hand, for points in the left half space and above the left dashed line, *i.e.* $-c_l t < x < 0$, we need to integrate from the interface, where the state is determined by the information coming along characteristics λ_{l+} and λ_{r-} and boundary conditions Eqs. (4.24) and (4.25). At the interface $x = 0$,

$$
\begin{aligned}
p(t, 0) &= \frac{m_r (p_l + m_l u_l)(t, 0) + m_l (p_r - m_r u_r)(t, 0)}{m_r + m_l}, \\
u(t, 0) &= \frac{(p_l + m_l u_l)(t, 0) - (p_r - m_r u_r)(t, 0)}{m_r + m_l}.
\end{aligned}
$$

55

So for $-c_l t < x < 0$ we have

$$
\begin{aligned}
&(p_l - m_l u_l)(t, x) \\
=\ & (p_l - m_l u_l)(t + \frac{x}{c_l}, 0) + \Gamma_l \kappa_l \int_{t + \frac{x}{c_l}}^t \frac{\partial^2 T_l}{\partial x^2}(\tau, x - c_l(\tau - t)) d\tau \\
=\ & p(t + \frac{x}{c_l}, 0) - m_l u(t + \frac{x}{c_l}, 0) + \\
& \Gamma_l \kappa_l (T_{l0} - T_m) \int_{t + \frac{x}{c_l}}^t \frac{x - c_l(\tau - t)}{\nu_l \tau \sqrt{4\pi\nu_l \tau}} e^{-\frac{(x - c_l(\tau - t))^2}{4\nu_l \tau}} d\tau.
\end{aligned}
$$

Similarly for points below the right dashed line in Figure 4.1, *i.e.* $x > c_r t$, we can integrate Eq. (4.21) along the characteristic λ_{r+} to obtain

$$
\begin{aligned}
&(p_r + m_r u_r)(t, x) \\
=\ & (p_r + m_r u_r)(0, x - c_r t) + \Gamma_r \kappa_r \int_0^t \frac{\partial^2 T_r}{\partial x^2}(\tau, x + c_r(\tau - t)) d\tau \\
=\ & p_{r0} + m_r u_{r0} - \Gamma_r \kappa_r (T_{r0} - T_m) \int_0^t \frac{x + c_r(\tau - t)}{\nu_r \tau \sqrt{4\pi\nu_r \tau}} e^{-\frac{(x + c_r(\tau - t))^2}{4\nu_r \tau}} d\tau.
\end{aligned}
$$

And for $0 < x < c_r t$,

$$
\begin{aligned}
&(p_r + m_r u_r)(t, x) \\
=\ & (p_r + m_r u_r)(t - \frac{x}{c_r}, 0) + \Gamma_r \kappa_r \int_{t - \frac{x}{c_r}}^t \frac{\partial^2 T_r}{\partial x^2}(\tau, x + c_r(\tau - t)) d\tau \\
=\ & p(t - \frac{x}{c_r}, 0) + m_r u(t - \frac{x}{c_r}, 0) - \\
& \Gamma_r \kappa_r (T_{r0} - T_m) \int_{t - \frac{x}{c_r}}^t \frac{x + c_r(\tau - t)}{\nu_r \tau \sqrt{4\pi\nu_r \tau}} e^{-\frac{(x + c_r(\tau - t))^2}{4\nu_r \tau}} d\tau.
\end{aligned}
$$

From $p_l \pm m_l u_l$ and $p_r \pm m_r u_r$ we can readily calculate p_l, u_l, p_r and u_r, thus the analytic solution of the state has been given for all space-time points.

56

4.3.2 Example

To visualize the pressure and velocity distribution let us consider the following special case.

$$(p_{l0}, u_{l0}, T_{l0}) = (0, 0, 1),$$
$$(p_{r0}, u_{r0}, T_{r0}) = (0, 0, 0). \qquad (4.31)$$

and

$$(\Gamma, \kappa, \rho c_p, c, m)_l = (1, 1, 1, 1, 1),$$
$$(\Gamma, \kappa, \rho c_p, c, m)_r = (\frac{1}{2}, \frac{1}{2}, \frac{1}{2}, \frac{1}{2}, 1). \qquad (4.32)$$

Figure 4.2 shows the plots of pressure and velocity at specific times. The pressure and velocity waves propagates at sound speed c_l to the left and c_r to the right. The wave is purely due to thermal conduction because initially the left and right side have the same pressure and are both at rest. The physical explanation for the pressure wave is simple – $T_{l0} > T_{r0}$ so there is heat flux from left to right, the pressure on the right side rises along with the temperature while the pressure on the left side decreases, which in turn induces a leftward flow. It agrees with the common sense that heat difference causes the air flow.

From Figure 4.2(a) and Figure 4.2(b) we can see that the solution is nowhere constant as contrast to the classical Riemann solution. Since the wave is propagating leftward, the left wave is shock while the right one is rarefaction. At the contact, which is fixed at origin in this case, T, p and u
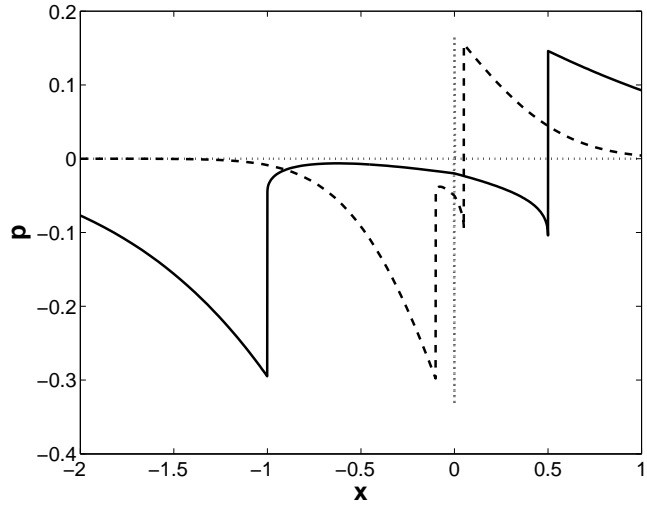
(a)
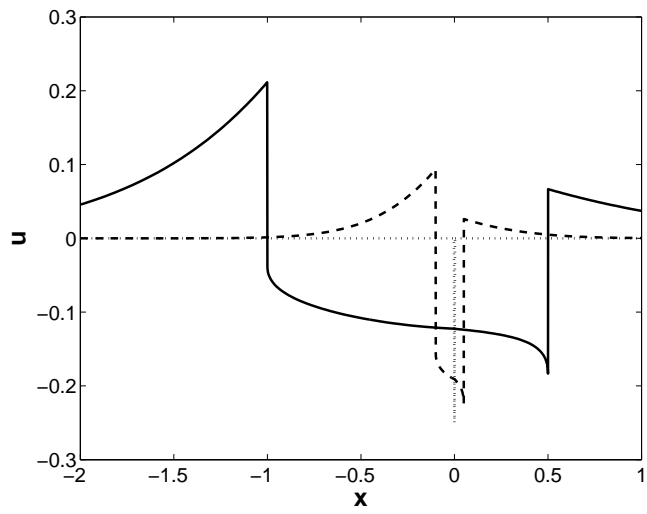
(b)

Figure 4.2: Pressure and velocity fields with initial conditions and parameters given in Eqs. (4.31) and (4.32). (a) is $p(x)$, (b) is $u(x)$. In both figures, dotted line is for $t = 0+$, dashed line is for $t = 0.1$, solid line is for $t = 1$.

are all conserved, though density and energy can have discontinuity as usual. The "mid state" is varying with both time and space, so it is not well-defined in the classical sense. However, we can investigate two limit cases, namely, $t \to \infty$ and $t \to 0$.

4.3.3 Asymptotic Solution in the Adiabatic Limit

First let us consider the case that $t \to \infty$. By scaling the conservation laws, it is easy to see that the limit $\kappa \to 0$ is equivalent to the limit that $t \to \infty$ and $x \to \infty$ simultaneously while keeping x/t unchanged. Therefore this is the limit of vanishing thermal conductivity, in other words, the *adiabatic limit*. We might expect the problem to be reduced to the classical Riemann problem in this limit, however it is not quite true due to the condition of temperature continuity that is absent in the classical Riemann problem. Figure 4.3 shows the plots of pressure and velocity with decreasing thermal conductivity κ. It is seen that the amplitude of the pressure and velocity wave does not vanish in the limit of $\kappa \to 0$, yet the width of the pressure and velocity peak approaches 0. Next we will prove it rigorously and derive the limit peak values of the pressure and velocity waves.

Thermal effect

The effect of the thermal conduction can be understood as a linear superposition onto the classical Riemann solution. If the thermal conduction is absent, then the characteristics λ_{l+} and λ_{r-} intersect at the interface and determine the mid state and thus the global piecewise constant solution struc-
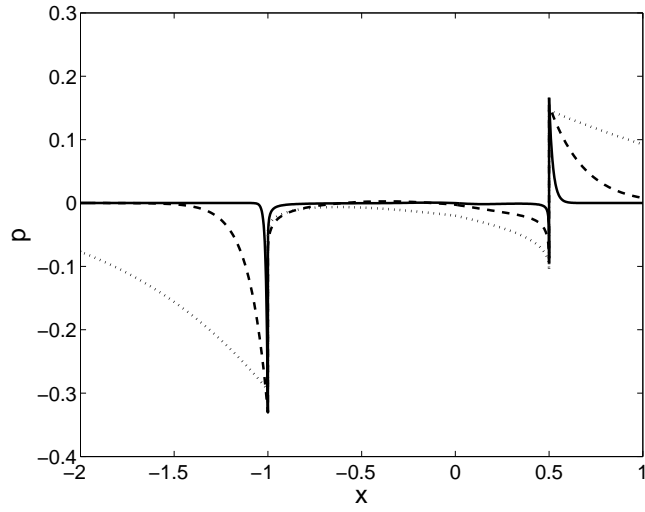
(a)
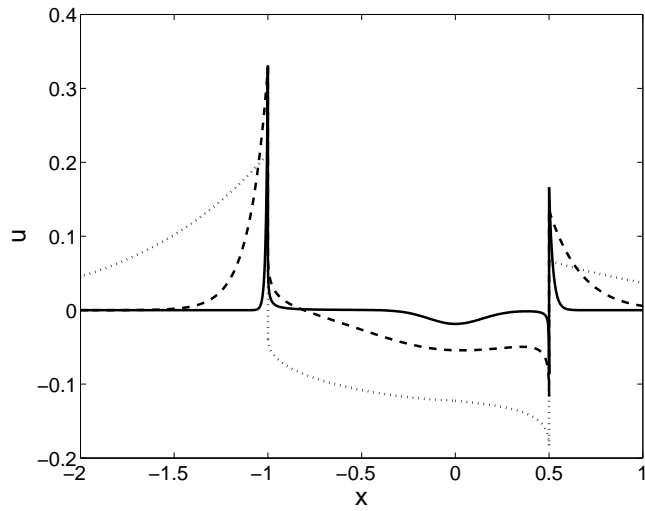
(b)

Figure 4.3: Pressure and velocity fields with various thermal conductivity. $(p_{l0}, u_{l0}, T_{l0}) = (0, 0, 1)$, $(p_{r0}, u_{r0}, T_{r0}) = (0, 0, 0)$. $(\Gamma, \rho c_p, c, m)_l = (1, 1, 1, 1)$, $(\Gamma, \rho c_p, c, m)_r = (0.5, 0.5, 0.5, 1)$. (a) is $p(x)$ at $t = 1$, (b) is $u(x)$ at $t = 1$. In both figures, dotted line is for $\kappa_l = 1$ and $\kappa_r = 0.5$, dashed line is for $\kappa_l = 0.1$ and $\kappa_r = 0.05$, solid line is for $\kappa_l = 0.01$ and $\kappa_r = 0.005$.

ture. Here we are interested in *the addition to the pressure and velocity waves from the effect of thermal conduction*, denoted by Δ_{Th}. For example,

$$\Delta_{Th}(p_l + m_l u_l)(t, x) = \Gamma_l \kappa_l (T_{l0} - T_m) \int_0^t \frac{x + c_l(\tau - t)}{\nu_l \tau \sqrt{4\pi\nu_l\tau}} e^{-\frac{(x+c_l(\tau-t))^2}{4\nu_l\tau}} d\tau.$$

and

$$\Delta_{Th} p(t, 0) = \frac{m_r \Delta_{Th}(p_l + m_l u_l)(t, 0) + m_l \Delta_{Th}(p_r - m_r u_r)(t, 0)}{m_r + m_l}.$$

Limit solution

First we prove the thermal conduction has no effect away from the shock front or rarefaction in the limit of vanishing thermal conductivity. For the waves outside the fronts ($|x| > ct$), two lemmas are proven below for the left and right going characteristics.

Lemma 4.3.1 *If $x > 0$ then*

$$\lim_{\nu \to 0} \int_0^t \frac{x - c(\tau - t)}{\tau\sqrt{4\pi\nu\tau}} \exp\left(-\frac{(x - c(\tau - t))^2}{4\nu\tau}\right) d\tau = 0$$

61

Proof:

$$\left| \lim_{\nu \to 0} \int_0^t \frac{x - c(\tau - t)}{\tau \sqrt{4\pi\nu\tau}} \exp\left(-\frac{(x - c(\tau - t))^2}{4\nu\tau}\right) d\tau \right|$$

$$\leq \lim_{\nu \to 0} \int_0^t \frac{x + ct}{\tau \sqrt{4\pi\nu\tau}} \exp\left(-\frac{x^2}{4\nu\tau}\right) d\tau$$

$$= (x + ct) \lim_{\nu \to 0} \int_0^{\nu t} \frac{ds}{s\sqrt{4\pi s}} e^{-\frac{x^2}{4s}}$$

$$= \frac{x + ct}{x} \lim_{\nu \to 0} \frac{2}{\sqrt{\pi}} \int_{\frac{x}{2\sqrt{\nu t}}}^{\infty} e^{-y^2} dy$$

$$= \frac{x + ct}{x} \lim_{\nu \to 0} \left(1 - \operatorname{erf}\left(\frac{x}{2\sqrt{\nu t}}\right)\right)$$

$$= 0.$$

Lemma 4.3.2 *If $\varepsilon = x - ct > 0$, then*

$$\lim_{\nu \to 0} \int_0^t \frac{x + c(\tau - t)}{\tau \sqrt{4\pi\nu\tau}} \exp\left(-\frac{(x + c(\tau - t))^2}{4\nu\tau}\right) d\tau = 0$$

Proof:

$$\lim_{\nu \to 0} \lim_{\varepsilon \to 0+} \int_0^t \frac{x + c(\tau - t)}{\tau \sqrt{4\pi\nu\tau}} \exp\left(-\frac{(x + c(\tau - t))^2}{4\nu\tau}\right) d\tau$$

$$= \lim_{\nu \to 0} \lim_{\varepsilon \to 0+} \int_0^t \frac{\varepsilon + c\tau}{\tau \sqrt{4\pi\nu\tau}} \exp\left(-\frac{(\varepsilon + c\tau)^2}{4\nu\tau}\right) d\tau$$

$$= \lim_{\nu \to 0} \lim_{\varepsilon \to 0+} \int_0^t \frac{\varepsilon}{\tau \sqrt{4\pi\nu\tau}} \exp\left(-\frac{(\varepsilon + c\tau)^2}{4\nu\tau}\right) d\tau$$

$$+ \lim_{\nu \to 0} \lim_{\varepsilon \to 0+} \int_0^t \frac{c}{\sqrt{4\pi\nu\tau}} \exp\left(-\frac{(\varepsilon + c\tau)^2}{4\nu\tau}\right) d\tau$$

62

The first term

$$\lim_{\nu \to 0} \int_0^t \frac{\varepsilon}{\tau \sqrt{4\pi\nu\tau}} \exp(-\frac{(\varepsilon + c\tau)^2}{4\nu\tau}) d\tau$$

$$= \frac{2}{\sqrt{\pi}} \lim_{\nu \to 0} e^{-\frac{c\varepsilon}{2\nu}} \int_{\frac{\varepsilon}{\sqrt{4\nu t}}}^{\infty} e^{-y^2} \exp(-(\frac{c\varepsilon}{4\nu y})^2) dy$$

$$= 0,$$

since the last integral is bounded and

$$\lim_{\nu \to 0} e^{-\frac{c\varepsilon}{2\nu}} = 0.$$

Similarly, the second term

$$\lim_{\nu \to 0} \int_0^t \frac{c}{\sqrt{4\pi\nu\tau}} \exp(-\frac{(\varepsilon + c\tau)^2}{4\nu\tau}) d\tau$$

$$= \frac{2}{\sqrt{\pi}} \lim_{\nu \to 0} e^{-\frac{c\varepsilon}{2\nu}} \int_0^{\frac{c}{2}\sqrt{\frac{t}{\nu}}} e^{-y^2} \exp(-(\frac{c\varepsilon}{4\nu y})^2) dy$$

$$= 0.$$

For $x > c_r t$, from Lemma 4.3.1

$$\lim_{\nu \to 0} \Delta_{Th}(p_r - m_r u_r) = 0,$$

and from Lemma 4.3.2

$$\lim_{\nu \to 0} \Delta_{Th}(p_r + m_r u_r) = 0,$$

63

so $\lim_{\nu \to 0} \Delta_{Th}(p_r) = 0$ and $\lim_{\nu \to 0} \Delta_{Th}(u_r) = 0$. The case of $x < c_l t$ is similar.

For the waves inside the fronts ($|x| < ct$), two more lemmas are needed.

Lemma 4.3.3 *For* $x = 0$,

$$\lim_{t \to \infty} \int_0^t \frac{x - c(\tau - t)}{\tau \sqrt{4\pi\nu\tau}} \exp(-\frac{(x - c(\tau - t))^2}{4\nu\tau}) d\tau = 0$$

Proof:

$$
\begin{aligned}
&\lim_{t \to \infty} \int_0^t \frac{x - c(\tau - t)}{\tau \sqrt{4\pi\nu\tau}} \exp(-\frac{(x - c(\tau - t))^2}{4\nu\tau}) d\tau \\
=\ &\lim_{t \to \infty} \int_0^t \frac{c(t - \tau)}{\tau \sqrt{4\pi\nu\tau}} \exp(-\frac{c^2(t - \tau)^2}{4\nu\tau}) d\tau \\
=\ &\frac{2}{\sqrt{\pi}} \lim_{t \to \infty} \int_{\frac{c}{2}\sqrt{\frac{t}{\nu}}}^{\infty} (1 - \frac{c^2 t}{4\nu y^2}) \exp(-y^2(1 - \frac{c^2 t}{4\nu y^2})^2) dy \\
=\ &\frac{2}{\sqrt{\pi}} \lim_{\alpha = \frac{c}{2}\sqrt{\frac{t}{\nu}} \to \infty} \int_{\alpha}^{\infty} (1 - (\frac{\alpha}{y})^2) \exp(-y^2(1 - (\frac{\alpha}{y})^2)^2) dy \\
=\ &\lim_{\alpha \to \infty} \frac{2}{\sqrt{\pi}} \int_{\alpha}^{\alpha + \sqrt[3]{\alpha}} (1 - (\frac{\alpha}{y})^2) \exp(-y^2(1 - (\frac{\alpha}{y})^2)^2) dy \\
&+ \lim_{\alpha \to \infty} \frac{2}{\sqrt{\pi}} \int_{\alpha + \sqrt[3]{\alpha}}^{\infty} (1 - (\frac{\alpha}{y})^2) \exp(-y^2(1 - (\frac{\alpha}{y})^2)^2) dy \\
\leq\ &\frac{2}{\sqrt{\pi}} \lim_{\alpha \to \infty} [\int_{\alpha}^{\alpha + \sqrt[3]{\alpha}} (1 - (\frac{\alpha}{\alpha + \sqrt[3]{\alpha}})^2) dy + \int_{\alpha + \sqrt[3]{\alpha}}^{\infty} \exp(-(y - \frac{\alpha^2}{\alpha + \sqrt[3]{\alpha}})^2) dy] \\
\leq\ &\lim_{\alpha \to \infty} [\frac{2}{\sqrt{\pi}} \frac{2}{\sqrt[3]{\alpha}} + 1 - \mathrm{erf}(\sqrt[3]{\alpha})] \\
=\ &0.
\end{aligned}
$$

Lemma 4.3.4 *If* $0 < x < ct$, *then*

$$\lim_{\nu \to 0} \int_{t - \frac{x}{c}}^t \frac{x + c(\tau - t)}{\tau \sqrt{4\pi\nu\tau}} \exp(-\frac{(x + c(\tau - t))^2}{4\nu\tau}) d\tau = 0$$

64

Proof: Denote $\varepsilon = ct - x$, we have

$$\lim_{\nu \to 0} \int_{t-\frac{x}{c}}^{t} \frac{x + c(\tau - t)}{\tau \sqrt{4\pi\nu\tau}} \exp(-\frac{(x + c(\tau - t))^2}{4\nu\tau}) d\tau$$

$$= \frac{2}{\sqrt{\pi}} \lim_{\nu \to 0} \int_0^{\frac{1}{2}\sqrt{\frac{cx}{\nu}}} dy (1 + \frac{\varepsilon c}{4\nu y^2})^{-\frac{3}{2}} \exp(-\frac{y^2}{1 + \frac{\varepsilon c}{4\nu y^2}}).$$

Obviously it is nonnegative. Since $y \le \frac{1}{2}\sqrt{\frac{cx}{\nu}}$, $1 + \frac{\varepsilon c}{4\nu y^2} \le \frac{\varepsilon c}{4\nu y^2}(1 + \frac{x}{\varepsilon})$, and so

$$\frac{2}{\sqrt{\pi}} \lim_{\nu \to 0} \int_0^{\frac{1}{2}\sqrt{\frac{cx}{\nu}}} dy (1 + \frac{\varepsilon c}{4\nu y^2})^{-\frac{3}{2}} \exp(-\frac{y^2}{1 + \frac{\varepsilon c}{4\nu y^2}}).$$

$$\le \frac{2}{\sqrt{\pi}} \lim_{\nu \to 0} \int_0^{\frac{1}{2}\sqrt{\frac{cx}{\nu}}} dy (\frac{\varepsilon c}{4\nu y^2})^{-\frac{3}{2}} \exp(-\frac{y^2}{\frac{\varepsilon c}{4\nu y^2}(1 + \frac{x}{\varepsilon})}).$$

$$= \lim_{\nu \to 0} \frac{\varepsilon + x}{\varepsilon} \sqrt{\frac{\nu}{\pi\varepsilon c}} (1 - \exp(-\frac{c}{4\nu} \frac{x^2}{\varepsilon + x}))$$

$$= 0.$$

For $0 < x < c_r t$, first applying Lemma 4.3.3 on both sides (along λ_{l+} and λ_{r-}) we see $\lim_{\nu \to 0} \Delta_{Th}(p_{bd}) = 0$ and $\lim_{\nu \to 0} \Delta_{Th}(u_{bd}) = 0$, where p_{bd} and u_{bd} stand for the pressure and velocity on the interface. Then from Lemma 4.3.1 and Lemma 4.3.4 we draw the same conclusion as for $x > c_r t$. The case of $-c_l t < x < 0$ is similar. As a summary, away from the shock front or rarefaction, the thermal conduction has no effect in the limit of vanishing thermal conductivity. However it is not so at the front. Again we consider waves outside the fronts first.

Lemma 4.3.5 *If $x = ct$ then*

$$\lim_{\nu \to 0} \int_0^t \frac{x + c(\tau - t)}{\tau \sqrt{4\pi\nu\tau}} \exp(-\frac{(x + c(\tau - t))^2}{4\nu\tau}) d\tau = 1$$

Proof:

$$\lim_{\nu \to 0} \int_0^t \frac{x + c(\tau - t)}{\tau \sqrt{4\pi\nu\tau}} \exp(-\frac{(x + c(\tau - t))^2}{4\nu\tau}) d\tau$$

$$= \lim_{\nu \to 0} \int_0^t \frac{c}{\sqrt{4\pi\nu\tau}} e^{-\frac{c^2}{4\nu}\tau} d\tau$$

$$= \frac{2}{\sqrt{\pi}} \lim_{\nu \to 0} \int_0^{\frac{c}{2}\sqrt{\frac{t}{\nu}}} e^{-y^2} dy$$

$$= \lim_{\nu \to 0} \text{erf}(\frac{c}{2}\sqrt{\frac{t}{\nu}})$$

$$= 1.$$

Lemma 4.3.6 *Define $\varepsilon = x - ct$, then*

$$\lim_{\nu \to 0} \lim_{\varepsilon \to 0+} \int_0^t \frac{x + c(\tau - t)}{\tau \sqrt{4\pi\nu\tau}} \exp(-\frac{(x + c(\tau - t))^2}{4\nu\tau}) d\tau = 2$$

Proof: As the proof of Lemma 4.3.2, the integral can be written as the sum of

two terms. Now the first term

$$\lim_{\nu \to 0} \lim_{\varepsilon \to 0+} \int_0^t \frac{\varepsilon}{\tau\sqrt{4\pi\nu\tau}} \exp(-\frac{(\varepsilon + c\tau)^2}{4\nu\tau}) d\tau$$

$$= \frac{2}{\sqrt{\pi}} \lim_{\nu \to 0} \lim_{\varepsilon \to 0+} \int_{\frac{\varepsilon}{\sqrt{4\nu t}}}^{\infty} \exp(-(y + \frac{c\varepsilon}{4\nu y})^2) dy$$

$$= \frac{2}{\sqrt{\pi}} \lim_{\nu \to 0} \lim_{\varepsilon \to 0+} e^{-\frac{c\varepsilon}{2\nu}} \int_{\frac{\varepsilon}{\sqrt{4\nu t}}}^{\infty} e^{-y^2} \exp(-(\frac{c\varepsilon}{4\nu y})^2) dy$$

$$= \frac{2}{\sqrt{\pi}} \lim_{\nu \to 0} \lim_{\varepsilon \to 0+} \int_{\frac{\varepsilon}{\sqrt{4\nu t}}}^{\infty} e^{-y^2} \exp(-(\frac{c\varepsilon}{4\nu y})^2) dy.$$

It is bounded from above by $\operatorname{erf}(\infty) = 1$. *We can show it is also bounded from below by 1. Indeed,*

$$\frac{2}{\sqrt{\pi}} \lim_{\nu \to 0} \lim_{\varepsilon \to 0+} \int_{\frac{\varepsilon}{\sqrt{4\nu t}}}^{\infty} e^{-y^2} \exp(-(\frac{c\varepsilon}{4\nu y})^2) dy.$$

$$\geq \frac{2}{\sqrt{\pi}} \lim_{\nu \to 0} \lim_{\varepsilon \to 0+} \int_{\max(\frac{\varepsilon}{\sqrt{4\nu t}}, \sqrt{\frac{c\varepsilon}{4\nu}})}^{\infty} e^{-y^2} \exp(-(\frac{c\varepsilon}{4\nu y})^2) dy$$

$$\geq \frac{2}{\sqrt{\pi}} \lim_{\nu \to 0} \lim_{\varepsilon \to 0+} e^{-\frac{c\varepsilon}{4\nu}} \int_{\max(\frac{\varepsilon}{\sqrt{4\nu t}}, \sqrt{\frac{c\varepsilon}{4\nu}})}^{\infty} e^{-y^2} dy$$

$$= \lim_{\nu \to 0} \lim_{\varepsilon \to 0+} e^{-\frac{c\varepsilon}{4\nu}} (1 - \operatorname{erf}(\max(\frac{\varepsilon}{\sqrt{4\nu t}}, \sqrt{\frac{c\varepsilon}{4\nu}})))$$

$$= 1.$$

Comparing the second term with Lemma 4.3.5 we can see that it is bounded

from above by 1. Similarly it is also bounded from below by 1. Indeed,

$$\lim_{\nu \to 0} \lim_{\varepsilon \to 0+} \int_0^t \frac{c}{\sqrt{4\pi\nu\tau}} \exp(-\frac{(\varepsilon + c\tau)^2}{4\nu\tau}) d\tau$$

$$= \frac{2}{\sqrt{\pi}} \lim_{\nu \to 0} \lim_{\varepsilon \to 0+} \int_0^{\frac{c}{2}\sqrt{\frac{t}{\nu}}} \exp(-(y + \frac{c\varepsilon}{4\nu y})^2) dy$$

$$= \frac{2}{\sqrt{\pi}} \lim_{\nu \to 0} \lim_{\varepsilon \to 0+} e^{-\frac{c\varepsilon}{2\nu}} \int_0^{\frac{c}{2}\sqrt{\frac{t}{\nu}}} e^{-y^2} \exp(-(\frac{c\varepsilon}{4\nu y})^2) dy$$

$$\geq \frac{2}{\sqrt{\pi}} \lim_{\nu \to 0} \lim_{\varepsilon \to 0+} \int_{\sqrt{\frac{c\varepsilon}{4\nu}}}^{\frac{c}{2}\sqrt{\frac{t}{\nu}}} e^{-y^2} \exp(-(\frac{c\varepsilon}{4\nu y})^2) dy$$

$$\geq \frac{2}{\sqrt{\pi}} \lim_{\nu \to 0} \lim_{\varepsilon \to 0+} e^{-\frac{c\varepsilon}{4\nu}} \int_{\sqrt{\frac{c\varepsilon}{4\nu}}}^{\frac{c}{2}\sqrt{\frac{t}{\nu}}} e^{-y^2} dy$$

$$= \lim_{\nu \to 0} \lim_{\varepsilon \to 0+} e^{-\frac{c\varepsilon}{4\nu}} (\mathrm{erf}(\frac{c}{2}\sqrt{\frac{t}{\nu}}) - \mathrm{erf}(\sqrt{\frac{c\varepsilon}{4\nu}}))$$

$$= 1.$$

First let $x - c_r t \to 0+$ for the right wave. Lemma 4.3.1 gives

$$\lim_{\nu \to 0} \lim_{x - c_r t \to 0+} \Delta_{Th}(p_r - m_r u_r) = 0$$

as before. Yet Lemma 4.3.6 gives

$$\lim_{\nu \to 0} \lim_{x - c_r t \to 0+} \Delta_{Th}(p_r + m_r u_r) = 2\Gamma_r (\rho c_p)_r (T_m - T_{r0}).$$

68

Therefore

$$\lim_{\nu\to 0}\lim_{x-c_r t\to 0+}\Delta_{Th}p_r = \Gamma_r(\rho c_p)_r(T_m - T_{r0})$$

$$= \Gamma_r(\rho c_p)_r(T_{l0} - T_{r0})\frac{\sqrt{(\rho c_p \kappa)_l}}{\sqrt{(\rho c_p \kappa)_l} + \sqrt{(\rho c_p \kappa)_r}}$$

$$\lim_{\nu\to 0}\lim_{x-c_r t\to 0+}\Delta_{Th}u_r = \frac{1}{m_r}\Gamma_r(\rho c_p)_r(T_m - T_{r0})$$

$$= \frac{1}{m_r}\Gamma_r(\rho c_p)_r(T_{l0} - T_{r0})\frac{\sqrt{(\rho c_p \kappa)_l}}{\sqrt{(\rho c_p \kappa)_l} + \sqrt{(\rho c_p \kappa)_r}}.$$

Similarly for the left wave,

$$\lim_{\nu\to 0}\lim_{x+c_l t\to 0-}\Delta_{Th}p_l = \Gamma_l(\rho c_p)_l(T_{r0} - T_{l0})\frac{\sqrt{(\rho c_p \kappa)_r}}{\sqrt{(\rho c_p \kappa)_l} + \sqrt{(\rho c_p \kappa)_r}}$$

$$\lim_{\nu\to 0}\lim_{x+c_l t\to 0-}\Delta_{Th}u_l = -\frac{1}{m_l}\Gamma_l(\rho c_p)_l(T_{r0} - T_{l0})\frac{\sqrt{(\rho c_p \kappa)_r}}{\sqrt{(\rho c_p \kappa)_l} + \sqrt{(\rho c_p \kappa)_r}},$$

For the height of waves inside the fronts, two more lemmas are needed.

Lemma 4.3.7 *For $0 < x < ct$, denote $\varepsilon = ct - x$, we have*

$$\lim_{\nu\to 0}\lim_{\varepsilon\to 0+}\int_{t-\frac{x}{c}}^{t}\frac{x + c(\tau - t)}{\tau\sqrt{4\pi\nu\tau}}\exp(-\frac{(x + c(\tau - t))^2}{4\nu\tau})d\tau = 1$$

69

Proof: Denote $\varepsilon = ct - x$, we have

$$\lim_{\nu \to 0} \lim_{\varepsilon \to 0+} \int_{t-\frac{x}{c}}^{t} \frac{x + c(\tau - t)}{\tau\sqrt{4\pi\nu\tau}} \exp(-\frac{(x + c(\tau - t))^2}{4\nu\tau}) d\tau$$

$$= \frac{2}{\sqrt{\pi}} \lim_{\nu \to 0} \lim_{\varepsilon \to 0+} \int_{0}^{\frac{1}{2}\sqrt{\frac{cx}{\nu}}} dy (1 + \frac{\varepsilon c}{4\nu y^2})^{-\frac{3}{2}} \exp(-\frac{y^2}{1 + \frac{\varepsilon c}{4\nu y^2}})$$

$$= \frac{2}{\sqrt{\pi}} \lim_{\nu \to 0} \lim_{\varepsilon \to 0+} \int_{0}^{\sqrt[3]{\frac{\varepsilon c}{4\nu}}} dy (1 + \frac{\varepsilon c}{4\nu y^2})^{-\frac{3}{2}} \exp(-\frac{y^2}{1 + \frac{\varepsilon c}{4\nu y^2}})$$

$$+ \frac{2}{\sqrt{\pi}} \lim_{\nu \to 0} \lim_{\varepsilon \to 0+} \int_{\sqrt[3]{\frac{\varepsilon c}{4\nu}}}^{\frac{1}{2}\sqrt{\frac{cx}{\nu}}} dy (1 + \frac{\varepsilon c}{4\nu y^2})^{-\frac{3}{2}} \exp(-\frac{y^2}{1 + \frac{\varepsilon c}{4\nu y^2}}).$$

The first term vanishes since the integral domain width vanishes in the limit $\varepsilon \to 0$. In the second term

$$\frac{\varepsilon}{x} \leq \frac{\varepsilon c}{4\nu y^2} \leq \sqrt[3]{\frac{\varepsilon c}{4\nu}},$$

so the second term equals

$$\frac{2}{\sqrt{\pi}} \lim_{\nu \to 0} \lim_{\varepsilon \to 0+} \int_{\sqrt[3]{\frac{\varepsilon c}{4\nu}}}^{\frac{1}{2}\sqrt{\frac{cx}{\nu}}} dy e^{-y^2} = 1.$$

Lemma 4.3.8 *For $x = 0$,*

$$\lim_{t \to 0} \int_{0}^{t} \frac{x - c(\tau - t)}{\tau\sqrt{4\pi\nu\tau}} \exp(-\frac{(x - c(\tau - t))^2}{4\nu\tau}) d\tau = 1$$

70

Proof:

$$\lim_{t \to 0} \int_0^t \frac{x - c(\tau - t)}{\tau \sqrt{4\pi\nu\tau}} \exp(-\frac{(x - c(\tau - t))^2}{4\nu\tau}) d\tau$$

$$= \frac{2}{\sqrt{\pi}} \lim_{\alpha = \frac{c}{2}\sqrt{\frac{t}{\nu}} \to 0} \int_\alpha^\infty (1 - (\frac{\alpha}{y})^2) \exp(-y^2(1 - (\frac{\alpha}{y})^2)^2) dy.$$

As we have done several times the domain of the integral can be divided into two subdomains, namely, $[\alpha, \sqrt{\alpha}]$ and $[\sqrt{\alpha}, \infty)$. The integral in the first subdomain vanishes in the limit of $\alpha \to 0$, while the one in the second subdomain approaches $\lim_{\alpha \to 0} 1 - \mathrm{erf}(\alpha) = 1$ since $(\frac{\alpha}{y})^2 < \alpha$ in the subdomain.

Note: In this lemma, the limit is taken at $t \to 0$ unlike the limit of $\nu \to 0$ in all previous lemmas.

Let $x - c_r t \to 0-$ for the right wave. Lemma 4.3.8 applied on the right side along λ_{r-} gives

$$\lim_{t \to 0} \Delta_{Th}(p_r - m_r u_r)(t, 0) = \Gamma_r (\rho c_p)_r (T_m - T_{r0}),$$

and applied on the left side along λ_{l+} gives

$$\lim_{t \to 0} \Delta_{Th}(p_l + m_l u_l)(t, 0) = \Gamma_l (\rho c_p)_l (T_m - T_{l0}).$$

So

$$\lim_{t \to 0} \Delta_{Th} p(t, 0) = \frac{m_r \Gamma_l (\rho c_p)_l (T_m - T_{l0}) + m_l \Gamma_r (\rho c_p)_r (T_m - T_{r0})}{m_r + m_l},$$

and

$$\lim_{t \to 0} \Delta_{Th} u(t, 0) = \frac{\Gamma_l (\rho c_p)_l (T_m - T_{l0}) - \Gamma_r (\rho c_p)_r (T_m - T_{r0})}{m_r + m_l}.$$

Applying Lemma 4.3.7 we have

$$\lim_{\nu \to 0} \lim_{x - c_r t \to 0-} \Delta_{Th}(p_r + m_r u_r)$$

$$= \lim_{\nu \to 0}[\lim_{t \to 0} \Delta_{Th} p(t, 0) + m_r \lim_{t \to 0} \Delta_{Th} u(t, 0)] + \Gamma_r(\rho c_p)_r(T_m - T_{r0})$$

$$= \frac{m_r \Gamma_l(\rho c_p)_l(T_m - T_{l0}) + m_l \Gamma_r(\rho c_p)_r(T_m - T_{r0})}{m_r + m_l}$$

$$+ m_r \frac{\Gamma_l(\rho c_p)_l(T_m - T_{l0}) - \Gamma_r(\rho c_p)_r(T_m - T_{r0})}{m_r + m_l} + \Gamma_r(\rho c_p)_r(T_m - T_{r0})$$

$$= 2\frac{m_r \Gamma_l(\rho c_p)_l(T_m - T_{l0}) + m_l \Gamma_r(\rho c_p)_r(T_m - T_{r0})}{m_r + m_l}.$$

Using Lemma 4.3.1 again we have

$$\lim_{\nu \to 0} \lim_{x \to c_r t-} \Delta_{Th} p_r = \frac{m_r \Gamma_l(\rho c_p)_l(T_m - T_{l0}) + m_l \Gamma_r(\rho c_p)_r(T_m - T_{r0})}{m_r + m_l}$$

$$= \frac{T_{r0} - T_{l0}}{m_r + m_l} \frac{\Gamma_l(\rho c_p)_l m_r \sqrt{(\rho c_p \kappa)_r} - \Gamma_r(\rho c_p)_r m_l \sqrt{(\rho c_p \kappa)_l}}{\sqrt{(\rho c_p \kappa)_l} + \sqrt{(\rho c_p \kappa)_r}}$$

$$\lim_{\nu \to 0} \lim_{x \to c_r t-} \Delta_{Th} u_r = \frac{T_{r0} - T_{l0}}{m_r(m_r + m_l)} \frac{\Gamma_l(\rho c_p)_l m_r \sqrt{(\rho c_p \kappa)_r} - \Gamma_r(\rho c_p)_r m_l \sqrt{(\rho c_p \kappa)_l}}{\sqrt{(\rho c_p \kappa)_l} + \sqrt{(\rho c_p \kappa)_r}}.$$

Similarly for the left wave inside the front,

$$\lim_{\nu \to 0} \lim_{x \to -c_l t+} \Delta_{Th} p_l = \lim_{\nu \to 0} \lim_{x \to c_r t-} \Delta_{Th} p_r$$

$$= \frac{T_{r0} - T_{l0}}{m_r + m_l} \frac{\Gamma_l(\rho c_p)_l m_r \sqrt{(\rho c_p \kappa)_r} - \Gamma_r(\rho c_p)_r m_l \sqrt{(\rho c_p \kappa)_l}}{\sqrt{(\rho c_p \kappa)_l} + \sqrt{(\rho c_p \kappa)_r}}$$

$$\lim_{\nu \to 0} \lim_{x \to -c_l t+} \Delta_{Th} u_l = -\frac{T_{r0} - T_{l0}}{m_l(m_r + m_l)} \frac{\Gamma_l(\rho c_p)_l m_r \sqrt{(\rho c_p \kappa)_r} - \Gamma_r(\rho c_p)_r m_l \sqrt{(\rho c_p \kappa)_l}}{\sqrt{(\rho c_p \kappa)_l} + \sqrt{(\rho c_p \kappa)_r}}.$$

For visualization the schematic of the eight lemmas is shown in Figure 4.4. Each line corresponds to a lemma. The number on each line is the normalized
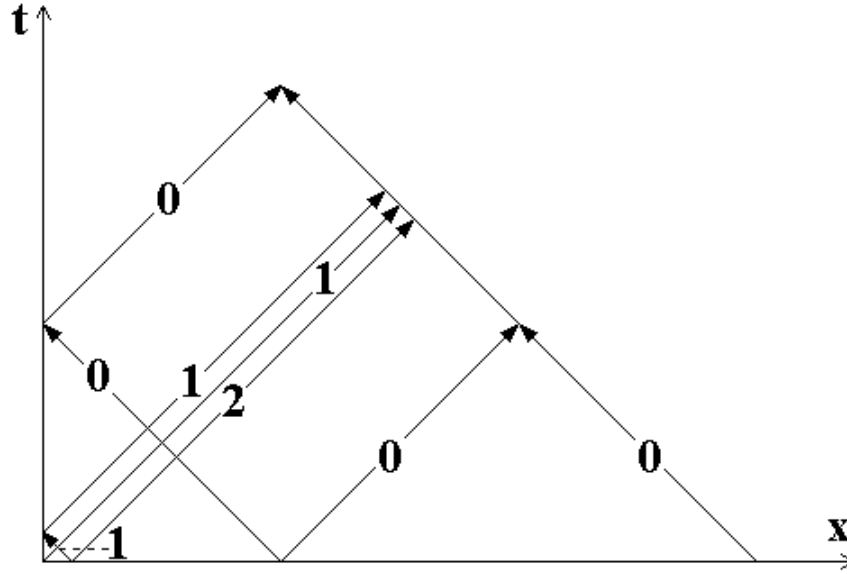
Figure 4.4: Schematic of the eight lemmas. Each line corresponds to a lemma. The number on each line is the normalized integral of T_{xx} along the characteristic, or equivalently, the normalized Δ_{Th} of the Riemann invariants.

integral of T_{xx} along the line, representing the thermal contribution to the change of the Riemann invariants.

We can compare the results listed above with the example given in Section 4.3.2. From Figure 4.3 it is clear that the width of the pressure and velocity peaks approaches zero in the adiabatic limit. The peak values given in the

previous formulas are

$$
\begin{aligned}
\lim_{\nu \to 0} \lim_{x-c_r t \to 0+} \Delta_{Th} p_r &= \frac{1}{6}, & \lim_{\nu \to 0} \lim_{x-c_r t \to 0+} \Delta_{Th} u_r &= \frac{1}{6}; \\
\lim_{\nu \to 0} \lim_{x-c_r t \to 0-} \Delta_{Th} p_r &= -\frac{1}{12}, & \lim_{\nu \to 0} \lim_{x-c_r t \to 0-} \Delta_{Th} u_r &= -\frac{1}{12}; \\
\lim_{\nu \to 0} \lim_{x+c_l t \to 0-} \Delta_{Th} p_l &= -\frac{1}{3}, & \lim_{\nu \to 0} \lim_{x+c_l t \to 0-} \Delta_{Th} u_l &= \frac{1}{3}; \\
\lim_{\nu \to 0} \lim_{x+c_l t \to 0+} \Delta_{Th} p_l &= -\frac{1}{12}, & \lim_{\nu \to 0} \lim_{x+c_l t \to 0+} \Delta_{Th} u_l &= \frac{1}{12}.
\end{aligned}
$$

They all agree with the solutions shown in Figure 4.3. The peak on the mid side of the left shock front is invisible because it has the same sign as the peak value on the other side of the front.

We can further investigate the profile of the pressure peak in the adiabatic limit. We prove below that the width of the pressure peaks in the adiabatic limit is ν/c rather than $\sqrt{\nu t}$, which is the width of the thermal layer at interface.

Lemma 4.3.9 *If $x > ct$ and $\varepsilon = x - ct = k\frac{\nu}{c}$, then*

$$
\lim_{\nu \to 0} \int_0^t \frac{x + c(\tau - t)}{\tau \sqrt{4\pi\nu\tau}} \exp\left(-\frac{(x + c(\tau - t))^2}{4\nu\tau}\right) d\tau = 2e^{-k}.
$$

Proof: As in Lemma 4.3.6,

$$
\begin{aligned}
&\lim_{\nu \to 0} \int_0^t \frac{x + c(\tau - t)}{\tau \sqrt{4\pi\nu\tau}} \exp\left(-\frac{(x + c(\tau - t))^2}{4\nu\tau}\right) d\tau \\
&= \lim_{\nu \to 0} \int_0^t \frac{\varepsilon}{\tau \sqrt{4\pi\nu\tau}} \exp\left(-\frac{(\varepsilon + c\tau)^2}{4\nu\tau}\right) d\tau + \lim_{\nu \to 0} \int_0^t \frac{c}{\sqrt{4\pi\nu\tau}} \exp\left(-\frac{(\varepsilon + c\tau)^2}{4\nu\tau}\right) d\tau
\end{aligned}
$$

74

The first term

$$\lim_{\nu \to 0} \int_0^t \frac{\varepsilon}{\tau \sqrt{4\pi\nu\tau}} \exp(-\frac{(\varepsilon + c\tau)^2}{4\nu\tau}) d\tau$$

$$= \frac{2}{\sqrt{\pi}} \lim_{\nu \to 0} e^{-\frac{c\varepsilon}{2\nu}} \int_{\frac{\varepsilon}{\sqrt{4\nu t}}}^{\infty} e^{-y^2} \exp(-(\frac{c\varepsilon}{4\nu y})^2) dy$$

$$= \frac{2}{\sqrt{\pi}} \lim_{\nu \to 0} e^{-\frac{k}{2}} \int_{\frac{k}{c}\sqrt{\frac{\nu}{4t}}}^{\infty} e^{-y^2} \exp(-(\frac{k}{4y})^2) dy$$

$$= e^{-\frac{k}{2}} \frac{2}{\sqrt{\pi}} \int_0^{\infty} e^{-y^2} \exp(-(\frac{k}{4y})^2) dy.$$

We can do the integration as following. Let

$$I(k) = \frac{2}{\sqrt{\pi}} \int_0^{\infty} e^{-y^2} \exp(-(\frac{k}{4y})^2) dy.$$

We know $I(0) = \mathrm{erf}(\infty) = 1$, *and*

$$I'(k) = \frac{2}{\sqrt{\pi}} \int_0^{\infty} e^{-y^2} \exp(-(\frac{k}{4y})^2)(-\frac{k}{8y^2}) dy$$

$$= -\frac{2}{\sqrt{\pi}} \int_0^{\infty} \exp(-(\frac{k}{4z})^2) e^{-z^2} \frac{dz}{2}$$

$$= -\frac{1}{2} I(k).$$

So $I(k) = \exp(-\frac{k}{2})$ *and the first term is* e^{-k}.

Similarly, the second term

$$\lim_{\nu \to 0} \int_0^t \frac{c}{\sqrt{4\pi\nu\tau}} \exp(-\frac{(\varepsilon + c\tau)^2}{4\nu\tau}) d\tau$$

$$= \frac{2}{\sqrt{\pi}} \lim_{\nu \to 0} e^{-\frac{c\varepsilon}{2\nu}} \int_0^{\frac{c}{2}\sqrt{\frac{t}{\nu}}} e^{-y^2} \exp(-(\frac{c\varepsilon}{4\nu y})^2) dy$$

$$= e^{-\frac{k}{2}} I(k)$$

$$= e^{-k}.$$

From Lemma 4.3.1 and 4.3.9 we know for $x > c_r t$ and $\frac{(x-c_r t)c_r}{\nu_r}$ fixed,

$$\lim_{\nu \to 0} \Delta_{Th} p_r(t,x) = \Gamma_r(\rho c_p)_r(T_m - T_{r0}) \exp(-\frac{c_r}{\nu_r}(x - c_r t)),$$

$$\lim_{\nu \to 0} \Delta_{Th} p_r(t,x) = \frac{1}{m_r} \Gamma_r(\rho c_p)_r(T_m - T_{r0}) \exp(-\frac{c_r}{\nu_r}(x - c_r t)).$$

Similar formula can be written for the left waves. The profiles of pressure and velocity peaks on the mid state side are more complicated integral forms rather than exponential function, yet the width of the peaks are also of the order of ν/c.

To summarize it, in the limit of vanishing thermal conductivity, the pressure and velocity waves are the same as in the classical Riemann solution except near the wave fronts, where the peak values can be calculated directly from the initial conditions and thermodynamic parameters for the linearized system, and the widths of the peaks are of order ν/c.

4.3.4   Asymptotic Solution in the Isothermal Limit

Next let us investigate the asymptotic solution as $t \to 0$ while all parameters are fixed. It is equivalent to the limit of $\nu \to \infty$ after certain scaling, so it can also be called the *isothermal* limit. In our linearized system, we are looking for $\lim_{t \to 0} T(t, 0)$, $\lim_{t \to 0} p(t, 0)$ and $\lim_{t \to 0} u(t, 0)$ with piecewise constant initial conditions. Although it seems like the classical Riemann problem, the intrinsic non-localness of parabolic equation (propagation speed is infinity) changes the solution quite a bit. Without heat conduction the mid state of the Riemann problem gives continuous pressure and velocity but *discontinuous* temperature at the contact, while with heat conduction the temperature is forced to be continuous at the contact, whose value is given in Eq. (4.30). The subsequent temperature wave shifts the contact pressure and velocity from the classical mid state. The difference is the Δ_{Th} of the corresponding quantity, whose values are actually already given in the previous section.

$$
\begin{aligned}
\lim_{t \to 0} T(t, 0) &= T_m = \frac{T_{l0}\sqrt{(\rho c_p \kappa)_l} + T_{r0}\sqrt{(\rho c_p \kappa)_r}}{\sqrt{(\rho c_p \kappa)_l} + \sqrt{(\rho c_p \kappa)_r}}, \\
\lim_{t \to 0} \Delta_{Th} p(t, 0) &= \frac{m_r \Gamma_l (\rho c_p)_l (T_m - T_{l0}) + m_l \Gamma_r (\rho c_p)_r (T_m - T_{r0})}{m_r + m_l} \\
&= (T_{r0} - T_{l0}) \frac{m_r \Gamma_l (\rho c_p)_l \sqrt{(\rho c_p \kappa)_r} - m_l \Gamma_r (\rho c_p)_r \sqrt{(\rho c_p \kappa)_l}}{(m_r + m_l)(\sqrt{(\rho c_p \kappa)_l} + \sqrt{(\rho c_p \kappa)_r})}, \\
\lim_{t \to 0} \Delta_{Th} u(t, 0) &= \frac{\Gamma_l (\rho c_p)_l (T_m - T_{l0}) - \Gamma_r (\rho c_p)_r (T_m - T_{r0})}{m_r + m_l} \\
&= (T_{r0} - T_{l0}) \frac{\Gamma_l (\rho c_p)_l \sqrt{(\rho c_p \kappa)_r} + \Gamma_r (\rho c_p)_r \sqrt{(\rho c_p \kappa)_l}}{(m_r + m_l)(\sqrt{(\rho c_p \kappa)_l} + \sqrt{(\rho c_p \kappa)_r})}. \quad (4.33)
\end{aligned}
$$

We can compare these results with the example given in Section 4.3.2.

The formulas above predicts

$$\lim_{t \to 0} T(t, 0) = \frac{2}{3},$$

$$\lim_{t \to 0} \Delta_{Th} p(t, 0) = -\frac{1}{12},$$

$$\lim_{t \to 0} \Delta_{Th} u(t, 0) = -\frac{1}{4},$$

which agree with the $t = 0$ curves in Figure 4.2.

We can also investigate the profile of the pressure wave in the limit of $t \to 0$. At time t the width of the pressure and velocity waves at the origin is of order $\sqrt{\nu t}$, and the wave front has moved by $ct \ll \sqrt{\nu t}$, so the wave profile is dominated by the thermal conduction. We can derive the exact profile as following.

Lemma 4.3.10 *For $x = k\sqrt{\nu t}$,*

$$\lim_{t \to 0} \int_0^t \frac{x + c(\tau - t)}{\tau \sqrt{4\pi\nu\tau}} \exp(-\frac{(x + c(\tau - t))^2}{4\nu\tau}) d\tau = 1 - \text{erf}(\frac{k}{2}).$$

Proof: Denote $x - ct$ by ε as usual,

$$\lim_{t \to 0} \int_0^t \frac{x + c(\tau - t)}{\tau \sqrt{4\pi\nu\tau}} \exp(-\frac{(x + c(\tau - t))^2}{4\nu\tau}) d\tau$$

$$= \lim_{t \to 0} \int_0^t \frac{\varepsilon}{\tau \sqrt{4\pi\nu\tau}} \exp(-\frac{(\varepsilon + c\tau)^2}{4\nu\tau}) d\tau + \lim_{t \to 0} \int_0^t \frac{c}{\sqrt{4\pi\nu\tau}} \exp(-\frac{(\varepsilon + c\tau)^2}{4\nu\tau}) d\tau$$

78

The first term

$$
\lim_{t \to 0} \int_0^t \frac{\varepsilon}{\tau \sqrt{4\pi\nu\tau}} \exp(-\frac{(\varepsilon + c\tau)^2}{4\nu\tau}) d\tau
$$

$$
= \frac{2}{\sqrt{\pi}} \lim_{t \to 0} e^{-\frac{c\varepsilon}{2\nu}} \int_{\frac{\varepsilon}{\sqrt{4\nu t}}}^{\infty} e^{-y^2} \exp(-(\frac{c\varepsilon}{4\nu y})^2) dy
$$

$$
= \frac{2}{\sqrt{\pi}} \int_{\frac{k}{2}}^{\infty} e^{-y^2} dy
$$

$$
= 1 - \operatorname{erf}(\frac{k}{2}).
$$

Similarly, the second term is zero.

Since the lemma is independent of c, for $x = k\sqrt{\nu t}$ we also have

$$
\lim_{t \to 0} \int_0^t \frac{x - c(\tau - t)}{\tau \sqrt{4\pi\nu\tau}} \exp(-\frac{(x - c(\tau - t))^2}{4\nu\tau}) d\tau = 1 - \operatorname{erf}(\frac{k}{2}).
$$

Therefore, as $x/\sqrt{\nu_r t}$ is fixed,

$$
\lim_{t \to 0} \Delta_{Th} p_r(t, x) = \Gamma_r(\rho c_p)_r(T_m - T_{r0})(1 - \operatorname{erf}(\frac{x}{2\sqrt{\nu_r t}})),
$$

$$
\lim_{t \to 0} \Delta_{Th} u_r(t, x) = 0.
$$

The pressure and velocity between $-c_l t$ and $c_r t$ are given in Eq. (4.33).

Figure 4.5 shows the plots of pressure and velocity as $t \to 0$. The initial conditions and parameters are given in Eqs. (4.31) and (4.32). In the figures ν is inversely proportional to t such that the length scale of diffusion $\sqrt{\nu t}$ is fixed for direct comparison. As $t \to 0$, the pressure profile approaches the formulas given above (the curve of the formulas, if plotted, would be indistinguishable
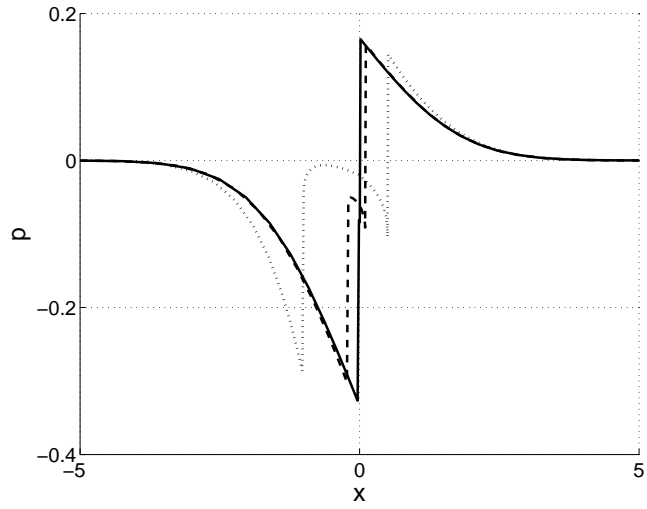
(a)
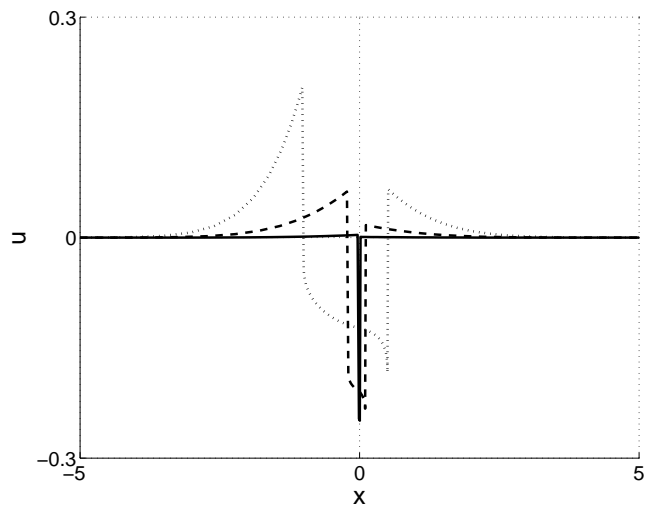
(b)

Figure 4.5: Pressure and velocity fields as $t \to 0$. Initial conditions and parameters except κ_l and κ_r are given in Eqs. (4.31) and (4.32). (a) is $p(x)$, (b) is $u(x)$. In both figures, dotted line is at $t = 1$ for $\kappa_l = 1$ and $\kappa_r = 0.5$, dashed line is at $t = 0.2$ for $\kappa_l = 5$ and $\kappa_r = 2.5$, solid line is at $t = 0.01$ for $\kappa_l = 100$ and $\kappa_r = 50$.

80

from the solid line). And the instantaneous mid state does agrees with Eq. (4.33).

Finally, it should be pointed out that the contact is moving together with the flow. In the linearized model, $i.e.$ up to the first order of the perturbation, the contact is moving with the velocity $u(t, 0)$ obtained above.

4.4 Analytical Solution for Phase Transitions: Temperature Field Decoupled

During phase transitions, the mass flux across the phase boundary depends on the interface temperature and the vapor pressure, so the temperature is coupled to the pressure at the interface even though it is assumed to be decoupled in both phases. Hence the linearized Euler equations are not readily solvable as for the contact, yet with certain approximations we can still obtain the analytical solutions for the special cases.

First, since the heat capacity of the liquid is much larger than that of the vapor, the interfacial temperature is almost the same as the liquid temperature, which is widely assumed in literatures on bubbly flows [12]. With this assumption the equation on the temperature field in the vapor is separated from the pressure field and can be solved analytically. It is a good approximation for short time, but not for longer time. As we will see later for nonlinear equations, the interface temperature gradually approaches the saturation temperature of the vapor pressure. Secondly, since the vapor velocity relative to the phase boundary is much larger than the liquid velocity relative

to the boundary due to their large density ratio, we can approximately take the velocity of the phase boundary, denoted by σ, to be 0 if we only solve the equations for the vapor.

Assume the vapor is on the right side. For clarity the equations for the vapor in the characteristic form are rewritten below. Since the equations are on the vapor side only, the subscripts have been dropped. All thermodynamic parameters are for the vapor.

$$\frac{\partial(p + mu)}{\partial t} + c\frac{\partial(p + mu)}{\partial x} = \Gamma\kappa\frac{\partial^2 T}{\partial x^2},$$

$$\frac{\partial(p - mu)}{\partial t} - c\frac{\partial(p - mu)}{\partial x} = \Gamma\kappa\frac{\partial^2 T}{\partial x^2},$$

$$\rho c_p \frac{\partial T}{\partial t} = \kappa\frac{\partial^2 T}{\partial x^2},$$

with Cauchy data

$$(p, u, T)(t = 0) = (p_0, u_0, T_0).$$

The condition at the phase boundary is

$$T(t, x = 0) = T_l,$$

and from Eq. (4.10),

$$M_{ev} = \rho u_{bd} = \alpha\frac{p_{sat}(T_l) - p_v}{\sqrt{2\pi RT}},$$

82

or equivalently,

$$\mu m u(t,0) = \mu \rho \sqrt{\gamma RT} u(t,0) = p_{sat}(T_l) - p(t,0), \qquad (4.34)$$

where $\mu = \frac{1}{\alpha}\sqrt{\frac{2\pi}{\gamma}}$ is a dimensionless constant.

4.4.1 Analytical Solution

Similarly we can write down the analytical solution.

$$T(t,x) = T_l + (T_0 - T_l)\text{erf}(\frac{x}{\sqrt{4\nu t}}),$$

$$(p - mu)(t,x) = p_0 - mu_0 - \Gamma\kappa(T_0 - T_l)\int_0^t \frac{x - c(\tau - t)}{\nu\tau\sqrt{4\pi\nu\tau}}e^{-\frac{(x-c(\tau-t))^2}{4\nu\tau}}d\tau,$$

$$(p + mu)(t,x)|_{x>ct} = p_0 + mu_0 - \Gamma\kappa(T_0 - T_l)\int_0^t \frac{x + c(\tau - t)}{\nu\tau\sqrt{4\pi\nu\tau}}e^{-\frac{(x+c(\tau-t))^2}{4\nu\tau}}d\tau.$$

$$(p + mu)(t,x)|_{x<ct} = p(t - \frac{x}{c},0) + mu(t - \frac{x}{c},0)$$
$$-\Gamma\kappa(T_0 - T_l)\int_{t-\frac{x}{c}}^t \frac{x + c(\tau - t)}{\nu\tau\sqrt{4\pi\nu\tau}}e^{-\frac{(x+c(\tau-t))^2}{4\nu\tau}}d\tau.$$

And

$$p(t,0) = \frac{\mu p_{ct}(t) + p_{sat}(T_l)}{\mu + 1}$$

$$u(t,0) = \frac{p_{sat}(T_l) - p_{ct}(t)}{(\mu + 1)m}, \qquad (4.35)$$

where

$$p_{ct}(t) = p_0 - mu_0 - \Gamma\kappa(T_0 - T_l)\int_0^t \frac{-c(\tau - t)}{\nu\tau\sqrt{4\pi\nu\tau}}e^{-\frac{(c(\tau-t))^2}{4\nu\tau}}d\tau$$

83

is the pressure on the phase boundary if it were a contact without mass flux. The corresponding u_{ct} would be 0 under the second approximation used for the phase transitions. The solution depends on two more parameters than the contact case, namely, $p_{sat}(T_l)$ and μ.

4.4.2 Example

Again for visualization let us consider the following special case.

$$
\begin{aligned}
(p_0, u_0, T_0) &= (0, 0, 0), \\
(T_l, p_{sat}(T_l)) &= (1, 1), \\
(\Gamma, \kappa, \rho c_p, c, m) &= (1, 1, 1, 1, 1), \\
\mu &= 5.
\end{aligned}
\tag{4.36}
$$

Figure 4.6 shows the temperature, pressure and velocity fields as functions of the space and the time.

4.4.3 Asymptotic Solutions

Similar to the contact case, we can derive the states as $t \to 0$,

$$
\begin{aligned}
\lim_{t \to 0} \Delta_{Th} p(t, 0) &= \frac{\mu \Gamma \rho c_p (T_l - T_0) + p_{sat}(T_l) - (p_0 - m u_0)}{\mu + 1}, \\
\lim_{t \to 0} \Delta_{Th} u(t, 0) &= \frac{p_{sat}(T_l) - (p_0 - m u_0) - \Gamma \rho c_p (T_l - T_0)}{(\mu + 1)m}.
\end{aligned}
$$

In the limit $t \to 0$, the pressure and velocity of the vapor at the interface differ from the values in the contact case as shown in Eq. (4.35). Yet the pressure
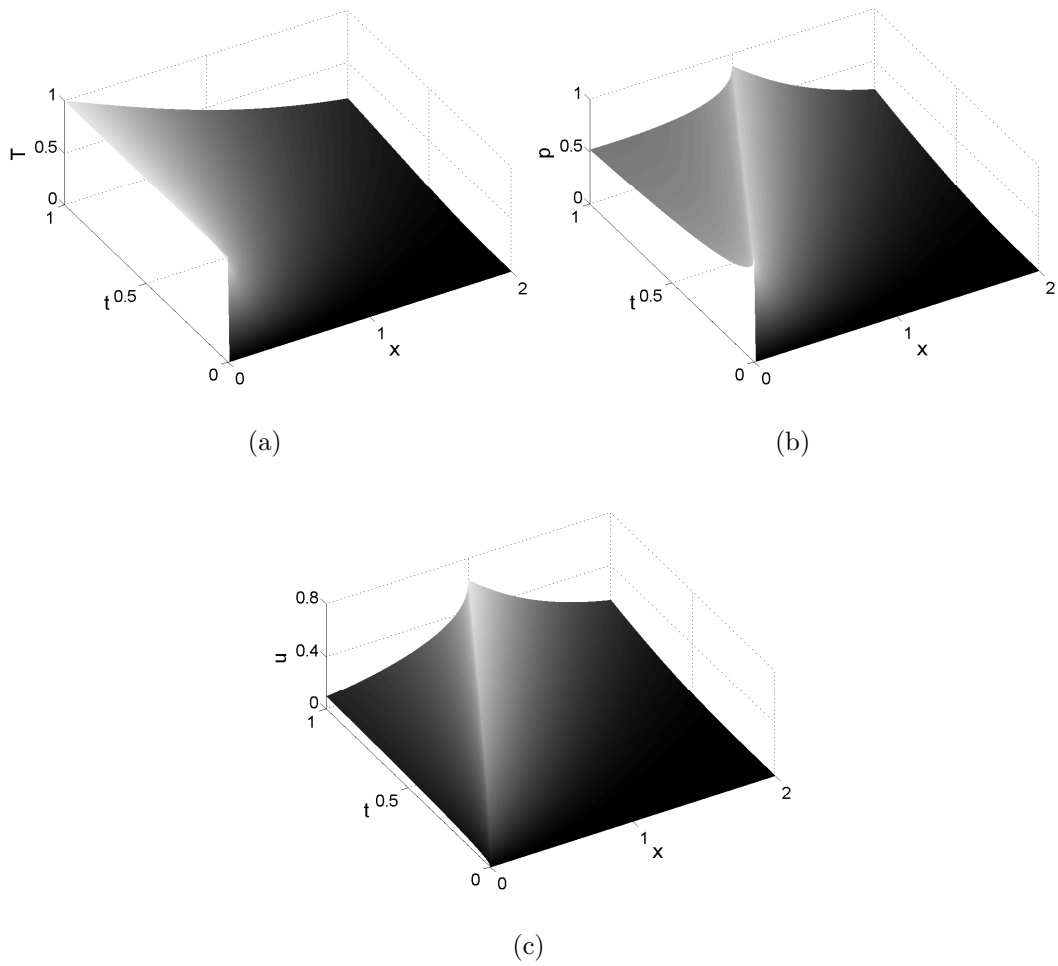
Figure 4.6: Analytical solution with initial condition and parameters given in Eq. (4.36). (a) is $T(t,x)$, (b) is $p(t,x)$, and (c) is $u(t,x)$.

has the same profile of width $\sqrt{\nu t}$ as in the contact case. On the other hand, in the adiabatic limit,

$$
\begin{aligned}
\lim_{\nu \to 0} \lim_{x-ct \to 0+} \Delta_{Th}p &= \Gamma \rho c_p(T_l - T_0), \\
\lim_{\nu \to 0} \lim_{x-ct \to 0+} \Delta_{Th}u &= \frac{1}{m}\Gamma \rho c_p(T_l - T_0), \\
\lim_{\nu \to 0} \lim_{x-ct \to 0-} \Delta_{Th}p &= \frac{\mu \Gamma \rho c_p(T_l - T_0) + p_{sat}(T_l) - (p_0 - mu_0)}{\mu + 1}, \\
\lim_{\nu \to 0} \lim_{x-c_r t \to 0-} \Delta_{Th}u &= \frac{\mu \Gamma \rho c_p(T_l - T_0) + p_{sat}(T_l) - (p_0 - mu_0)}{(\mu + 1)m}.
\end{aligned}
$$

For $x > ct$ the $\Delta_{Th}p$ and $\Delta_{Th}u$ vanish in the adiabatic limit as in the contact case, but for $0 < x < ct$ it is not so. In particular, for $x = 0$,

$$
\begin{aligned}
\lim_{\nu \to 0} \Delta_{Th}p(t, 0) &= \frac{p_{sat}(T_l) - (p_0 - mu_0)}{\mu + 1}, \\
\lim_{\nu \to 0} \Delta_{Th}u(t, 0) &= \frac{p_{sat}(T_l) - (p_0 - mu_0)}{(\mu + 1)m}.
\end{aligned}
$$

Distinct from the contact case, the pressure and velocity on the phase boundary do not reduce to the classical Riemann solution in the adiabatic limit. This result is based on the assumption that the interface temperature is constant. If the assumption is violated, the interface pressure in the adiabatic limit could agree with the classical Riemann solution. All the states listed above in the two limits have been verified for the given example as we did for the contact case.

Now let us discuss the effect of the parameter μ. Since μ is inversely proportional to the evaporation coefficient, $\mu \to \infty$ means no evaporation, thus reduces to case of contact with thermal conduction, as reflected in Eq. (4.35).

On the other hand, if $\mu \to 0$, then the vapor pressure is forced to be at equilibrium with the saturation pressure at the interfacial temperature to induce a finite evaporation/condensation rate. It is a crude model of evaporation, which is used literatures such as [24]. In reality, μ is a finite number and its effect is between these two limit cases.

4.5 Analytical Solutions: Hyperbolic Fields Decoupled

4.5.1 Immiscible Fluids

Next we consider the case that Γ vanishes, again for contact with thermal conduction first. The linearized equations are

$$
\begin{aligned}
\frac{\partial(p_i + m_i u_i)}{\partial t} + c_i \frac{\partial(p_i + m_i u_i)}{\partial x} &= 0, \\
\frac{\partial(p_i - m_i u_i)}{\partial t} - c_i \frac{\partial(p_i - m_i u_i)}{\partial x} &= 0, \\
(\rho c_p)_i \frac{\partial T_i}{\partial t} - (\beta T)_i \frac{\partial p_i}{\partial t} &= \kappa_i \frac{\partial^2 T_i}{\partial x^2},
\end{aligned}
$$

where $i = l$ or r. Initial conditions are

$$
\begin{aligned}
(p_l, u_l, T_l)(t = 0) &= (p_{l0}, u_{l0}, T_{l0}) \\
(p_r, u_r, T_r)(t = 0) &= (p_{r0}, u_{r0}, T_{r0}).
\end{aligned}
$$

Analytical solution

The pressure and velocity fields are exactly the same as the classical Riemann solution. For $x > c_r t$, $(p, u) = (p_{r0}, u_{r0})$. For $x < -c_r t$, $(p, u) = (p_{l0}, u_{l0})$.

And for $-c_l t < x < c_r t$, $(p, u) = (p_m, u_m)$, where

$$
\begin{aligned}
p_m &= \frac{m_l p_{r0} + m_r p_{l0}}{m_l + m_r} + \frac{m_l m_r}{m_l + m_r}(u_{l0} - u_{r0}), \\
u_m &= \frac{m_l u_{l0} + m_r u_{r0}}{m_l + m_r} + \frac{p_{l0} - p_{r0}}{m_l + m_r}.
\end{aligned}
$$

For the temperature field, we could only give the exact solution in the special case that $(\rho c_p \kappa)_l = (\rho c_p \kappa)_r$, because then the continuity of temperature and heat flux at the contact is easily satisfied. Indeed, the temperature field satisfies the equations

$$
\begin{aligned}
(\rho c_p)_l \frac{\partial T_l}{\partial t} - \kappa_l \frac{\partial^2 T_l}{\partial x^2} &= (\beta T)_l (p_m - p_{l0}) \delta\!\left(t + \frac{x}{c_l}\right), \\
(\rho c_p)_r \frac{\partial T_r}{\partial t} - \kappa_r \frac{\partial^2 T_r}{\partial x^2} &= (\beta T)_r (p_m - p_{r0}) \delta\!\left(t - \frac{x}{c_r}\right), \\
T_l(t, 0) &= T_r(t, 0), \\
\kappa_l \frac{\partial T_l}{\partial x}(t, 0) &= \kappa_r \frac{\partial T_r}{\partial x}(t, 0).
\end{aligned}
$$

and the solution is

$$
\begin{aligned}
T_l(t, x) =\ & \frac{T_{l0} + T_{r0}}{2} + \frac{T_{r0} - T_{l0}}{2} \mathrm{erf}\!\left(\frac{x}{\sqrt{4\nu_l t}}\right) \\
& + \frac{(\beta T)_l}{(\rho c_p)_l}(p_m - p_{l0}) c_l \int_0^t \frac{d\tau}{\sqrt{4\pi\nu_l \tau}} \exp\!\left(-\frac{(x - c_l(\tau - t))^2}{4\nu_l \tau}\right) \\
& + \frac{(\beta T)_r}{(\rho c_p)_r}(p_m - p_{r0}) c_r \int_0^t \frac{d\tau}{\sqrt{4\pi\nu_r \tau}} \exp\!\left(-\frac{\left(\frac{\kappa_r}{\kappa_l} x + c_r(\tau - t)\right)^2}{4\nu_r \tau}\right),
\end{aligned}
$$

and

$$
\begin{aligned}
T_r(t, x) &= \frac{T_{l0} + T_{r0}}{2} + \frac{T_{r0} - T_{l0}}{2} \operatorname{erf}(\frac{x}{\sqrt{4\nu_r t}}) \\
&+ \frac{(\beta T)_l}{(\rho c_p)_l}(p_m - p_{l0})c_l \int_0^t \frac{d\tau}{\sqrt{4\pi\nu_l \tau}} \exp(-\frac{(\frac{\kappa_l}{\kappa_r}x - c_l(\tau - t))^2}{4\nu_l \tau}) \\
&+ \frac{(\beta T)_r}{(\rho c_p)_r}(p_m - p_{r0})c_r \int_0^t \frac{d\tau}{\sqrt{4\pi\nu_r \tau}} \exp(-\frac{(x + c_r(\tau - t))^2}{4\nu_r \tau}).
\end{aligned}
$$

Example

Take the following parameters as an example.

$$
\begin{aligned}
(p_{l0}, u_{l0}, T_{l0}) &= (0, 0, 1), \\
(p_{r0}, u_{r0}, T_{r0}) &= (1, 0, 0).
\end{aligned}
$$

and

$$
\begin{aligned}
(\beta T, \kappa, \rho c_p, c, m)_l &= (1, 1, 1, 1, 1), \\
(\beta T, \kappa, \rho c_p, c, m)_r &= (1, 2, \frac{1}{2}, \frac{1}{2}, 1).
\end{aligned}
$$

Figure 4.7(a) shows the plots of pressure and velocity at $t = 1$, which is independent of the temperature field. Figure 4.7(a) shows the temperature field at the same time with different κ's. It is seen that in the adiabatic limit, T becomes a step function. We can prove it using the following lemma.

89
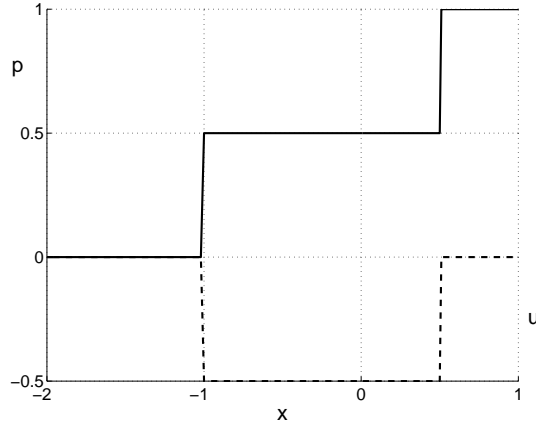
(a)
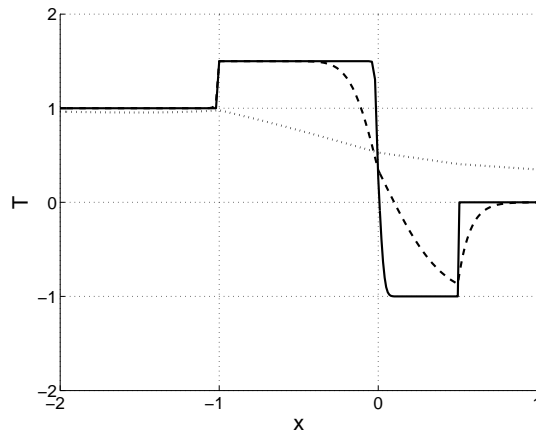
(b)

Figure 4.7: Hyperbolic and parabolic fields with various thermal conductivity. $(p_{l0}, u_{l0}, T_{l0}) = (0, 0, 1)$, $(p_{r0}, u_{r0}, T_{r0}) = (1, 0, 0)$. $(\beta T, \rho c_p, c, m)_l = (1, 1, 1, 1)$, $(\beta T, \rho c_p, c, m)_r = (1, 0.5, 0.5, 1)$. (a) is $p(x)$ and $u(x)$ at $t = 1$, independent of κ's. Solid line is p, dashes line is u. (b) is $T(x)$ at $t = 1$. Dotted line is for $\kappa_l = 1$ and $\kappa_r = 2$, dashed line is for for $\kappa_l = 0.01$ and $\kappa_r = 0.02$, solid line is for for $\kappa_l = 0.0001$ and $\kappa_r = 0.0002$.

Lemma 4.5.1 *For $0 < a < 1$,*

$$\lim_{N \to \infty} \frac{1}{\sqrt{\pi}} \int_0^N dz \exp(-\frac{1}{4}(z - a\frac{N^2}{z})^2) = 1,$$

while for $a < 0$ and $a > 1$,

$$\lim_{N \to \infty} \frac{1}{\sqrt{\pi}} \int_0^N dz \exp(-\frac{1}{4}(z - a\frac{N^2}{z})^2) = 0.$$

Proof: For $0 < a < 1$, let $a = k^2$ with $0 < k < 1$,

$$\lim_{N \to \infty} \frac{1}{\sqrt{\pi}} \int_0^N dz \exp(-\frac{1}{4}(z - \frac{(kN)^2}{z})^2)$$

$$= \lim_{N \to \infty} \frac{1}{\sqrt{\pi}} \int_{-kN}^{(1-k)N} dy \exp(-y^2(\frac{kN + \frac{y}{2}}{kN + y})^2)$$

$$= \lim_{N \to \infty} \frac{1}{\sqrt{\pi}} \int_{-\sqrt{kN}}^{\sqrt{kN}} dy \exp(-y^2(\frac{kN + \frac{y}{2}}{kN + y})^2)$$

$$+ \lim_{N \to \infty} \frac{1}{\sqrt{\pi}} \int_{-kN}^{-\sqrt{kN}} dy \exp(-y^2(\frac{kN + \frac{y}{2}}{kN + y})^2)$$

$$+ \lim_{N \to \infty} \frac{1}{\sqrt{\pi}} \int_{\sqrt{kN}}^{(1-k)N} dy \exp(-y^2(\frac{kN + \frac{y}{2}}{kN + y})^2).$$

The first integral equals

$$\frac{1}{\sqrt{\pi}} \int_{-\infty}^{\infty} dy e^{-y^2} = 1,$$

and the other two vanish.

91

For a < 0,

$$\lim_{N\to\infty} \frac{1}{\sqrt{\pi}} \int_0^N dz \exp(-\frac{1}{4}(z - a\frac{N^2}{z})^2)$$

$$= \lim_{N\to\infty} \frac{1}{\sqrt{\pi}} e^{\frac{a}{2}N^2} \int_0^N dz \exp(-\frac{1}{4}(z^2 + (a\frac{N^2}{z})^2))$$

$$\leq \lim_{N\to\infty} \frac{1}{\sqrt{\pi}} e^{\frac{a}{2}N^2} \int_0^N dz e^{-\frac{z^2}{4}}$$

$$= 0.$$

For a > 1,

$$\lim_{N\to\infty} \frac{1}{\sqrt{\pi}} \int_0^N dz \exp(-\frac{1}{4}(z - a\frac{N^2}{z})^2)$$

$$\leq \lim_{N\to\infty} \frac{1}{\sqrt{\pi}} \int_0^N dz \exp(-\frac{1}{4}((a - 1)N)^2)$$

$$= \lim_{N\to\infty} \frac{N}{\sqrt{\pi}} \exp(-\frac{1}{4}((a - 1)N)^2)$$

$$= 0.$$

Limit solutions

Using the lemma above with $N^2 = \frac{c^2 t}{\nu}$ and $a = 1 - \frac{|x|}{ct}$, it is straightforward to show that in the adiabatic limit, the temperature field is

$$T(t, x < -c_l t) = T_{l0},$$

$$T(t, -c_l t < x < 0) = T_{l0} + \frac{(\beta T)_l}{(\rho c_p)_l}(p_m - p_{l0}),$$

$$T(t, 0 < x < c_r t) = T_{r0} + \frac{(\beta T)_r}{(\rho c_p)_r}(p_m - p_{r0}),$$

$$T(t, c_r t < x) = T_{r0}.$$

Compared with the equation on temperature, the formulas above indicate that the entropy in each phase doesn't change across the wavefront in the adiabatic limit, which agree with the classical Riemann solution (for linearized EOS the entropy jump across the shock front is 0 because the sound speed is a constant). A refined version of Lemma 4.5.1 would reveal that the transition layers in terms of a have width of order $1/N$ and $1/N^2$ at $a = 1$ and $a = 0$, respectively. For example, it can be proven that for $k \to 1$ while $N(1 - k)$ is fixed,

$$\lim_{N \to \infty} \frac{1}{\sqrt{\pi}} \int_0^N dz \exp(-\frac{1}{4}(z - a\frac{N^2}{z})^2) = \frac{1}{2}(1 + \text{erf}(N(1 - k))).$$

Transformed to the hyperbolic-parabolic system, it means the width of the left and right propagating temperature jumps are of order ν/c while the jump width at contact is of order $\sqrt{\nu t}$. This result is the same as the case where βT is neglected. It is also observed that in the adiabatic limit, the contribution to the temperature field around the contact from the pressure field has the same profile as that from the thermal diffusion, namely

$$T = T_M + \Delta T \text{erf}(\frac{x}{\sqrt{4\nu t}}), \tag{4.37}$$

where T_M and ΔT are the contact temperature and temperature jump on either side.

We can also check the isothermal limit, *i.e.* $t \to 0$. Figure 4.8 shows the temperature field in the decreasing times with νt fixed. It is easy to see that
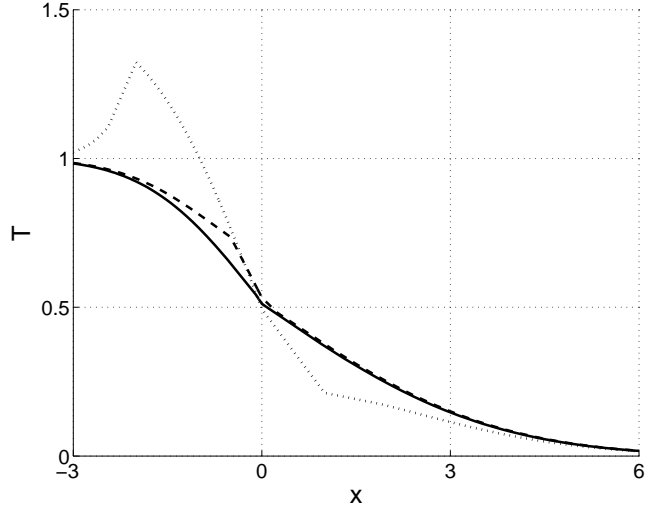
Figure 4.8: Temperature field as $t \to 0$. Parameters and initial conditions are the same as in Figure 4.7. Dotted line is at $t = 2$ for $\kappa_l = 0.5$ and $\kappa_r = 1$, dashed line is at $t = 0.5$ for $\kappa_l = 2$ and $\kappa_r = 4$, solid line is at $t = 0.1$ for $\kappa_l = 10$ and $\kappa_r = 20$.

the limit temperature field is

$$
\begin{aligned}
\lim_{t \to 0} T_l(t, x) &= \frac{T_{l0} + T_{r0}}{2} + \frac{T_{r0} - T_{l0}}{2} \mathrm{erf}(\frac{x}{\sqrt{4\nu_l t}}), \\
\lim_{t \to 0} T_r(t, x) &= \frac{T_{l0} + T_{r0}}{2} + \frac{T_{r0} - T_{l0}}{2} \mathrm{erf}(\frac{x}{\sqrt{4\nu_r t}}).
\end{aligned}
$$

In other words, the hyperbolic fields does not affect the temperature field in the isothermal limit.

4.5.2 Phase Transitions

As in Section 4.4 we need certain approximation to decouple the temperature field from the hyperbolic fields in the boundary condition on the phase

boundary. The equation is in the vapor side only, and the approximation is $T(t, 0) = T_l$ and $\sigma = 0$. For clarity, we rewrite the equations here.

$$\frac{\partial(p + mu)}{\partial t} + c\frac{\partial(p + mu)}{\partial x} = 0,$$

$$\frac{\partial(p - mu)}{\partial t} - c\frac{\partial(p - mu)}{\partial x} = 0,$$

$$\rho c_p\frac{\partial T}{\partial t} - \beta T\frac{\partial p}{\partial t} = \kappa\frac{\partial^2 T}{\partial x^2},$$

with Cauchy data and boundary conditions

$$(p, u, T)(t = 0) = (p_0, u_0, T_0),$$

$$T(t, x = 0) = T_l,$$

$$\mu mu(t, 0) = p_{sat}(T_l) - p(t, 0),$$

where $\mu = \frac{1}{\alpha}\sqrt{\frac{2\pi}{\gamma}}$ is a dimensionless constant.

Analytical Solution

The hyperbolic fields are piecewise constant,

$$p(t, x > ct) = p_0,$$

$$u(t, x > ct) = u_0,$$

$$p(t, x < ct) = p_m = \frac{\mu(p_0 - mu_0) + p_{sat}(T_l)}{\mu + 1},$$

$$u(t, x < ct) = u_m = \frac{p_{sat}(T_l) - (p_0 - mu_0)}{(\mu + 1)m},$$

which agree with Eq. (4.35) derived in the $\beta = 0$ case. The temperature is

$$
\begin{aligned}
T(t,x) \;=\;& T_l + (T_0 - T_l)\mathrm{erf}(\frac{x}{\sqrt{4\nu t}}) \\
&+ \frac{\beta T}{\rho c_p}(p_m - p_0)c \int_0^t \frac{d\tau}{\sqrt{4\pi\nu\tau}} \exp(-\frac{(x + c(\tau - t))^2}{4\nu\tau}) \\
&- \frac{\beta T}{\rho c_p}(p_m - p_0)c \int_0^t \frac{d\tau}{\sqrt{4\pi\nu\tau}} \exp(-\frac{(x - c(\tau - t))^2}{4\nu\tau}).
\end{aligned}
$$

Limit solutions

The limit solutions are nothing but special cases of the previous section on the contact. In the isothermal limit ($t \to 0$),

$$
\lim_{t\to 0} T(t,x) = T_l + (T_0 - T_l)\mathrm{erf}(\frac{x}{\sqrt{4\nu t}}).
$$

In the adiabatic limit,

$$
\begin{aligned}
T(t, x < ct) \;&=\; T_0 + \frac{\beta T}{\rho c_p}(p_m - p_0), \\
T(t, x > ct) \;&=\; T_0.
\end{aligned}
$$

As for the contact case, the formulas indicate that the entropy is continuous across the wavefront. Notice that the parameters μ and $p_{sat}(T_l)$ play no role in the T field in both limits, although they do affect the pressure and velocity. Once again, the deviation of the pressure and velocity distributions from the Riemann solution in the adiabatic limit comes from the assumption that T_l is a constant.

4.6 Full Nonlinear Equations

Having discussed the two exactly solvable cases of linearized equations, we change gear to the nonlinear equations. The followings are the observations from the linearized equations.

- In the isothermal limit for immiscible fluids, the thermal effect dominates. The hyperbolic layer (ct) is much narrower than the thermal layer ($\sqrt{\nu t}$). The pressure has accumulated from the thermal wave an instantaneous change at each side of the hyperbolic layer, and the mid state is determined by these modified pressures. The velocity field has not changed. Both the temperature and the pressure fields in the thermal layer have width $\sqrt{\nu t}$.

- In the adiabatic limit for immiscible fluids, the solution to the problem with Riemann data converges to the classical Riemann solution in general. The temperature field has jump width of order $\sqrt{\nu t}$ at the material interface and jump width of order ν/c at the propagating shock fronts or rarefactions. Pressure and velocity fields have spikes at the wave fronts with width of order ν/c.

- The behavior of the vapor in phase transitions in the isothermal limit is similar to that for the immiscible fluids but the interface pressure and velocity are different. At the early stage of phase transitions, the interface temperature is close to the liquid temperature, but later it changes slowly toward the saturated temperature at the vapor pressure.

As we will see, the solution to the problem with Riemann data also converges to the classical Riemann solution.

4.6.1   Local Riemann Problem

Next we will give the procedure to solve the full nonlinear local Riemann problem, being full meaning neither βT nor Γ vanishes. For clearness we rewrite the equations here.

$$
\begin{aligned}
\frac{\mathrm{d}p}{\mathrm{d}\lambda_{\pm}} \pm \rho c \frac{\mathrm{d}u}{\mathrm{d}\lambda_{\pm}} &= \Gamma\kappa\frac{\partial^2 T}{\partial x^2}, \\
\rho c_p \frac{\mathrm{d}T}{\mathrm{d}\lambda_0} - \beta T \frac{\mathrm{d}p}{\mathrm{d}\lambda_0} &= \kappa\frac{\partial^2 T}{\partial x^2}.
\end{aligned}
\tag{4.38}
$$

For each phase there is different set of initial conditions and EOS. Subscript will be added when necessary. Continuity of temperature at the interface requires an interfacial temperature in the limit $t \to 0$, denoted by T_m. The procedure is to find the T_m first, then use it to determine the mid state. The derivation in this section is more heuristic than rigorous compared to the previous sections.

Temperature field

In the limit of $t \to 0$, the system is predominantly parabolic, so all the first order spatial derivatives can be neglected. The conservation of mass and

momentum gives

$$\frac{\partial \rho}{\partial t} = 0, \qquad (4.39)$$

$$\frac{\partial (\rho u)}{\partial t} = 0, \qquad (4.40)$$

which indicates the density and velocity are unchanged. The energy conservation law gives

$$\rho c_p \frac{\partial T}{\partial t} = (1 + \Gamma \beta T) \kappa \frac{\partial^2 T}{\partial x^2}.$$

Recalling the thermodynamic identity

$$\frac{c_p}{c_v} = \frac{K_T}{K_S} = \frac{c^2}{c_T^2} = 1 + \Gamma \beta T,$$

where c_v is the specific heat with constant volume, c_T is the "isothermal sound speed", K_T and K_S are the isothermal and isentropic compressibility. The temperature equation can be simplified to

$$\rho c_v \frac{\partial T}{\partial t} = \kappa \frac{\partial^2 T}{\partial x^2}. \qquad (4.41)$$

With Eq. (4.39) in mind, the coefficients in Eq. (4.41) are evaluated along the isovolumes and thus functions of the only variable T. Therefore it is a nonlinear equation of T. At the interface T is continuous, and the heat flux satisfies

$$\kappa_r \frac{\partial T_r}{\partial x} - \kappa_l \frac{\partial T_l}{\partial x} = 0 \qquad (4.42)$$

99

for contact, and

$$\kappa_r \frac{\partial T_r}{\partial x} - \kappa_l \frac{\partial T_l}{\partial x} = M_{ev} L \qquad (4.43)$$

for phase boundary. In case $T_{l0} = T_{r0}$, we would have $T_m = T_{l0} = T_{r0}$, otherwise since the temperature gradient is infinite at the interface as $t \to 0$, the left side of the Eqs. (4.42) and (4.43) are actually $\infty - \infty$, therefore the limit temperature field with the boundary condition Eq. (4.43) would have the same T_m as that with boundary condition Eq. (4.42). In other words, for the purpose of finding T_m in the limit $t \to 0$, we can always use Eq. (4.42) instead of Eq. (4.43).

If the coefficients in Eq. (4.41) do not vary much, it suffices to solve the linearized version. The solution is

$$
\begin{aligned}
T_m &= \frac{T_{l0}\sqrt{(\rho c_v \kappa)_l} + T_{r0}\sqrt{(\rho c_v \kappa)_r}}{\sqrt{(\rho c_v \kappa)_l} + \sqrt{(\rho c_v \kappa)_r}}, \qquad (4.44) \\
T_l(t,x) &= T_m + (T_m - T_{l0})\mathrm{erf}(\frac{x}{\sqrt{4\nu_l^* t}}), \\
T_r(t,x) &= T_m + (T_{r0} - T_m)\mathrm{erf}(\frac{x}{\sqrt{4\nu_r^* t}}),
\end{aligned}
$$

where $\nu^* = \sqrt{\kappa/(\rho c_v)}$.

Pressure and velocity fields

From the temperature field and Eqs. (4.40) and (4.39), the pressure and velocity fields outside the hyperbolic layer ($x < -c_l t$ and $x > c_r t$) in the limit

100

$t \to 0$ are

$$p_l(t, x) = P_l(T_l(t, x), \rho_{l0}),$$

$$p_r(t, x) = P_r(T_r(t, x), \rho_{l0}),$$

$$u_l(t, x) = u_{l0},$$

$$u_r(t, x) = u_{r0},$$

where P_l and P_r are thermodynamic functions depending on the EOS on each side. Now let us find the mid state in the hyperbolic layer $-c_l t < x < c_r t$. Since hyperbolic system propagates at finite speed, the local initial value $p_l(0+, 0-)$, $u_l(0+, 0-)$, $p_r(0+, 0+)$ and $u_r(0+, 0+)$ solely determine the instantaneous mid state. Since the thermal layer is much wider than the hyperbolic layer, the temperature in the hyperbolic layer is T_m. Therefore the last step is to solve a Riemann problem with the modification from isentropic to isothermal. The equations are

$$\frac{\partial \rho_i}{\partial t} + \frac{\partial \rho_i u_i}{\partial x} = 0,$$

$$\frac{\partial \rho_i u_i}{\partial t} + \frac{\partial \rho_i u_i^2 + p_i}{\partial x} = 0,$$

$$T_i = T_m,$$

where subscript i is l or r. The initial conditions are

$$(\rho, p, u)_l(t = 0) = (\rho_{l0}, P_l(T_m, \rho_{l0}), u_{l0}),$$

$$(\rho, p, u)_r(t = 0) = (\rho_{r0}, P_r(T_m, \rho_{r0}), u_{r0}).$$

T_m is from the solution to Eq. (4.41) with boundary condition Eq. (4.42). Approximate value of T_m is given above.

The other conditions at the interface are the Rankine-Hugoniot conditions for contact

$$\Delta p = 0,$$
$$\Delta u = 0,$$

or Rankine-Hugoniot conditions plus the one from kinetic theory for phase boundary

$$\Delta p = -M\Delta u, \tag{4.45}$$
$$\Delta u = M\Delta V, \tag{4.46}$$
$$M_{ev} = \frac{\alpha}{\sqrt{2\pi RT_m}}(p_{sat}(T_m) - p_v). \tag{4.47}$$

Here Δ stands for the difference between left and right side.

Now that the equations are purely hyperbolic, we can find its characteristics and corresponding "Riemann" invariants. It it not difficult to show that the 2 by 2 systems has two characteristics, namely, $\lambda_{\pm} = u \pm c_T$, where c_T is the isothermal sound speed. The corresponding invariants are $du \pm \frac{dp}{\rho c_T}$. The solution has self-similarity as in the Riemann problem, so we can construct the mid state analogously. In Figure 4.9, the curve for left shock wave and rarefaction passes the (p_{l0}^*, u_{l0}) point in the $p-u$ plane, and the curve for right shock wave and rarefaction passes the (p_{r0}^*, u_{r0}) point. Here p_{l0}^* and p_{r0}^* are
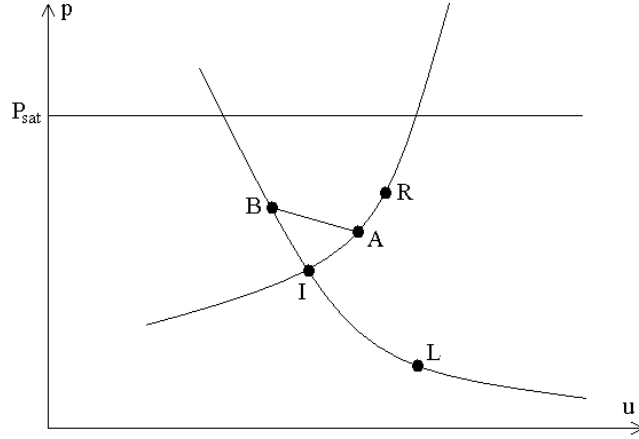
Figure 4.9: Construction of the mid state and the wave structure for the isothermal Riemann problem. The curves passing point L is the left shock curve (upper part) and rarefaction (lower part). The curves passing point R is the right shock curve (upper part) and rarefaction (lower part). The intersection is the instantaneous mid state for contact with thermal conduction.

the initial pressures for the current isothermal Riemann problem. Along the

left(right) rarefaction, $dT = 0$ and

$$du \pm \frac{dp}{\rho c_T} = 0.$$

Along the left(right) shock curve, $u_r < u_l$ and

$$\Delta V \Delta p = -(\Delta u)^2,$$

$$\Delta T = 0.$$

For the contact, all we need is to find the intersection of the two curves. The mere existence of c_T guarantee the monotonicity of the rarefaction and

shock curves and thus the uniqueness of the intersection. The mid state is then determined and the local wave has the same structure as in the Riemann solution, namely, a left shock wave or rarefaction, a right shock wave or rarefaction, and a contact in between.

Phase transition

For phase transitions, in order to find the left and right mid states we need to go through the following procedure. For simplicity the vapor is assumed to be on the right side, the opposite case can be treated similarly.

1. Find the intersection, which is shown as point I in Figure 4.9, of the curves for left and right waves in $p - u$ plane, just as for the contact. Denote the mid state by (p_m^*, u_m^*). If $p_{sat}(T_m) = p_m^*$, then from Eq. (4.47) $M_{ev} = 0$ and it reduces to the contact without mass flux. If $p_{sat}(T_m) \neq p_m^*$, then go to step 2.

2. We will treat the case $p_{sat}(T_m) > p_m^*$, the opposite case can be handled similarly. For simplicity we will write p_s instead of $p_{sat}(T_m)$ in this paragraph. If $p_v = p_m^*$, then the vapor is unsaturated, and Eq. (4.47) also indicates that $M_{ev} > 0$, so the vapor pressure will increases from the evaporation. Therefore the actual p_v should be between p_m^* and p_s. We are going to show that there is a unique p_v and associated mid state satisfying Eqs. (4.45)–(4.47).

   For each p_v between p_m^* and p_s we can determine the $M = M_{ev}$ by Eq. (4.47). The p_v also determines u_v since (p_v, u_v), which is point A in

Figure 4.9, in one the curve for right wave. Using Eq. (4.45) we can draw a line with slope $-M$ passing point A. The line would intersect the curve for left wave so long as M is smaller than the absolute slope of the curve. Since the latter is approximately $\rho_l c_l$, it requires

$$\frac{\alpha}{\sqrt{2\pi R T_m}}(p_{sat}(T_m) - p_v) < \rho_l c_l,$$

or equivalently,

$$\alpha\sqrt{\frac{\gamma}{2\pi}}(p_{sat}(T_m) - p_v) < \rho_l c_l c_v,$$

where γ is the polytropic index of the vapor and c_v is vapor sound speed at temperature T_m. In practice p_s is of the same order as p_v, and the inequality above is always satisfied. For example, for water not too far from saturation in temperature from 20^oC to 100^oC, the left side of the inequality is no more than 1 atmosphere, while the right side is more than 5000 atmosphere. The intersection of the line with the curve is denoted by point B in Figure 4.9. Now that we know the temporary mid state on both sides, we can check the last jump condition Eq. (4.46). Let

$$f(p_v) = \Delta u - M\Delta V.$$

All quantities on the right side are continuous functions of p_v. We need to find the zero of f for $p_m^* \le p_v \le p_s$. Next we will prove the existence of such a zero point. First, at $p_v = p_m^*$, $M > 0$ by Eq. (4.47) and point

A coincides with point B so $\Delta u = 0$, therefore

$$f(p_m^*) = -M(V_v - V_l) < 0,$$

where we have set the Δ to be right side minus left side. Second, at $p_v = p_s$, $M = 0$ by Eq. (4.47) and point B is to the left of point A, so

$$f(p_s) = \Delta u = u_A - u_B > 0.$$

From fundamental calculus we know f must have a zero between p_m^* and p_s. It is easy to verify that f is a monotonely increasing function of p_v, therefore the zero of f is unique. Similar conclusion can be drawn for the case that $p_s < p_m^*$. In that case, $M_{ev} < 0$ and $p_s < p_v < p_m^*$. Numerically the value of p_v can be found by iteration. Upon linearization, the M_{ev} so obtained agrees with the results in Section 4.4.

4.6.2   Travelling Wave Solutions

We sought the solution in the adiabatic limit using the method of travelling wave solutions. The travelling wave solution is a useful tool in the investigation of nonlinear properties of hyperbolic systems with terms involving higher order spatial derivatives such as viscosity and thermal conduction [14, 33]. In this section we studied the travelling wave solutions to the Euler equations with heat conduction and phase transitions. The equations are Eqs. (4.1)–(4.3) and the interface conditions are Eqs. (4.4)–(4.10). We first found

106

the travelling wave solutions with the discontinuity at the phase boundary, then the solutions with the discontinuity in a single phase. Discontinuities still exist as a contrast to usual travelling wave solutions because here only the temperature is continuous everywhere while the pressure and velocity are still allowed to be discontinuous.

Travelling waves across the phase boundary

In the reference frame of the phase boundary, the travelling wave solution is a steady state. So we only need to find all the steady states. From Eqs. (4.1)–(4.3), it is easy to write down the solution,

$$\rho u \;=\; M,$$

$$\rho u^2 + p \;=\; Mu + p = B,$$

$$(\rho E + p)u - \kappa T_x \;=\; M(H + \frac{u^2}{2}) - \kappa T_x = C,$$

where M, B and C are three constants. The Rankine-Hugoniot conditions dictates that M, B and C are equal for both left and right states. Since the interface is at rest, M coincides with the usual notation for mass flux. Using the remaining two boundary conditions, namely, the continuity of temperature and Eq. (4.10), the solution is uniquely determined by the pressure, temperature and temperature gradient of the vapor at the interface. The procedure is as following. First the M is determined by Eq. (4.10), then the liquid state on the interface is determined by the continuity of T and the Rankine-Hugoniot

107

condition

$$\Delta p = -M^2 \Delta V.$$

The liquid state is illustrated as the intersection of two curves in Figure 4.10. The velocities of both phases at the interface are $u_l = MV_l$ and $u_v = MV_v$. The temperature gradient of the vapor at the interface determined the constant C. The state away from the interface on each side is determined by the EOS and the following equations,

$$
\begin{aligned}
kT_x &= M(H + \frac{u^2}{2}) - C = M(H + \frac{M^2}{2}V^2) - C, \qquad (4.48) \\
p - p_s &= -M^2(V - V_s),
\end{aligned}
$$

where p_s and V_s are from the state on the interface. Given the EOS, the ODE can be integrated to find the thermodynamic state for all x, while the velocity is again determined by $u = MV$.

With the EOS and the second equation above in mind, the term $H + \frac{M^2}{2}V^2$ in Eq. (4.48) can be regarded as a function of T. In general the function is complicated, but we will show for slow phase transitions the term can be approximated by $c_p T$ up to a constant. Indeed, denote the mach number u_s/c
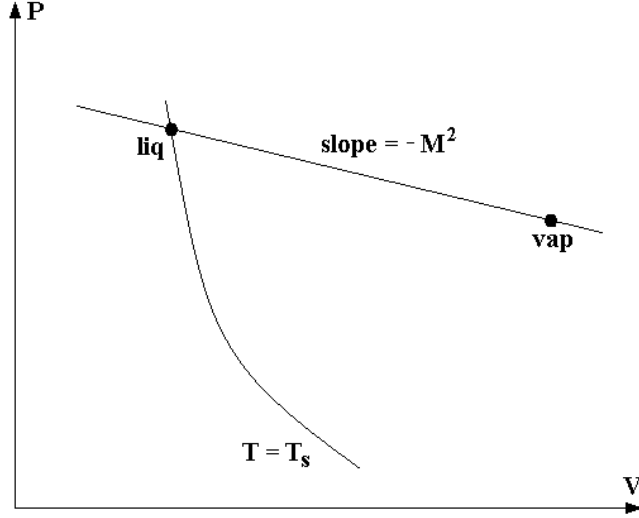
Figure 4.10: Schematic of interface states for travelling wave solutions of the Euler equations with phase transitions. The states stay on the line connecting the liquid and vapor states at the interface.

by n, the differential of $H + \frac{M^2}{2}V^2$ is

$$d(H + \frac{M^2}{2}V^2)$$

$$= c_p dT + V(1 - \beta T)dp + M^2 V\, dV$$

$$= c_p dT + \beta T M^2 V\, dV$$

$$= c_p dT(1 + n^2\Gamma\frac{T}{V}\frac{dV}{dT})$$

$$= c_p dT(1 + n^2\Gamma\beta T(1 - n^2\gamma)),$$

where Γ is the Gruneisen coefficient, γ is the ratio of specific heat, and β is the thermal expansion coefficient. For both POLY and SPOLY EOS's, $\Gamma = \gamma - 1$. $\beta T = 1$ for ideal gas, while it is much smaller than 1 for liquid. Since γ and Γ are of order 1, it is clear $H + \frac{M^2}{2}V^2 \doteq c_p T$ up to a constant for small mach

109

number.

With the approximation for slow phase transitions, Eq. (4.48) involves temperature only, so it can be integrated to give

$$T(x) = T_s + \frac{(\kappa T_x)_s}{c_p M}(\exp(\frac{M c_p x}{\kappa}) - 1).$$

The equation above is unbounded for $x \to \infty$ if $M > 0$ or for $x \to -\infty$ if $M < 0$, unless $(\kappa T_x)_s = 0$. Therefore, if we require the temperature to be bounded in the entire space, the "product" of phase transitions (vapor in evaporation, liquid in condensation) must be constant state. On the other hand, if the problem is on a finite domain with certain boundary conditions to guarantee a steady state solution, both phases can be nonuniform.

To understand the solution, let us take the example of evaporation ($M > 0$) with constant vapor state. The latent heat for the phase transition is totally provided by the liquid, *i.e.*

$$-(\kappa T_x)_s = ML.$$

So the liquid temperature field is

$$T(x) = T_s + \frac{L}{c_p}(1 - \exp(\frac{M c_p x}{\kappa})). \tag{4.49}$$

The temperature of the liquid at $-\infty$ is $T_L = T_s + \frac{L}{c_p}$. The interpretation is clear – the heat released by the liquid whose temperature dropped from T_L to T_s is $c_p(T_L - T_s) = L$, which is exact the latent heat needed for the phase

110

transition. Nevertheless, this solution is *not* physical. The reason is that during evaporation, the liquid state on the interface is metastable, and the liquid state in the above solution has higher temperature but lower pressure than interface state, which deviates further from the phase coexistence curve and is metastable or unstable more strongly, so the solution cannot exist physically. In other word, the physical travelling wave solution can only exist on finite domain and the "product" phase cannot be uniform. On the contrary, it is the "product" phase that provides the latent heat in evaporation and absorbs the heat emitted in condensation.

Travelling waves in a single phase

In the reference frame of the pressure jump or equivalently the shock front, the travelling wave solution is a steady state. The equations are still

$$
\begin{aligned}
\rho u &= M, \\
\rho u^2 + p &= Mu + p = B, \\
(\rho E + p)u - \kappa T_x &= M(H + \frac{u^2}{2}) - \kappa T_x = C.
\end{aligned}
\tag{4.50}
$$

But now the EOS on both sides of the shock front are the same, and the mach numbers are bigger than 1 on one side and smaller than 1 on the other. Since the mach numbers behind the shock is less than 1, the differential of the term $H + \frac{M^2}{2}V^2$ has the same sign as $c_p dT$. Because the temperature is required to be bounded in the entire space for a shock wave to exist in the adiabatic limit, similar to the travelling wave solutions across the phase boundary, we
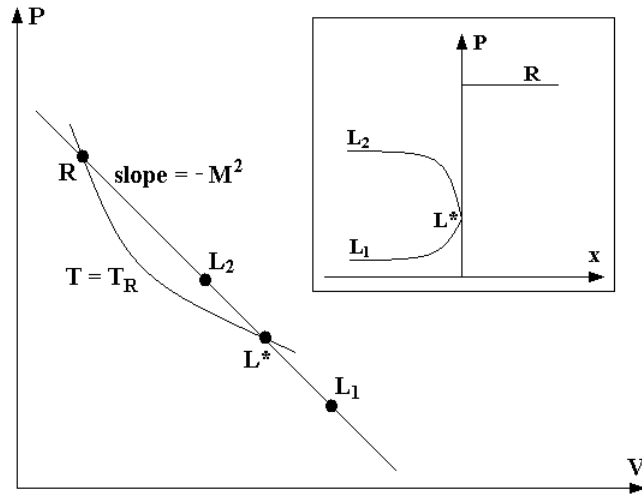
Figure 4.11: Schematic of the travelling wave solution to the Euler equations with heat conduction for the left shock wave.

conclude that the state behind the shock must be constant.

Let's take the left shock $(M > 0)$ to illustrate the travelling wave solution. The schematic is shown in Figure 4.11. The right side is behind the shock so it has to be a constant state. The temperature at the left side of the interface equals T_R, so the left state at the shock front could be either R or L^* in the figure. However, the left front state must be L^* unless $L = R$ because otherwise $T_x \equiv 0$ by Eq. (4.50) which implies $L = R$. The states to the left of the front stay on the segment connecting L and L^* in the $p - V$ diagram and gradually changes from one end to the other. If $T_R > T_L$ as for the point L_1, then $p_{L^*} > p_L$. If $T_R < T_L$ as for the point L_2, then $p_{L^*} < p_L$ and the pressure profile appears as a spike. In both cases, the decay length of the left pressure profile is of order ν/c.

4.6.3 Adiabatic Limit

In the adiabatic limit, the hyperbolic layer is much wider than the thermal layers and the solution to the problem with Riemann data essentially has the same structure as the classical Riemann solution. First we consider the left and right propagating waves, which are either rarefactions or shock waves. For rarefactions, the perturbation from the thermal effect approaches zero in the adiabatic limit because the width of the rarefactions is proportional to t and much wider than the thermal layers. However for shock waves the perturbation from the thermal effect does not approach zero everywhere. In fact, from the travelling wave solutions in a single phase, we see that the pressure wave deviate from the classical Riemann solution in a region of width about ν/c and the amount of deviation is nonzero in the adiabatic limit. Next we turn to the central wave which depends on the interfacial property.

Contact

First we consider the simpler case without phase transition. In the purely hyperbolic system, the temperature is discontinuous at the contact and the solution around the contact can be considered as the simplest travelling wave that has no mass flux. With thermal conduction, however, the temperature profile at contact is smoothed out to the width of order $\sqrt{\nu t}$, so that the solution is *not* a travelling wave solution. The interfacial temperature is determined by temperature on its two sides and the continuity condition of heat flux. The following is the detail.

The left and right mid states have the same pressure and velocity but

different temperature, denoted by T_{ML} and T_{MR}. Since the pressure around the contact is not changing as $t \to \infty$, the equations for the temperature are

$$
\begin{aligned}
(\rho c_p)_l\left(\frac{\partial T_l}{\partial t} + u_l\frac{\partial T_l}{\partial x}\right) &= \kappa_l\frac{\partial^2 T_l}{\partial x^2}, \\
(\rho c_p)_r\left(\frac{\partial T_r}{\partial t} + u_r\frac{\partial T_r}{\partial x}\right) &= \kappa_r\frac{\partial^2 T_r}{\partial x^2}.
\end{aligned}
$$

And at contact

$$
\begin{aligned}
T_l &= T_r, \\
\kappa_l\frac{\partial T_l}{\partial x} &= \kappa_r\frac{\partial T_r}{\partial x}.
\end{aligned}
$$

Also, the temperature at the far left end and the far right end are T_{ML} and T_{MR} respectively. Since the contact is moving together with the fluid, it is straightforward to show that the temperature at the contact T_{ct} as $t \to \infty$ is

$$
T_{ct} = \frac{T_{ML}\sqrt{(\rho c_p \kappa)_l} + T_{MR}\sqrt{(\rho c_p \kappa)_r}}{\sqrt{(\rho c_p \kappa)_l} + \sqrt{(\rho c_p \kappa)_r}}.
$$

Phase transition

The interfacial temperature is more important for phase transitions because the transition rate is related to the saturation pressure at the interfacial temperature. First we exclude the possibility in most cases that the solution converges to a steady state solution across the phase boundary with nonzero transition rate. Too see that we assume on the contrary that the solution does converge to a steady state solution with nonzero mass flux, then as we

114

have pointed out, the "product" phase must be a constant state, and far from the phase boundary the "source" phase has temperature L/c_p above/below the interface temperature for evaporation/condensation, which is unphysical – *e.g.* for the phase transition in room temperature between the water and the water vapor, it requires the source phase to be either the water hotter than 500^oC or the vapor colder than -1000^oC.

Then we demonstrate that the transition rate decreases to zero as $t \to \infty$ and thus the solution is *not* a travelling wave solution either. The limit temperature at the phase boundary T_{ph} is determined by

$$p_{sat}(T_{ph}) = p_v = p_M,$$

where p_M is the pressure on the contact if there were no phase transition. Again we assume the vapor is on the right side. Denote the interfacial temperature by T_s (whose limit as $t \to \infty$ is T_{ph}). The equations for temperature are the same as for the contact, but the boundary conditions change to

$$
\begin{aligned}
T_l &= T_r, \\
\kappa_r \frac{\partial T_r}{\partial x} - \kappa_l \frac{\partial T_l}{\partial x} &= M_{ev}L = \frac{\alpha L}{\sqrt{2\pi RT_s}}(p_{sat}(T_s) - p_v).
\end{aligned}
\tag{4.51}
$$

For the moment we assume $p_v = p_M$ to neglect the interference of the left and right propagating hyperbolic waves with the thermal wave at phase boundary. Then using the T_{ph} defined above, the last equation can be rewritten as

$$\kappa_r \frac{\partial T_r}{\partial x} - \kappa_l \frac{\partial T_l}{\partial x} = \frac{\alpha L}{\sqrt{2\pi RT_s}}(p_{sat}(T_s) - p_{sat}(T_{ph})).$$

115

For the asymptotic analysis, we can linearize the equation to be

$$\kappa_r \frac{\partial T_r}{\partial x} - \kappa_l \frac{\partial T_l}{\partial x} = [\frac{\alpha L}{\sqrt{2\pi R T_s}} \frac{\mathrm{d}p_{sat}}{\mathrm{d}T}|_{T_{ph}}](T_s - T_{ph}),$$

where the quantity in the square bracket can be regarded as a constant, which we denote by K.

The linearized thermal equation

$$\begin{aligned}
(\rho c_p)_l \frac{\partial T_l}{\partial t} &= \kappa_l \frac{\partial^2 T_l}{\partial x^2}, \\
(\rho c_p)_r \frac{\partial T_r}{\partial t} &= \kappa_r \frac{\partial^2 T_r}{\partial x^2},
\end{aligned}$$

with boundary condition

$$\begin{aligned}
T_l(t, x = 0) &= T_r(t, x = 0), \\
(\kappa_r \frac{\partial T_r}{\partial x} - \kappa_l \frac{\partial T_l}{\partial x})(t, x = 0) &= K(T_s(t) - T_{ph}), \quad\quad (4.52)
\end{aligned}$$

and initial condition $(T_l, T_r)(t = 0) = (T_{ML}, T_{MR})$ is solved numerically.

Figure 4.12 shows the solution to the normalized equation. All coefficients – $(\rho c_p)_l$, $(\rho c_p)_r$, κ_l, κ_r and K are set to 1. $T_{ML} = 1$, $T_{MR} = 0$. For $T_{ph} = 0.25$ between T_{ML} and T_{MR}, the interfacial temperature gradually decreases from $T_{ct} = 0.5$ to T_{ph}, as shown in Figure 4.12(a). It is interesting to note that even if $T_ph = -0.25$ is outside the range between T_{ML} and T_{MR}, T_s still evolves from T_{ct} to T_{ph}. It is also noted that the time needed for T_s to reach T_{ph} is infinitely long.

This result can be understood as following. As $t \to \infty$, the temperature
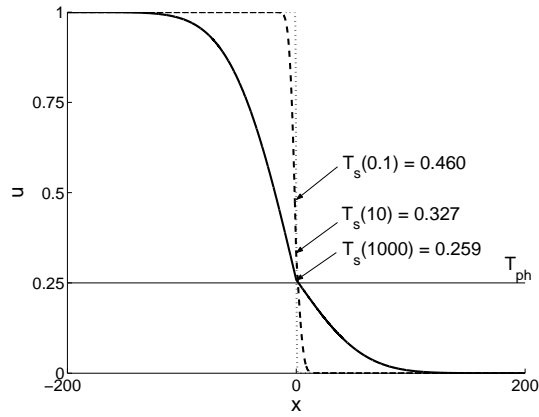
(a)
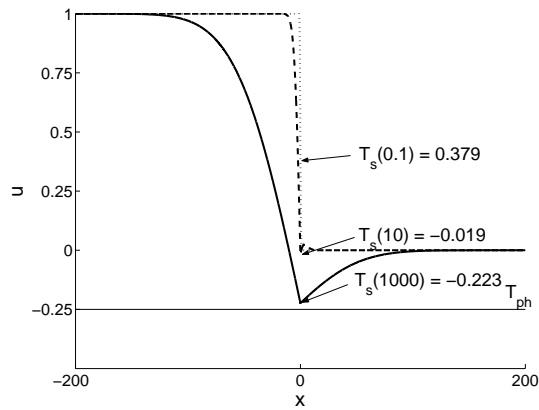
(b)

Figure 4.12: Solution to the linearized equation for large-time temperature in phase transitions. $(\rho c_p)_l = (\rho c_p)_r = 1$, $\kappa_l = \kappa_r = 1$. $K = 1$ in Eq. (4.52). $T_{ML} = 1$, $T_{MR} = 0$. (a) is the temperature distribution with $T_{ph} = 0.25$, (b) is the temperature with $T_{ph} = -0.25$. In both figures, dotted line is for $t = 0.1$, dashes line is for $t = 10$, and solid line is for $t = 1000$. For both settings the interfacial temperature T_s gradually approaches T_{ph} as time grows.

117

gradient on both sides of the interface approaches zero because the width of the thermal layer, $\sqrt{\nu t}$, grows unbounded. Therefore, the left side of Eq. (4.52) vanishes as $t \to \infty$, and so the right side vanishes, which means $T_s(\infty) = T_{ph}$. It also agrees with the physical picture. In out example, $T_{ph} < T_{ct}$, which is equivalent to $p_v < p_{sat}(T_{ct})$. The vapor is unsaturated, so the the liquid evaporates. The vapor pressure increases, meanwhile the interfacial temperature decrease due to the absorption of latent heat. As we will soon see, the change of vapor pressure doesn't play a crucial role. It is the decreasing interfacial temperature that slows down the evaporation. As t goes to infinity, the evaporation rate goes to zero, though it is always positive.

Lastly we show that the change of vapor pressure does not change the whole picture as we promised. Suppose the p_v in Eq. (4.51) is varying due to the interaction of the hyperbolic waves with the thermal wave at phase boundary. Figure 4.13 is the visualization of the discussion below. In the figure, points L and R are the left and right initial state. Vapor is supposed to be on the right side. The curve passing either point is the isentrope connected to the shock curve. The intersection point I is the mid state for contact. Without interaction, p_v stays at p_M and both left and right states stay at point I.

To the maximum extent of interaction, the vapor pressure would follow the mass flux to a new point on the curve passing R, for example, point A in Figure 4.13. Accordingly, the state at the liquid side of the phase boundary would shift to point B such that the pair (A,B) satisfies the Rankine-Hugoniot condition with the mass flux due to the deviation from Clausius-Clapeyron

118
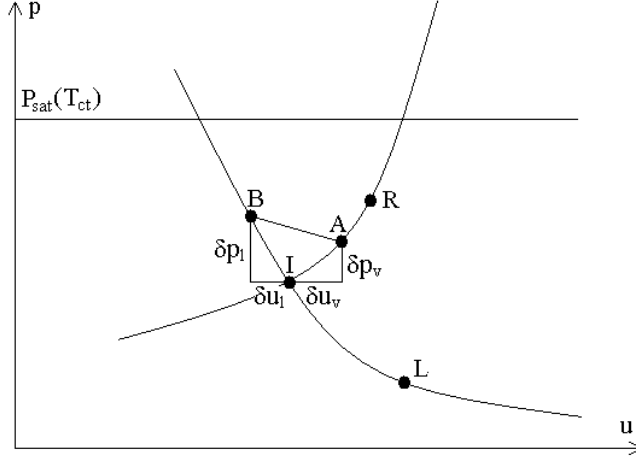
Figure 4.13: Schematic of the interaction between hyperbolic waves and the thermal wave at phase boundary. In the figure $p_{sat}(T_{ct}) > p_M$, which causes evaporation. The maximum hyperbolic effect would increase p_v by $\delta p_v \approx M_{ev} c_v$.

curve. The difference of point A and B from I is denoted by δp and δu in Figure 4.13. Since the slope of the curve is approximately ρc,

$$\delta p_v \approx \rho_v c_v \delta u_v.$$

where c_v is the vapor sound speed. Taking into account that $(\rho c)_l \gg (\rho c)_v$, Rankine-Hugoniot condition $\Delta u = M \Delta V$ gives

$$\delta u_v \approx \delta u_v + \delta u_l = M(V_v - V_l) \approx M V_v.$$

Combine the two equations we have

$$\delta p_v \approx \rho_v c_v M V_v = M c_v.$$

On the other hand, by Eq. (4.34)

$$\mu c_v M = p_{sat}(T_s) - p_v = p_{sat}(T_s) - p_M - \delta p_v,$$

where $\mu = \frac{1}{\alpha}\sqrt{\frac{2\pi}{\gamma}}$ is a dimensionless constant. The last two equation together gives

$$c_v M = \frac{p_{sat}(T_s) - p_M}{\mu + 1}.$$

Substituting the equation for M, Eq. (4.51) becomes

$$\kappa_r \frac{\partial T_r}{\partial x} - \kappa_l \frac{\partial T_l}{\partial x} = M_{ev} L = \frac{L}{(\mu + 1)c_v}(p_{sat}(T_s) - p_M).$$

The only difference from the original equation with p_v fixed is that μ is replaces by $\mu + 1$. Therefore, the effect of hyperbolic waves is no more than a reduced coefficient K. If the hyperbolic interaction is weaker, then the increment from μ would be less than 1. All in all, a smaller K only slows down the evolution of T_s to some extent, yet the conclusion that T_s approaches T_{ph} steadily is sustained. Furthermore, since δp_v is proportional to M_{ev}, it also goes to zero as $M_{ev} \to 0$, which means $p_v \to p_M$. Therefore the limit state is the same as without hyperbolic interaction too.

It is worth mentioning that this conclusion shows that the liquid temperature cannot be held to be constant for all time as in Section 4.4. Finally it should be pointed out that T_{ph} is allowed to be outside the range from T_{ML} to T_{MR} because the waves are propagating in an infinite domain. If the liquid and vapor, for example, are in an insulated container, then thermal equilibrium

will be reached after certain time. In general, the thermal effect eventually
dominates over the hyperbolic effect in isolated systems.

4.6.4 Wave Structure

Now that we have investigated both the short time behavior (isothermal
limit) and the large time behavior(adiabatic limit) of the Euler equations with
thermal conduction, we will discuss the global wave structure at all times. For
t much smaller than the characteristic time ν/c^2, thermal effect dominates
and the system is essentially isothermal. For t much larger than that, the
hyperbolic effect dominate and the system is essentially adiabatic. For time
in between, both effects are important.

- For $t \ll \nu/c^2$, $ct \ll \sqrt{\nu t}$ and the hyperbolic layer is an isothermal 3-wave
  structure embedded in the much wider thermal layer. The left and right
  waves propagate at the isothermal sound speeds, and they can be shocks
  or rarefactions. The mid state depends on whether the interface is the
  contact or the phase boundary. The isothermal waves propagate away
  from the interface and determine the size of the spikes at the shock fronts
  at later times.

- For $t \gg \nu/c^2$, $ct \gg \sqrt{\nu t} \gg \nu/c$ and the hyperbolic layer evolves into
  the 3-wave structure of the classical Riemann solution, left and right
  waves propagating at the adiabatic sound speeds. If the wave is a shock,
  there is a thermal layer of width about ν/c around the shock front, in
  which the deviation from the classical Riemann solution can be nonzero

in the limit of $t \to \infty$. If the wave is a rarefaction, the thermal layer can cover the entire rarefaction and the deviation vanishes in the limit of $t \to \infty$. There is no mass flux across the interface at large times for both the immiscible fluids and the phase transitions, and the thermal layer around the interface has the width of order $\sqrt{\nu t}$. The only difference between the two cases is in the interface temperature. For immiscible fluids it is between the temperature on the two sides of the contact, for phase transitions it is determined by the saturation condition.

- For intermediate times, $ct \approx \sqrt{\nu t} \approx \nu/c$ and the hyperbolic layer still have the 3-wave structure but it is neither isothermal nor adiabatic. The left and right waves propagate at varying speeds, which gradually shift from isothermal to adiabatic. As shown in Figure 4.2, the spikes at the left and right wave fronts overlap with each other and also with the thermal layer at the interface. As a result, the solution is far from being piecewise constant or rarefactions. It is not clear yet whether extra shocks could exist, good numerical algorithms may help to capture the detailed wave structure.

Chapter 5

Numerical Algorithm for the Simulation of Phase Transitions

The numerical algorithm for the heat conduction and phase transitions is based on the front tracking method. A key feature of front tracking is the avoidance of finite differencing across discontinuities fronts and thus the elimination of interfacial numerical diffusion. Phase boundary is tracked explicitly by a codimension one grid immersed in a regular spatial grid. The front propagates according to the dynamics around it (*i.e.* Lagrangian) while the regular spatial grid is fixed in time (*i.e.* Eulerian). In each time step, the front is first propagated with states on its two sides updated, then the interior states are updated using finite difference scheme.

Section 5.1 is the algorithm for interface propagation and front states update, and Section 5.2 describes the 2nd order finite difference update of the interior states. The numerical algorithm has been implemented into the Fron-Tier hydro code. In Section 5.3 we validated the numerical scheme by verifying the convergence of the simulation results to the analytical solution through

mesh refinement, we also illustrated the effectiveness of the thin thermal layer method. Lastly the numerical method was applied to the one dimensional condensation problem in Section 5.4.

5.1 Propagation of Phase Boundary

5.1.1 Normal Propagation

The phase boundary is first propagated in the normal direction. The characteristic form of the equations at the phase boundary has been given in Eqs. (4.12)–(4.15). Normal propagation solves a non-local Riemann problem. The original hyperbolic solver has three steps: slope reconstruction, prediction using a local Riemann solver, and correction by a nonlocal solver.

The first step in hyperbolic solver is kept. The second step has been modified as following. At the very first time step ($dt = 0$) or the time step when the phase boundary is dynamically created, the boundary states are set as described in Section 4.6.1. If the temperature is continuous across the phase boundary, nothing need to be done. Otherwise the interface temperature is calculated by solving the nonlinear Eq. (4.41) or using the approximate value in Eq. (4.44), while the density and velocity of the states on both sides of the interface are kept unchanged (the pressure, from EOS, changes accordingly), thus the left and right states become the point L and R in Figure 4.9. We could go further to solve the adiabatic Riemann problem exactly as described in Section 4.6.1, which requires extra iteration for phase transition. However, the lengthy procedure is skipped. The reason is that if the left and right

states were initialized as mid states in Figure 4.9 rather than the L and R states, the exact value of L and R states wouldn't be recovered in the finite difference update in the subsequent time steps due to the singularity of the temperature field at origin, thus the physical spikes at the shock fronts would be severely reduced. In fact, the current implementation not only gives more accurate height of the spikes, but also predicts the correct, though not exact, mid states from the linearized solver in the subsequent time steps. For all subsequent time steps, the interfacial pressure, velocity and temperature are forced to satisfy the required boundary conditions such as Rankine-Hugoniot condition and phase transition rate equation, so that the local Riemann solver does not change the states on either side of the interface. Therefore, the normal velocity of the phase boundary at the beginning of each time step is obtained from the beginning states directly, and the sound speeds needed for the slopes of characteristics are also directly from the beginning states on the two sides of the interface.

In the step of nonlocal solver, a discrete version of the characteristic system Eqs. (4.12)–(4.15) is solved. The phase boundary normal velocity obtained at the end of the time step is averaged with the value at the beginning of the time step and then used for the propagation of phase boundary.

To solve the characteristic system, the states at the feet of the traced back characteristics are first obtained by interpolation, usually of the conservative quantities, namely, mass, momentum and total energy density. The characteristic $\lambda_\pm = u \pm c$ and $\lambda_0 = u$, while the material interface move at $\sigma = u$ for contact and $\sigma = \Delta(\rho u)/\Delta\rho$ for phase transition. For small time step Δt, the

125
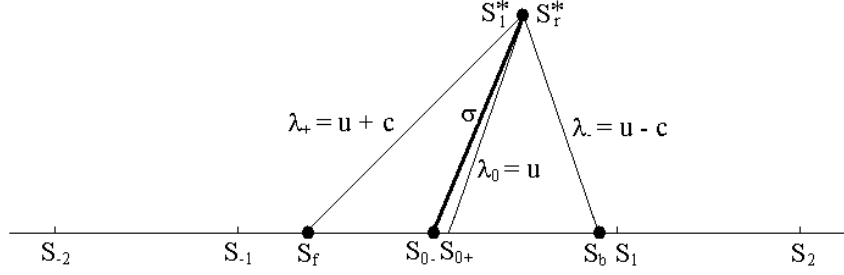
Figure 5.1: Five point stencil for the front normal propagation with thermal conduction. In each time step, the new front states S_l^* and S_r^* are calculated, and the front propagates normally.

characteristics are approximated by straight lines. Figure 5.1 is the schematic of the traced back characteristics. The left foot is $(c_l + u_l - \sigma)\Delta t$ away from the interface, while the right foot is $(c_r - u_r + \sigma)\Delta t$ away from the interface. For contact the foot of characteristic λ_0 coincides with the interface. But for phase transition it differs from the interface position, it could be on either side of the interface depending on the mass flux. However, since in most cases the phase transition rate is small enough such that

$$|u - \sigma| \ll c$$

on both sides of the interface, it doesn't make much difference to use $c_l \Delta t$ and $c_r \Delta t$ as the distance from the left and right feet to the interface. In the numerical implementation, the foot of λ_0 is also assumed to coincide with the interface for phase transition. Once we obtained the states at the characteristic feet by interpolation, we can integrate along the characteristics. Divided by

126

ρc and then integrated from t to $t + \Delta t$, Eqs. (4.12) and (4.13) become

$$\int_t^{t+\Delta t} \frac{\mathrm{d}p}{\mathrm{d}\lambda_+} \frac{d\lambda_+}{\rho c} + (u_l^* - u_f) + \alpha N_0 \int_t^{t+\Delta t} \frac{cu}{r} d\lambda_+$$
$$= -\int_t^{t+\Delta t} \frac{\partial \phi}{\partial \mathbf{n}} d\lambda_+ - \int_t^{t+\Delta t} \frac{\Gamma}{\rho c} (\frac{\partial q}{\partial \mathbf{n}} + \alpha N_0 \frac{q}{r}) d\lambda_+,$$
$$\int_t^{t+\Delta t} \frac{\mathrm{d}p}{\mathrm{d}\lambda_-} \frac{d\lambda_-}{\rho c} - (u_r^* - u_b) + \alpha N_0 \int_t^{t+\Delta t} \frac{cu}{r} d\lambda_-$$
$$= \int_t^{t+\Delta t} \frac{\partial \phi}{\partial \mathbf{n}} d\lambda_- - \int_t^{t+\Delta t} \frac{\Gamma}{\rho c} (\frac{\partial q}{\partial \mathbf{n}} + \alpha N_0 \frac{q}{r}) d\lambda_-. \qquad (5.1)$$

Neglecting the distance between the foot of the characteristic λ_0 and the interface, we have

$$\mathbf{u}_l'^* = \mathbf{u}_{0-}',$$

$$\mathbf{u}_r'^* = \mathbf{u}_{0+}',$$

where $\mathbf{u}'$ is the tangential velocity. We can also integrate the energy equation, however since it is a parabolic equation for temperature, the interface state is preferably determined by boundary condition rather than integration along λ_0. The boundary conditions depends on the interfacial dynamics. The case of contact is simpler, so we treat it first.

Contact with thermal conduction

The boundary conditions are

$$\Delta u = 0,$$

$$\Delta p + p_s = 0,$$

$$\Delta T = 0,$$

$$\Delta q = 0,$$

where p_s is the pressure jump due to surface tension, which is determined by the surface tension coefficient and the local curvature on the interface. The discrete characteristic equation along with the boundary condition can be solved in several ways. There are three methods implemented for the nonlocal hyperbolic Riemann solver, namely, RIEMANN, MOC+RH and CHEAP MOC+RH methods [21]. The RIEMANN method exploits the similarity between Eq. (5.1) and the local Riemann problem. It uses a local Riemann solver with S_f and S_b as initial left and right states to solve for the mid state. However it does not readily apply in our situation, because as pointed out in Section 4.6.4 the nonlocal wave structure is much more complicated than the local 3-wave structure. The other two methods approximate the the integrals in Eq. (5.1) by finite differences in time. The only difference between the them is that MOC+RH uses trapezoidal rule quadrature for the integration while CHEAP MOC+RH uses backward difference quadrature. In view of the various first order approximations already made at the interface, there would be little difference between the two methods. The following procedure

is analogous to the CHEAP MOC+RH method.

1. Starting from the usual five point stencil along the normal of the interface as shown in Figure 5.1. Let the grid size be Δn. First we determine the interfacial temperature. The boundary conditions

$$
\begin{aligned}
T_l^* &= T_r^* \\
\kappa_l \frac{T_l^* - T_{-1}}{\Delta n} &= \kappa_r \frac{T_1 - T_r^*}{\Delta n}
\end{aligned}
$$

give

$$
T_s := T_l^* = T_r^* = \frac{\kappa_l T_{-1} + \kappa_r T_1}{\kappa_l + \kappa_r}. \tag{5.2}
$$

2. Next we seek S_l^* and S_r^*. The difference equations are

$$
\begin{aligned}
&\frac{p_l^* - p_f}{\rho_f c_f} + (u_l^* - u_f) + \alpha N_0 \frac{c_f u_f}{r_f} \Delta t + (\phi_n')_f \Delta t \\
&= \frac{\Gamma_f}{\rho_f c_f} \kappa_l \left(\frac{T_{-2} + T_{0-} - 2T_{-1}}{\Delta n^2} + \alpha N_0 \frac{T_{0-} - T_{-1}}{r_f \Delta n} \right) \Delta t, \\
&\frac{p_r^* - p_b}{\rho_b c_b} - (u_r^* - u_b) + \alpha N_0 \frac{c_b u_b}{r_b} \Delta t - (\phi_n')_b \Delta t \\
&= \frac{\Gamma_b}{\rho_b c_b} \kappa_r \left(\frac{T_2 + T_{0+} - 2T_1}{\Delta n^2} + \alpha N_0 \frac{T_1 - T_{0+}}{r_b \Delta n} \right) \Delta t.
\end{aligned}
$$

Combined with $u_l^* = u_r^*$ and $p_l^* = p_r^* + p_s$, the pressure and velocity of S_l^* and S_r^* is readily solved. Finally the density of the states are determined from their EOS's with known pressure and temperature.

Phase transition

Next we treat the interfacial propagation for phase transition. The boundary conditions are

$$\Delta u = M\Delta V, \tag{5.3}$$

$$\Delta p + p_s = -M^2\Delta V, \tag{5.4}$$

$$\Delta T = 0, \tag{5.5}$$

$$\Delta q = -M_{ev}L, \tag{5.6}$$

$$M_{ev} = \frac{\alpha}{\sqrt{2\pi RT_s}}(p_{sat}(T_s) - p_v). \tag{5.7}$$

Since the interfacial temperature is coupled to the phase transition rate by kinetic theory, the temperature cannot be determined directly. Iteration over the vapor pressure p_v and the difference of specific volumes ΔV has been used. For clearness, we assume the vapor is on the right side.

1. Substituting the vapor pressure at S_{0+} for the p_v in Eq. (5.7) and discretizing Eq. (5.6), we have two equation for the two variable T_s and M_{ev}. The equations are

$$M_{ev}L = \kappa_r\frac{T_1 - T_s}{\Delta n} - \kappa_l\frac{T_s - T_{-1}}{\Delta n},$$

$$M_{ev} = \frac{\alpha}{\sqrt{2\pi RT_s}}(p_{sat}(T_s) - p_v).$$

The function p_{sat} is a nonlinear function, Newton's iteration or similar method is needed to solve the equations exactly. However, since this step itself is in the iteration of p_v and ΔV, we can linearize the Clausius-

Clapeyron equation at a reference temperature T_r and solve for T_s and M_{ev} while preserving the convergence of S_l^* and S_r^* through the iteration. For the first iteration step, T_r can be chosen to be the T_s at the beginning of the time step if $T_{0-} = T_{0+}$, or their average, for example, $(T_{0-}+T_{0+})/2$ if they are different. For subsequent iteration steps, T_r is simply the T_s obtained in the last iteration. Upon linearization,

$$T_s = \frac{\kappa_l T_{-1} + \kappa_r T_1 + \frac{\alpha}{\sqrt{2\pi R T_r}} L \Delta n (p_v - p_{sat}(T_r) + \frac{\mathrm{d}p_{sat}}{\mathrm{d}T}(T_r)T_r)}{\kappa_l + \kappa_r + \frac{\alpha}{\sqrt{2\pi R T_r}} L \Delta n \frac{\mathrm{d}p_{sat}}{\mathrm{d}T}(T_r)}, \qquad (5.8)$$

and

$$M_{ev} = \frac{\alpha}{\sqrt{2\pi R T_r}}(p_{sat}(T_r) - p_v + \frac{\mathrm{d}p_{sat}}{\mathrm{d}T}(T_r)(T_s - T_r)),$$

where $\frac{\mathrm{d}p_{sat}}{\mathrm{d}T}(T_r)$ is the slope of phase coexistence curve at T_r, which by Clausius-Clapeyron equation equals

$$\frac{\mathrm{d}p_{sat}}{\mathrm{d}T}(T_r) = \frac{L}{T_r(V_v(T_r, p_{sat}(T_r)) - V_l(T_r, p_{sat}(T_r)))}.$$

2. Having obtained the temperature and mass flux, we can solve the characteristic Eq. (5.1) with the Rankine-Hugoniot conditions Eqs. (5.3) and (5.4). For the first iteration the ΔV in Eqs. (5.3) and (5.4) is set to $V_{r0} - V_{l0}$. Then same as the last step for contact, the density ρ_l^* and ρ_r^* are determined from their EOS's with the pressure and temperature obtained in the iteration.

3. The last step in the iteration is to compare the newly obtained p_v and ΔV with the values used in the iteration. If the differences are within

the preset tolerance, then the iteration is over, otherwise update the p_v and ΔV for next iteration and go back to step 1.

In practice it is found that p_v and ΔV usually has relative error below 10^{-6} after 4 iterations. The convergence of p_v and ΔV guarantees the convergence of T_s, thus justifies the linearization of the Clausius-Clapeyron equation used in step 1.

5.1.2   Thin Thermal Layer Method

The method described above works well for fine grid, but when the grid is coarse as required by the physical problem or the computational capability, we have a numerical difficulty. For large Δn, the interface temperature given in Eq. (5.8) is approximately $T_{sat}(p_v)$, while in reality it should change gradually from the T_s given in Eq. (5.2) to $T_{sat}(p_v)$. The wrong interface temperature would in turn gives wrong temperature and pressure fields, especially in the liquid. To make it worse, even Eq. (5.2) gives wrong temperature if the thermal layer is narrower than the grid size, for which the correct interface temperature is close to

$$T_m = \frac{T_{-1}\sqrt{(\rho c_p \kappa)_l} + T_1\sqrt{(\rho c_p \kappa)_r}}{\sqrt{(\rho c_p \kappa)_l} + \sqrt{(\rho c_p \kappa)_r}}.$$

To illustrate it, let us consider a practical situation. For two dimensional simulation of bubbly water in a container of size $1cm$, suppose the grid size is $dx = 1\mu m$, which is already quite fine. The thermal layer in water is of width $\sqrt{\nu t}$ where $\nu = \kappa/(\rho c_p) = 1.5 \times 10^{-6}cm^2/ms$, and the time step restricted by

CFL condition is $dt = dx/c = 6.7 \times 10^{-7} ms$. So it requires

$$\frac{dx^2}{\nu dt} = 10^4$$

time steps for the thermal layer to expand to a grid cell. For all these time steps, it is inappropriate to use simple finite difference for the temperature gradient at the interface. More details are given in Section 5.3.

To solve the Euler equations with reasonable accuracy in a coarse grid, we need to represent the thermal layer in certain way. A widely used method is the spectral method [24, 30, 2], where the temperature field is spanned by Chebychev polynomials and the evolution is solved by Galerkin method or collocation method. However, spectral method has several drawback. First, it has been only used for spherical problems where the temperature field can be spanned by single variable polynomials, while our goal is to develop direct numerical simulation scheme in arbitrary geometry. Moreover, the coordinate of vapor in $(0, R_{bub}]$ is normalized to $(0, 1]$ for the variable in the polynomials, while the coordinate of liquid is normalized from $[R_{bub}, \infty)$ to $(0, 1]$, which cannot be carried out for the multi bubble system we intend to simulate. Secondly, for the spectral method the temperature field is always separated from the pressure and velocity waves – in vapor uniform pressure is assumed, and in liquid the thermal expansion coefficient is set to zero. The evolution of the pressure field does not depend on temperature either – it is either the Rayleigh-Plesset equation for incompressible fluid or the Keller equation for weakly compressible fluid. So the temperature and pressure can be solved

on different grids or in different solution spaces. As a contrast, for the fully compressible fluid we simulate, they have to be solved simultaneously on a common grid. Spectral method, even if it worked efficiently, would invoke a difficult problem for mapping the temperature field from the polynomial expansion form to the fixed grid while preserving the accuracy.

As a result, we hereby present a different method that incorporates the thermal layer into the finite difference scheme when necessary. The idea is simple. When the thermal layer is thinner than a grid cell, then the temperature profile should take the form of Eq. (4.37). For clarity, we consider the phase on the right side of the interface and rewrite the equation with slight changes in notation,

$$T = T_M + (T_R - T_M)\text{erf}(\frac{x}{\sqrt{4\nu t}}).$$

Since the thermal layer is thinner than the grid size dx, the temperature T_1 one grid cell away from the interface should be approximately T_R. Taking derivative over x at the origin in the equation above, we have

$$\left(\frac{\partial T}{\partial x}\right)_0 = (T_R - T_M)\frac{2}{\sqrt{\pi}}\frac{1}{\sqrt{4\nu t}} \approx \frac{T_1 - T_M}{\sqrt{\pi\nu t}}.$$

Therefore the temperature gradient at the interface is better approximated by $(T_1 - T_M)/\sqrt{\pi\nu t}$ than $(T_1 - T_M)/dx$. Considering the approximate nature of the argument, we used $\epsilon\sqrt{\nu t}$ instead of $\sqrt{\pi\nu t}$ in the implementation, where ϵ is a number of order 1 to be optimized by numerical experiment. When $\epsilon\sqrt{\nu t}$ is larger than dx, the thermal layer can be regarded as wider than a

134

grid cell, so we can revert to the usual finite difference approximation for the temperature gradient. As a summary, the temperature gradient at the interface is approximated by

$$\left(\frac{\partial T}{\partial x}\right)_0 \approx \frac{T_1 - T_M}{dx^*} := \frac{T_1 - T_M}{\min(\epsilon\sqrt{\nu t}, dx)}, \tag{5.9}$$

where dx^* is defined to $\min(\epsilon\sqrt{\nu t}, dx)$. Numerical experiment found $\epsilon = 1$ is a good choice in general, so ϵ is set to 1 by default. Admittedly the uncertainty of ϵ makes the method ad-hoc, however as we will see in Section 5.3 it works quite well in spite of its simplicity. It should be emphasized that the t in the formulas is the time since the interface in created rather than the global time if the bubbles are created dynamically as in [22].

When the thin layer modification is applied to the normal front propagation, all interfacial heat flux in the form of $\kappa\Delta T/\Delta n$ should be replaced by $\kappa\Delta T/\Delta n^*$ with the ν in the corresponding phase. For example, Eq. (5.2) should be replaced by

$$T_s = \frac{\frac{\kappa_l}{\Delta n_l^*}T_{-1} + \frac{\kappa_r}{\Delta n_r^*}T_1}{\frac{\kappa_l}{\Delta n_l^*} + \frac{\kappa_r}{\Delta n_r^*}},$$

where $\Delta n_l^* = \min(\epsilon\sqrt{\nu_l t}, \Delta n)$ and $\Delta n_r^* = \min(\epsilon\sqrt{\nu_r t}, \Delta n)$. Eq. (5.8) changes similarly, and so does the heat flux at interface in the characteristic equations. Another point need to be mentioned is that throughout the analysis on thin thermal layer, the temperature gradient away from the interface in either phase has been assumed to be zero. In the general situation that the gradients don't vanish, the T_1 in Eq. (5.9) for thin thermal layer is not close to T_R (the interface temperature with thermal conduction neglected). Rather, T_1 in Eq.

(5.9) should be replaced by the appropriate approximation of T_R, which is given by the extrapolation $2T_1 - T_2$. The left side of the interface should be handled accordingly to give the correct temperature and heat flux on the interface. For example, the correct form of Eq. (5.2) is

$$T_s = \frac{\frac{\kappa_l}{\Delta n_l^*}(2T_{-1} - T_{-2}) + \frac{\kappa_l}{\Delta n}(T_{-2} - T_{-1}) + \frac{\kappa_r}{\Delta n_r^*}(2T_1 - T_2) + \frac{\kappa_r}{\Delta n}(T_2 - T_1)}{\frac{\kappa_l}{\Delta n_l^*} + \frac{\kappa_r}{\Delta n_r^*}}.$$

In the later sections, the numerical technique introduced here will be referred to as the thin (thermal) layer method.

5.1.3 Tangential Propagation

The normal propagation of the front solves the Euler equations projected onto the normal direction. After that the Euler equations projected onto the tangent space are solved on both sides of the front. Along the tangential direction(s),

$$
\begin{aligned}
\frac{\partial \rho}{\partial t} + \frac{\partial \rho u}{\partial \boldsymbol{\tau}} + \alpha N_1 \frac{\rho u}{r} &= 0, \\
\frac{\partial \rho u}{\partial t} + \frac{\partial (\rho u^2 + p)}{\partial \boldsymbol{\tau}} + \alpha N_1 \frac{\rho u^2}{r} &= -\rho \frac{\partial \phi}{\partial \boldsymbol{\tau}}, \\
\frac{\partial \rho \mathbf{u}'}{\partial t} + \frac{\partial \rho u \mathbf{u}'}{\partial \boldsymbol{\tau}} + \alpha N_1 \frac{\rho u \mathbf{u}'}{r} &= 0, \\
\frac{\partial \rho E}{\partial t} + \frac{\partial (\rho E + p)u}{\partial \boldsymbol{\tau}} + \alpha N_1 \frac{(\rho E + p)u}{r} &= -\frac{\partial q}{\partial \boldsymbol{\tau}} - \alpha N_1 \frac{q}{r},
\end{aligned}
$$

where $\boldsymbol{\tau}$ is the tangential direction of the interface in two-dimensional problem or one of the tangential directions in three-dimensional problem. u and $\mathbf{u}'$ are the tangential velocity along $\boldsymbol{\tau}$ and the velocity components perpendicular to

$\boldsymbol{\tau}$. q is the tangential heat flux. N_1 is the x component of the $\boldsymbol{\tau}$.

The tangential equations are solved using the finite difference scheme described in the next section. The only difference between tangential state update and interior state update is that the N_1 for interior update is either 0 or 1. After the tangential propagation, the states on the two sides of the front are changed, so the Rankine-Hugoniot conditions, temperature continuity and the equations about heat flux and phase transition rate could be violated. An extra normal propagation with $\Delta t = 0$ after the tangential propagation solves the problem.

5.2   Finite Difference Update of Interior States

After the front propagation and update of front states, the interior states on the spatial grid need to be time updated. Since the heat conduction does not involve cross derivatives in space, we can still use directional splitting as in the current implementation. The advantage of weaving the parabolic terms into the hyperbolic step rather than after it is that the accuracy of the scheme is boosted from 1st order to 2nd order in time.

The shock capturing methods currently implemented in FronTier for one-dimensional sweeps include Lax-Wendroff method, Lax-Friedrichs method, Collela piecewise linear method and a second order monotone upwind scheme for conservation laws (MUSCL) scheme developed by Van Leer and adapted for FronTier by I-L. Chern. MUSCL scheme is similar to the piecewise parabolic method described in [11], and a detailed description can be found in [10]. The two-pass implementation currently being used in FronTier, namely,
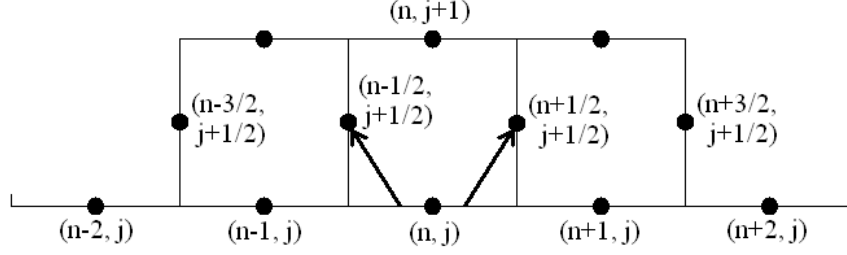
Figure 5.2: Finite difference update of interior state with thermal conduction.

first *regular* cells then *irregular* cells update, is well documented in [21]. Here we will use MUSCL as an example to demonstrate the addition of parabolic corrections. The emphasis is on the change from the original scheme.

In MUSCL, the gas states are first linearly reconstructed then propagated for half time step by characteristic method. With heat conduction added, the linear reconstruction step is the same while the changes of the Riemann invariants along the characteristics have additional source terms from heat conduction. The explicit formulas are

$$
\begin{aligned}
\frac{\mathrm{d}p}{\mathrm{d}\lambda_+} + \alpha_i \frac{\rho c^2 u}{x_i} + \rho c \frac{\mathrm{d}u}{\mathrm{d}\lambda_+} &= -\rho c \frac{\partial \phi}{\partial x_i} - \Gamma(\frac{\partial q}{\partial x_i} + \alpha_i \frac{q}{x_i}), \\
\frac{\mathrm{d}p}{\mathrm{d}\lambda_-} + \alpha_i \frac{\rho c^2 u}{x_i} - \rho c \frac{\mathrm{d}u}{\mathrm{d}\lambda_-} &= \rho c \frac{\partial \phi}{\partial x_i} - \Gamma(\frac{\partial q}{\partial x_i} + \alpha_i \frac{q}{x_i}), \\
\frac{\mathrm{d}\mathbf{u}'}{\mathrm{d}\lambda_0} &= 0, \\
\frac{\mathrm{d}e}{\mathrm{d}\lambda_0} + p\frac{\mathrm{d}V}{\mathrm{d}\lambda_0} &= -\frac{1}{\rho}(\frac{\partial q}{\partial x_i} + \alpha_i \frac{q}{x_i}).
\end{aligned}
$$

To evaluate the thermal terms, centered finite difference scheme has been used for the heat flux and its derivative.

As shown in Figure 5.2, during the half time step update of cell (n, j),

138

the Riemann invariant along right-going characteristics to point $(n + \frac{1}{2}, j + \frac{1}{2})$ and along left-going characteristics to point $(n - \frac{1}{2}, j + \frac{1}{2})$ both have thermal source term proportional to

$$-\left(\frac{\partial q}{\partial x_i} + \alpha_i \frac{q}{x_i}\right).$$

For medium satisfying Fourier's Law of conductivity, $q = -\kappa \frac{\partial T}{\partial x_i}$. We need to estimate $\frac{\partial^2 T}{\partial x_i^2}$ and also $\frac{\partial T}{\partial x_i}$ in cylindrical or spherical geometry. They are simply given by

$$
\begin{aligned}
\frac{\partial^2 T}{\partial x_i^2}(n, j) &= \frac{T(n+1, j) - 2T(n, j) + T(n-1, j)}{dx^2}, \\
\frac{\partial T}{\partial x_i}(n, j) &= \frac{T(n+1, j) - T(n-1, j)}{2dx},
\end{aligned}
$$

where dx is the grid size.

After the Riemann solver step at half time step, finite volume method is used to update the conservative quantities, namely, mass, momentum and energy. Accordingly thermal source terms should also so added, and the terms should be calculated using the states at half time step to guarantee 2nd order accuracy in time. The thermal source term is nonzero only for the energy conservation law in Eq. (4.11) and it is $-\left(\frac{\partial q}{\partial x_i} + \alpha_i \frac{q}{x_i}\right)$. The heat flux and its

139

derivative are approximated by

$$q(n, j + \frac{1}{2}) = -\kappa \frac{T(n + \frac{1}{2}, j + \frac{1}{2}) - T(n - \frac{1}{2}, j + \frac{1}{2})}{dx},$$

$$\frac{\partial q}{\partial x_i}(n, j + \frac{1}{2}) = \frac{q(n + \frac{1}{2}, j + \frac{1}{2}) - q(n - \frac{1}{2}, j + \frac{1}{2})}{dx} =$$

$$-\kappa \frac{T(n + \frac{3}{2}, j + \frac{1}{2}) - T(n + \frac{1}{2}, j + \frac{1}{2}) - T(n - \frac{1}{2}, j + \frac{1}{2}) + T(n - \frac{3}{2}, j + \frac{1}{2})}{2dx^2}.$$

Notice that in order to update on grid cell, four half time step states are needed compared to the two states in original hyperbolic MUSCL scheme. Therefore in the vectorized version of MUSCL, the half step need to be carried out for two more points, one at each end.

Lastly it should be pointed out that because the scheme is forward in time, the time step is subject to both the hyperbolic (CFL) restriction and the parabolic restriction. The hyperbolic restriction is

$$\Delta t < \frac{\Delta x}{c_{max}},$$

and the parabolic restriction is

$$\Delta t < \frac{1}{2}\frac{\Delta x^2}{\nu_{max}} = \frac{1}{2}\frac{\Delta x^2}{(\frac{\kappa}{\rho c_v})_{max}}.$$

In fact, the time step should satisfy

$$2\frac{\Delta t}{\Delta x^2}\nu_{max} + \frac{\Delta t}{\Delta x}c_{max} < 1.$$

5.3 Validation

5.3.1 Comparison with Analytical Solutions

First we verified the convergence of the numerical solution to the analytical solution in Section 4.3.2. The temperature field is decoupled from the hyperbolic fields. The initial conditions and parameters are given in Eqs. (4.31) and (4.32) respectively. The numerical scheme was linearized accordingly. Figure 5.3 shows the comparison of the numerical solutions of grid size 0.1 and 0.01 with the analytical solutions. The convergence is clearly verified.

We also verified the convergence of numerical solution to the analytical solution in Section 4.4, where the hyperbolic fields are decoupled from the temperature field. Initial conditions and parameters are the same as in Figure 4.7 except that $\kappa_l = 0.01$ and $\kappa_r = 0.02$. Figure 5.4 compares the temperature field from linearized numerical scheme with grid size 0.1 and 0.01 to the analytical solution. The convergence is verified again.

5.3.2 Thin Thermal Layer Method

In this section we demonstrate the effect of the thin thermal layer method in a coarse grid. To understand whether a grid is regarded as fine or coarse, we rewrite Eq. (5.8) using the thin layer method and the linearized Clausius-Clapeyron equation,

$$T_s = \frac{\frac{\kappa_l}{\Delta n_l^*} T_{-1} + \frac{\kappa_r}{\Delta n_r^*} T_1 + \frac{\alpha}{\sqrt{2\pi R T_r}} L \frac{\mathrm{d}p_{sat}}{\mathrm{d}T} T_{sat}(p_v)}{\frac{\kappa_l}{\Delta n_l^*} + \frac{\kappa_r}{\Delta n_r^*} + \frac{\alpha}{\sqrt{2\pi R T_r}} L \frac{\mathrm{d}p_{sat}}{\mathrm{d}T}}. \tag{5.10}$$
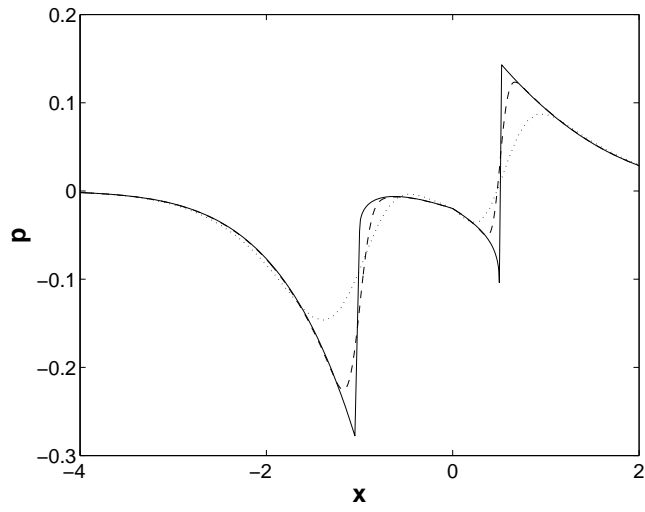
(a)
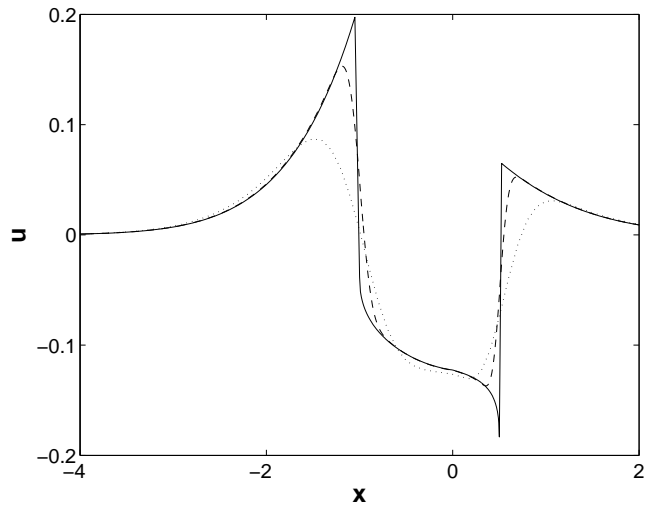
(b)

Figure 5.3: Convergence of the pressure and velocity fields obtained numerically to the analytical solutions for decoupled temperature field. Initial conditions and parameters are given in Eqs. (4.31) and (4.32). (a) is $p(x)$ at $t = 1$, (b) is $u(x)$ at $t = 1$. In both figures, dotted line is for grid size $dx = 0.1$, dashed line is for $dx = 0.01$, solid line is the analytical solution.

142
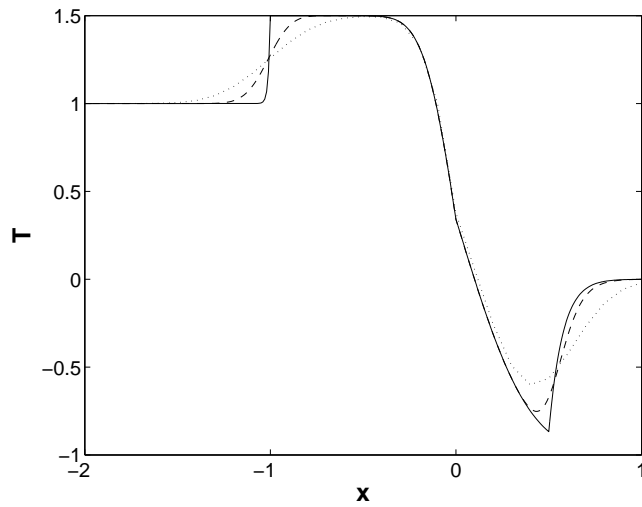
Figure 5.4: Convergence of the T field obtained numerically to the analytical solutions for decoupled hyperbolic fields. $(\beta T, \rho c_p, c, m)_l = (1, 1, 1, 1)$, $(\beta T, \rho c_p, c, m)_r = (1, 0.5, 0.5, 1)$, $\kappa_l = 0.01$, $\kappa_r = 0.02$. Initial conditions are $(p_{l0}, u_{l0}, T_{l0}) = (0, 0, 1)$, $(p_{r0}, u_{r0}, T_{r0}) = (1, 0, 0)$. Plotted is the T at $t = 1$. Dotted line is for grid size $dx = 0.1$, dashed line is for $dx = 0.01$, solid line is the analytical solution.

The criterion for the fineness of the grid is that the Δn^* in the equation above can be replaced by Δn without making much difference. We focus on the gas(vapor)-liquid interface. Since the thermal diffusivity of gas(vapor) is usually much larger than that of liquid, the thermal layer in the gas(vapor) is wider than a grid cell for most of the time.

First we consider gas-liquid interface without phase transition. To obtain an accurate temperature field at earlier time such that $\sqrt{\nu_l t} \ll \Delta n$, the grid is coarse and thin layer method is needed, while for later time such that $\sqrt{\nu_l t} \gg \Delta n$, the grid is fine enough so that the thin layer method doesn't make much difference. On the other hand, the pressure field can be calculated with reasonable precision without thin layer method even for earlier time. The reason is that the heat flux on the vapor side can be calculated quite accurately due to the thickness of the vapor thermal layer relative to the grid size, and the heat flux is continuous across the contact, so that the pressure filed, mainly dependent on the interface heat flux rather than interface temperature, can be obtained accurately without an accurate temperature field.

Next we turn to the more complicated problem with phase transition. Here we have an extra length scale from the interfacial dynamics. If

$$\frac{\kappa_{liq}}{\Delta n} \gg \frac{\alpha}{\sqrt{2\pi RT}} L \frac{\mathrm{d}p_{sat}}{\mathrm{d}T},$$

Eq. (5.10), which clearly is an interpolation, wouldn't change much if Δn is replaced by a smaller Δ^*. In other word, the criterion for the fineness of the

144

grid is

$$\Delta n \ll \kappa_{liq} \frac{\sqrt{2\pi RT}}{\alpha L} \frac{\mathrm{d}T_{sat}}{\mathrm{d}p} \doteq \kappa_{liq} \sqrt{2\pi RT} \frac{TV_{vap}}{\alpha L^2}.$$

For water at 20^oC, using the thermodynamic coefficients listed in Appendix A, the right hand side of the formula above is $4\mu m$. If the criterion is not satisfied, the grid is coarse for the calculation of both the temperature and pressure fields at earlier time. The thin layer method improves the accuracy of the simulation by a lot, as illustrated by the example below.

We consider the realistic phase transition between water and water vapor at room temperature 20^oC. The vapor is on the left side, and the EOS parameters are set as in Appendix A. Assume initially both phases are at rest, and have the same temperature(20^oC) and pressure. Initially, the vapor is superheated by 1^oC, which means

$$T_v - T_{sat}(p_v) = 1^oC.$$

The metastable liquid evaporates, which induces a couple of thermal and pressure waves – the interface cools down and vapor heats up, the vapor pressure increases, and there is a mass flux into the vapor, etc. The numerical solutions at $5\mu s$ are plotted in Figure 5.5 and Figure 5.6. The solution from three simulations are shown, namely, $\Delta n = 10\mu m$, $\Delta n = 1\mu m$ and $\Delta n = 0.2\mu m$. Recalling the grid fineness criterion from interfacial dynamics, the case $\Delta n = 10\mu m$ can be regarded as coarse grid, $\Delta n = 0.2\mu m$ the fine grid, while $\Delta n = 1\mu m$ is intermediate. The phase boundary has moved negligible distance in $5\mu s$.

Figure 5.5 is the numerical solution obtained *without* using the thin layer

(a)

(b)

(c)
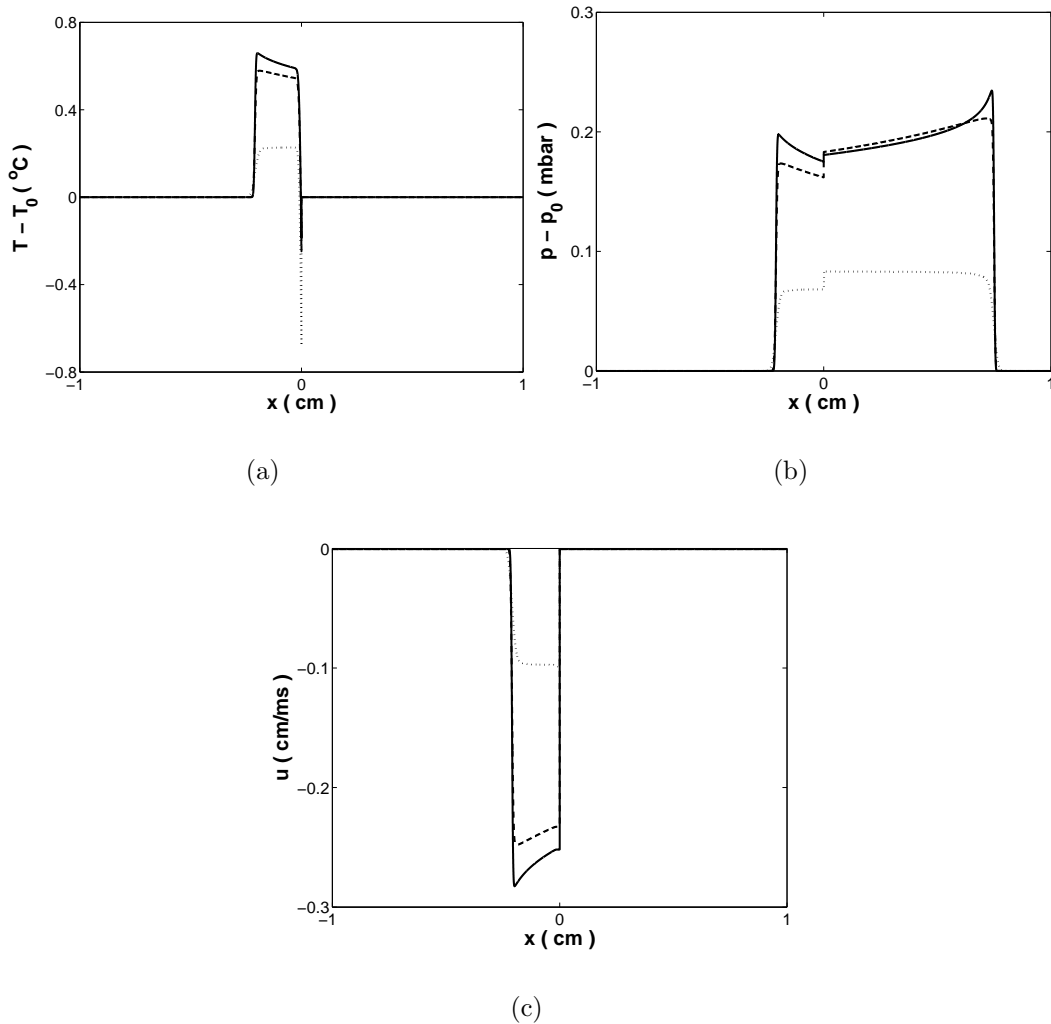
Figure 5.5: Numerical solution to the problem with Riemann data with phase transition between water and water vapor. Initially conditions are $T_0 = 20^o C$, $T_{sat}(p_0) = 19^o C$ and $u_0 = 0$, where both phases have the same T, p and u. Plotted is the solution at $5\mu s$ from direct simulation *without* using thin layer method. (a) is $T(x)$, (b) is $p(x)$, and (c) is $u(x)$. In all figures, the dotted curve is from the simulation with $\Delta n = 10\mu m$, the dashed curve with $\Delta n = 1\mu m$, and the solid curve with $\Delta n = 0.2\mu m$.

146

(a)

(b)

(c)
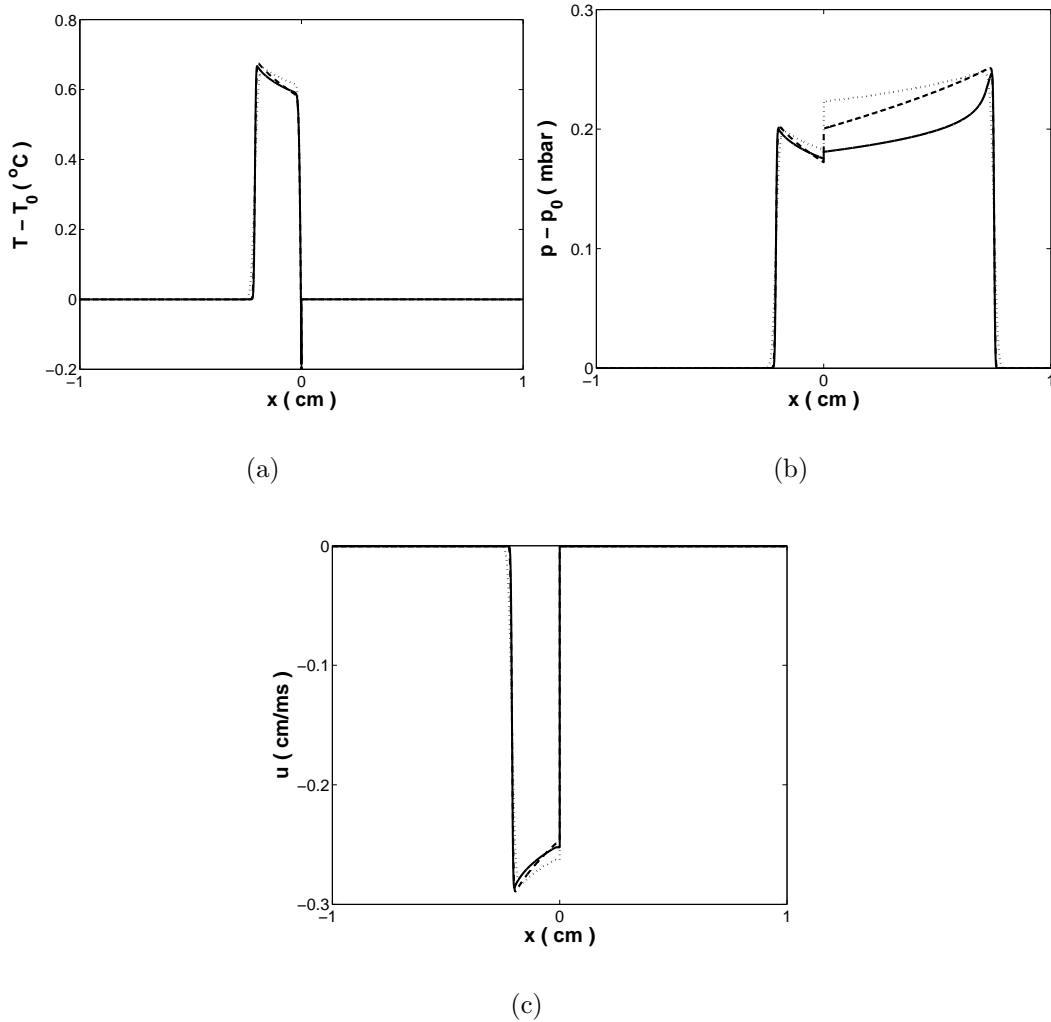
Figure 5.6: Numerical solution to the problem with Riemann data with phase transition between water and water vapor. Initial conditions are the same as in Figure 5.5. Plotted is the solution at $5\mu s$ from direct simulation *with* thin layer method. (a) is $T(x)$, (b) is $p(x)$, and (c) is $u(x)$. In all figures, the dotted curve is from the simulation with $\Delta n = 10\mu m$, the dashed curve with $\Delta n = 1\mu m$, and the solid curve with $\Delta n = 0.2\mu m$.

method, while Figure 5.6 is obtained *with* thin layer method. The solid curves $(\Delta n = 0.2\mu m)$ have been compared with the simulation of $\Delta n = 0.4\mu m$ and the convergence was verified, so we can approximately take the solid curves to be the exact solutions to which other numerical solutions should converge. We notice the solid curves of the corresponding temperature, pressure and velocity fields in both figures are almost the same, which is natural since the liquid thermal layer is thin relative to the grid only for a period much short than $5\mu s$. It is easy to see that the fields obtained on coarser grids in Figure 5.5 deviate severely from the exact solution, though the convergence by mesh refinement is also clear.

As a contrast, the solutions on coarser grid shown in Figure 5.6 is almost the same as the exact solution. The only exception to the observation above is the liquid pressure at intermediate grid size $\Delta n = 1\mu m$. It maybe argued that the liquid pressure of the dashed line in Figure 5.5(b) is closer to the exact solution than that in Figure 5.6(b). However, it is more like a coincidence since the convergence of the vapor pressure is just the opposite. Increasing the ϵ in Eq. (5.9) could make the liquid pressure closer to the exact solution, but meanwhile deviate the vapor pressure from the exact value. More delicate numerical scheme might help to resolve the issue. As a summary, the thin thermal layer method, in spite of its crudeness, boost the accuracy of the numerical solution at coarse grid significantly.

148

5.4   Application to One Dimensional Condensation

We used the numerical method to simulate the one dimensional condensation problem. The early-stage build-up of the temperature field has been demonstrated. The late-stage condensing flow was compared to the exact steady states and the convergence was confirmed. The one-dimensional problem consists of a vertical tube containing a shallow layer of water with height $0.05mm$. The bottom of the tube is in contact with colder material to sustain a constant outgoing heat flux. The remaining space is filled with water vapor. Initially the water and water vapor are at rest and in equilibrium at room temperature – $T_0 = 20^oC$, $p_0 = 23.4$mbar. The outgoing heat flux from water gradually builds up a temperature gradient in the water and causes condensation. For the boundary conditions at the opening of the tube, the vapor pressure is assumed to be constant and the temperature gradient is assumed to be zero. Mathematically, the equations for the liquid and vapor states are the Euler equation with thermal conduction, and interface conditions is the Rankine-Hugoniot conditions plus interfacial dynamics of phase transition with evaporation coefficient set to 0.4. The boundary conditions are

$$
\begin{aligned}
\left(\frac{\partial T}{\partial x}\right)_{x=0} &= 0, \\
p(x=0) &= p_0, \\
\left(\frac{\partial T}{\partial x}\right)_{x=D} &= T_{x0}, \\
u(x=D) &= 0,
\end{aligned}
$$

149
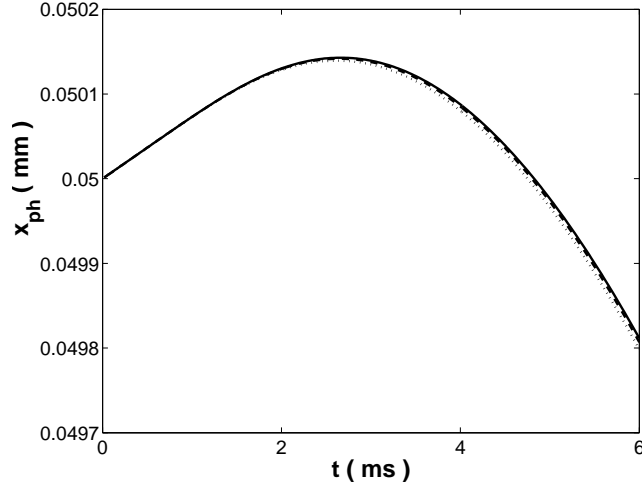
Figure 5.7: The position of phase boundary in the first $6ms$. $T_0 = 20^oC$, $p_0 = 23.4$mbar, $T_{x0} = -2.5^oC/\mu m$. x_{ph} first increases due to the thermal contraction and later decreases due to condensation. The solid line is from the simulation with grid size $1\mu m$, the dashed line is with grid size $2\mu m$, the dotted line is with grid size $4\mu m$.

where D is the total length of the liquid and vapor in the calculation. Since the vapor state is virtually uniform, the length of vapor layer doesn't affect the results. In the calculation D is chosen to be $0.1mm$ so that initially the computational domain is half filled with water. $x = D$ is the bottom of the tube and $x = 0$ is vapor end. In the following example, $T_{x0} = -2.5^oC/\mu m$. The EOS parameters and the thermal conductivities are set as in Appendix A for room temperature.

5.4.1 Early Stage

The simulation was carried out using the numerical methods developed in the previous sections. The grid resolution was $1\mu m$. The position of the

150

phase boundary x_{ph} calculated from the simulation was plotted against the time $0 < t < 6ms$ in Figure 5.7. It shows that the phase boundary first moves to the the right, then back to the left. In other words, before the liquid volume increases due to the condensation, it first decreases for about $2.7ms$. The reason is that the liquid shrinks with the lowering temperature when the heat flux required for the phase transition has not been built up. It is not until about $t = 4.8ms$ that the phase boundary moves back to the original position. After that the phase transition dominates over thermal contraction of the liquid and the phase boundary moves steadily to the left.

5.4.2 Late Stage

The liquid height increases during the condensation, while the thermal and pressure waves in the tube gradually approaches the "steady state" dictated by the boundary conditions and liquid height. The "steady state" is quoted because it is not a single state, but rather a series of states depending on the liquid height that is changing with time. The steady states can be found as following. Since $T_x(x = 0) = 0$, the steady state of vapor is uniform. Combined with the fact that the mach number of the phase transition in the example is less than 0.1 for the vapor and even smaller for the liquid, the steady temperature field in liquid is given by Eq. (4.49) except that the x there should be replaced by $x - x_{ph}$, where x_{ph} is the location of the phase boundary.

$$T(x) = T_s + \frac{L}{c_p}(1 - \exp(\frac{Mc_p(x - x_{ph})}{\kappa})).$$

(5.11)

151

At the bottom of the tube ($x = D$) the exponent $Mc_p(D - x_{ph})/\kappa$ is about 0.2, which is small but not negligible. So $\frac{\partial T}{\partial x}$ is not uniform, and the transition rate M of the steady state should be obtained by solving

$$\left(\frac{\partial T}{\partial x}\right)_{x=D} = -\frac{LM}{\kappa} \exp(\frac{Mc_p(D - x_{ph})}{\kappa}) = T_{x0}.$$

From M the interface temperature can be found from kinetic relation with the known vapor pressure p_0. The variation of the pressure in the liquid is negligible compared to the pressure jump at the phase boundary. The steady state liquid pressure is given by

$$p_l = p_v + M^2 \Delta V \doteq p_0 + M^2 V_v.$$

The liquid velocity is 0 at $x = D$ as dictated by the boundary condition, hence the velocity of the phase boundary is

$$u_{ph} = -MV_l|_D \doteq -MV_{l0}(1 + \beta(T|_D - T_0)),$$

where the effect of pressure variation on density has been neglected. The vapor velocity is

$$u_v = MV_v + u_{ph} \doteq MV_v.$$

Since the phase boundary is moving, all the quantities above vary with time.

Table 5.1 is the comparison between the steady state quantities and the corresponding ones in the evolving wave obtained from numerical simulation. It can be seen from the table that the evolving state is closer to the steady

$t(ms)$	10		20		30	
$x_{ph}(mm)$	0.04874		0.04464		0.03991	
state	actual	steady	actual	steady	actual	steady
$M(10^{-5}g/cm^2 \cdot ms)$	3.61	5.10	4.74	5.04	4.958	4.968
$T_s(^oC)$	14.09	11.65	12.24	11.75	11.880	11.865
p_l(mbar)	23.48	23.56	23.535	23.552	23.5475	23.5481
$u_{ph}(10^{-5}cm/ms)$	-3.31	-4.97	-4.58	-4.90	-4.818	-4.822
$u_v(cm/ms)$	2.16	3.06	2.84	3.02	2.975	2.981

Table 5.1: Comparison of the actual states from simulation with the corresponding steady states at various times. The steady state depends on the interface position at time t. The grid resolution of the simulation is $1\mu m$.

state at later time. Figure 5.8 visualizes the evolution. From the figure we see the pressure and velocity jumps at the phase boundary increase steadily toward the values of steady states.

The temperature field plotted in Figure 5.8(a) is particularly interesting. The temperature gradient is approximately constant in the steady state, so the solid curve ($t = 30ms$) in Figure 5.8(a) should be roughly a straight line as it is. However, if looked at carefully, one might notice it is not exactly a straight line. In fact we can show the curvature of the temperature field matches excellently with the nonlinearity revealed in Eq. (5.11). In order to see the nonlinearity of the temperature distribution, define

$$y = \ln(1 + \frac{c_p}{L}(T_s - T)).$$

From Eq. (5.11), for steady state

$$y_{st} = \frac{Mc_p}{\kappa}(x - x_{ph}). \tag{5.12}$$

153

(a)

(b)

(c)
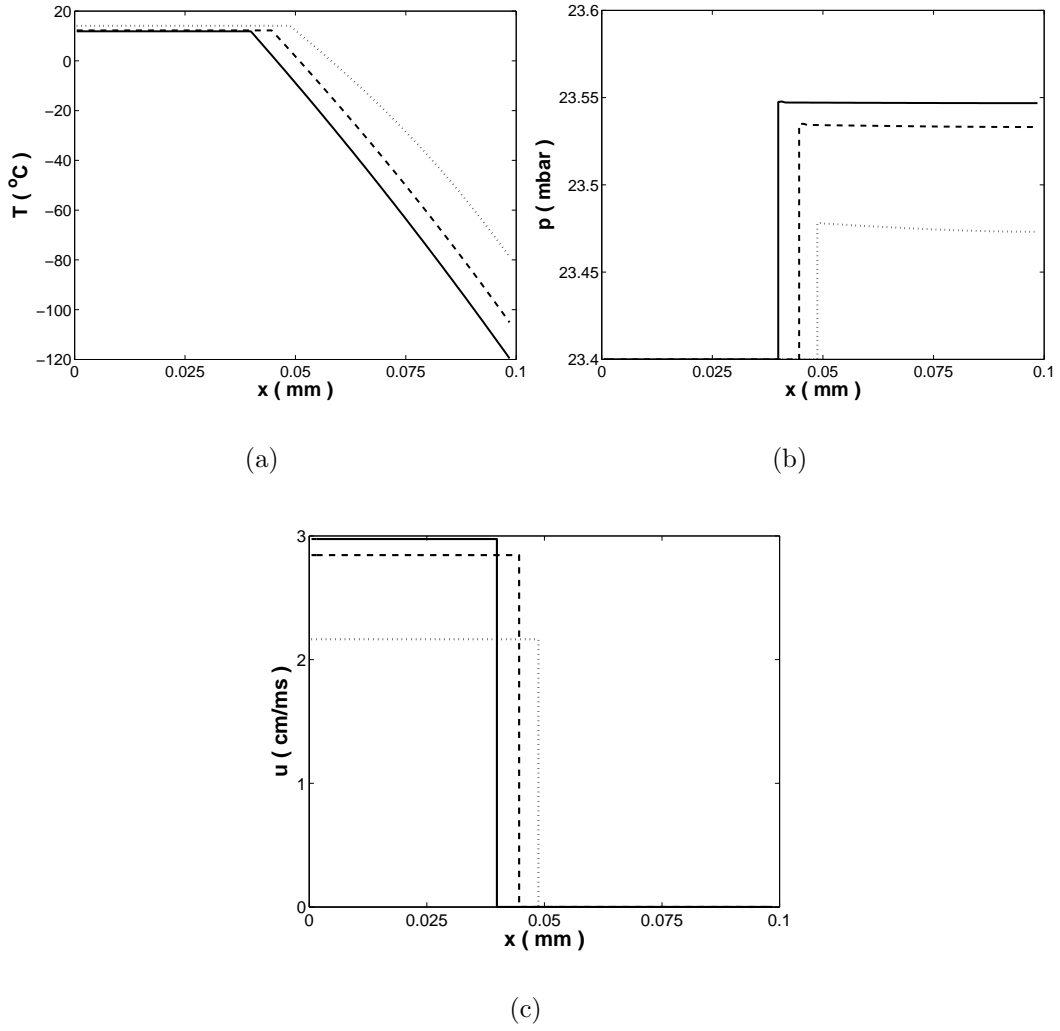
Figure 5.8: Late-stage condensing flow. $T_0 = 20^oC$, $p_0 = 23.4$mbar, $T_{x0} = -2.5^oC/\mu m$. (a) is $T(x)$, (b) is $p(x)$, and (c) is $u(x)$. In all figures, the dotted curve is for $T = 10ms$, the dashed curve for $t = 20ms$, and the solid curve for $t = 30ms$. The grid size of the simulation was $1\mu m$.
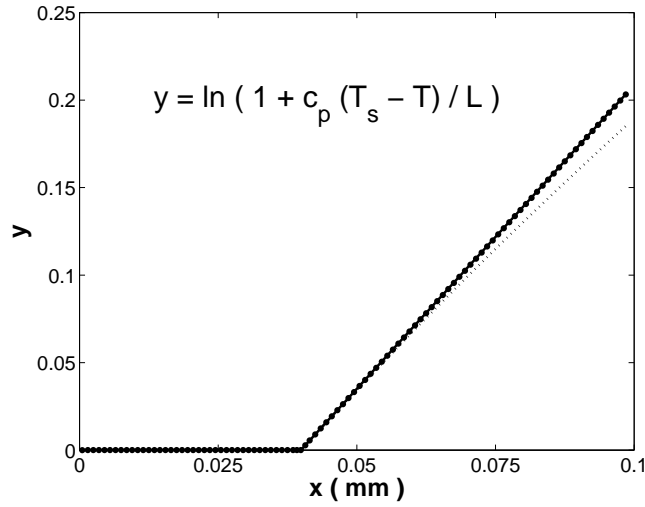
Figure 5.9: Match of the nonlinearity between the temperature from simulation at $t = 30ms$ and the steady state temperature distribution. The solid line is plot of y_{st} in Eq. (5.12). The dots are the discretized values of y from simulation. The dotted line line the plot of y if the temperature gradient were constant. Obviously the actual T at $t = 30$ is much closer to Eq. (5.11) than a linear distribution.

In the above two equations, thermodynamical parameters c_p and κ are both for the liquid. Using the T_s at $t = 30$, the discretized value of y from simulation can be calculated. y_{st} and the y from simulation are compared in Figure 5.9. The match is almost perfect. It indicates the state at $t = 30$ is close to the steady state not only in general profile but also in fine details.

Finally the mesh refinement check for the late-stage solutions is shown in Figure 5.10. All the curves are very close to each other, the temperature field obtained at the three grid resolutions are particularly indistinguishable in Figure 5.10(a).

(a)

(b)

(c)
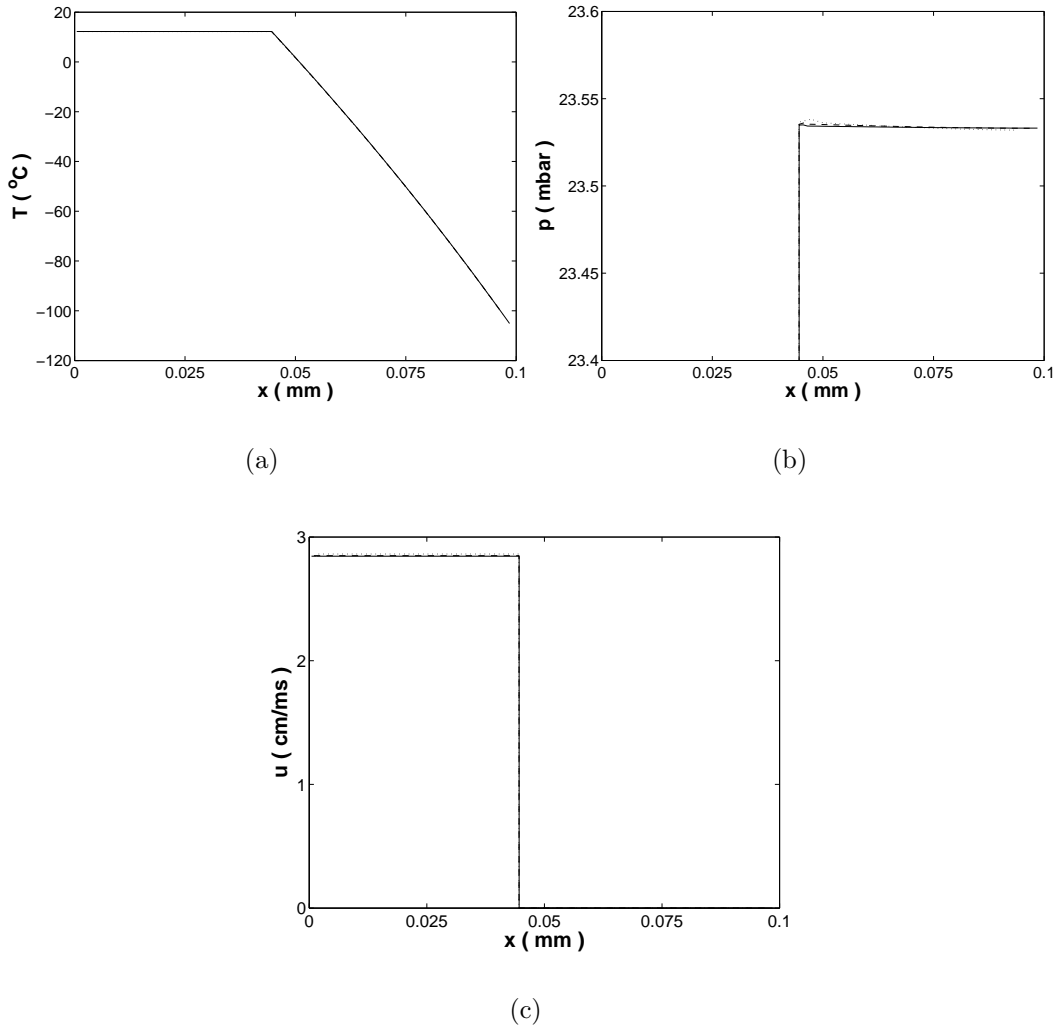
Figure 5.10: Mesh refinement check for $t = 20ms$. (a) is $T(x)$, (b) is $p(x)$, and (c) is $u(x)$. In all figures, the dotted curve is from the simulation of grid resolution $4\mu m$, the dashed curve is of grid resolution $2\mu m$, and the solid curve is of grid resolution $1\mu m$.

Chapter 6

Conclusion

6.1   DNS of Bubbly Flows and Application

Through the comparison of numerical simulations with experiments and theoretical predictions on the propagation of acoustic and shock waves in bubbly fluids, the direct approach to the simulation of bubbly flows using the method of front tracking and the FronTier code has been validated. This method is potentially very accurate in treating many physical effects in bubbly flows, such as drag, surface tension, viscosity, and the phase transition induced mass transfer. It has a variety of current and prospective applications, such as Rayleigh-Taylor instability [18, 28] and cavitating flows.

The pressure wave relaxation in bubbly mercury in the SNS target has been investigated numerically using the FronTier hydro code. The estimation of cavitation bubble collapse pressure under periodic ambient pressure has been carried out systematically. The efficiency of the mitigation of overall cavitation damage by the injection of bubbles has been calculated. The overall cavitation damage has been found to be reduced by more than an order of

magnitude through the injection of gas bubbles with volume fraction of order 1%. Therefore the use of layers of non-dissolvable gas bubbles as a pressure mitigation technique to reduce the cavitation erosion has been confirmed.

6.2   Interfacial Dynamics of Phase Transitions

The interfacial dynamics of phase transitions has been investigated along with the case without mass flux. The rate of the non-equilibrium phase transitions is proportional to the deviation of vapor pressure from the Clausius-Clapeyron equation. Analytical solutions to the linearized equations have been explored. Physical spikes have been observed on the wavefronts, whose height and width were calculated exactly for linearized equations. The spikes persist for linearized equations but appear to vanish for nonlinear equations as time increases. The 3-wave structure coupled to the thermal layers in the adiabatic and isothermal limits has been clarified. The reason for the lack of a clear wave structure in the intermediate time has also been discussed. The analytical travelling wave solutions have been found and shown to exist only on finite domain dictated by the stability condition.

A numerical scheme for solving the Euler equations with thermal conduction and phase transitions has been implemented in the frame of front tracking. Heat conduction has been added to the interior state update with second order accuracy. Phase boundary propagation has been handled according to the interfacial dynamics. A numerical technique has been introduced to account for the thermal layer thinner than a grid cell. The algorithm and the thin layer method have been validated by showing their convergence to the analytical

solution (or fine grid solution if analytical solution is unknown) through mesh refinement. The scheme has also been extended to multi-dimension, adapted to cylindrical and spherical symmetry, and applied to sample physical problems such as the simulation of boiling and cavitating processes.

Appendix A

Parameters for Stiffened Polytropic EOS

A.1 Thermodynamic Identities

Following is the definition of a few thermodynamic quantities.

$$
\begin{aligned}
c_p &:= T \left(\frac{\partial S}{\partial T} \right)_p, \\
c_v &:= T \left(\frac{\partial S}{\partial T} \right)_V, \\
K_T &:= -\rho \left(\frac{\partial V}{\partial p} \right)_T, \\
K_S &:= -\rho \left(\frac{\partial V}{\partial p} \right)_S, \\
\beta &:= \frac{1}{V} \left(\frac{\partial V}{\partial T} \right)_p, \\
c^2 &:= \left(\frac{\partial p}{\partial \rho} \right)_S,
\end{aligned}
$$

where c_p and c_v are the specific heat with fixed pressure and fixed volume respectively. K_T and K_S are the isothermal and isentropic compressibility. β is the coefficient of thermal expansion and c is the adiabatic sound speed.

There are several thermodynamic identities for them that will be used for the setting of the EOS parameters.

$$
\begin{aligned}
c_p &= \frac{\beta V}{\Gamma K_S}, \\
c_v &= \frac{\beta V}{\Gamma K_T}, \\
c_p - c_v &= \frac{\beta V}{K_T}\beta T.
\end{aligned}
\tag{A.1}
$$

Number of free parameters

Take Gibbs energy G as example. The second law of thermodynamics gives

$$
dG = V\,dp - S\,dT.
$$

We are concerned about the specific Gibbs energy in the vicinity of a point (p_0, T_0) in the $p - T$ plane. Expand G in p and T up to second order,

$$
\begin{aligned}
G(p, T) \;\doteq\;& G(p_0, T_0) + V(p - p_0) - S(T - T0) + \frac{1}{2}\left(\frac{\partial V}{\partial p}\right)_T (p - p0)^2 \\
&+ \left(\frac{\partial V}{\partial T}\right)_p (T - T_0)(p - p_0) - \frac{1}{2}\left(\frac{\partial S}{\partial T}\right)_p (T - T0)^2,
\end{aligned}
$$

where V, S and all partial derivatives are evaluated at (p_0, T_0). The three partial derivatives are related to K_T, β and c_p respectively. The value of G in the vicinity of (p_0, T_0) is determined up to the second order by six quantities – K_T, β, c_p, V, S and G at (p_0, T_0). The first four are well defined physically, while the last two can be shifted by arbitrary constants. If the EOS's of the two phases are required to be consistent at the phase coexistence curve, then

the specific Gibbs energy in both phases must be equal at the curve.

$$0 = \Delta G = \Delta E + p\Delta V - T\Delta S \Rightarrow \Delta E = T\Delta S - p\Delta V = L - p\Delta V, \quad (A.2)$$

where $L = T\Delta S$ is the latent heat of phase transitions. Therefore, in order
for the EOS to be accurate up to the second order expansion near (p_0, T_0) and
consistent with phase transitions, four parameters associated with K_T, β, c_p,
V and one auxiliary parameter associated with L are needed. The Stiffened
Polytropic EOS introduced below has exactly five parameters to accommodate
the requirement.

As for the γ-law gas or the so-called POLY EOS implemented in FronTier,
$K_T = p^{-1}$, $\beta = T^{-1}$, and the specific internal energy E has definite physical
meaning. So the five parameters reduce to two parameters, as there are in the
POLY EOS, namely, R and γ.

A.2   Liquid and Vapor EOS's

Throughout the thesis the liquid is described by the stiffened polytropic
(SPOLY) EOS, while the vapor is considered as γ-law gas, or equivalently, the
polytropic (POLY) EOS. SPOLY EOS is a simple, analytical approximation
to an arbitrary EOS, obtained by local fitting pressure, density, temperature
and the first derivatives [36]. It has two defining equations,

$$p + \gamma p_\infty = (\gamma - 1)\rho(E + E_\infty),$$
$$RT = (p + p_\infty)V + (\gamma - 1)E_t\rho^{\gamma-1}.$$

Other thermodynamic quantities such as entropy can be derived from them. There are five parameters in the equations, namely, γ, R, p_∞, E_∞ and E_t. Since E_t is usually negative, for convenience we will denote $-E_t$ by Q. And it is easy to derive that

$$R = c_v(\gamma - 1).$$

In the implementation, the five parameters are γ, c_v, p_∞, E_∞ and Q. Using Eq. (A.1), it is straightforward to derive the following formulas for the thermodynamic quantities K_T, β, c_p in terms of these parameters,

$$
\begin{aligned}
\frac{1}{K_T} &= p + p_\infty + (\gamma - 1)^2 Q V^{-\gamma}, \\
\frac{1}{\beta} &= T + \frac{\gamma}{c_v} Q V^{1-\gamma}, \\
c_p &= c_v + \beta R T,
\end{aligned}
$$

or inversely, the formulas for the EOS parameters in terms of the thermodynamic quantities K_T, β, c_p and V at (p, T),

$$
\begin{aligned}
c_v &= c_p - \frac{\beta^2 V T}{K_T}, \\
\gamma &= 1 + \frac{\beta V}{K_T c_v}, \\
Q &= V^{\gamma-1} \frac{c_v}{\gamma} \frac{1 - \beta T}{\beta}, \\
p_\infty &= \frac{1}{K_T} - (\gamma - 1)^2 Q V^{-\gamma} - p. \quad \text{(A.3)}
\end{aligned}
$$

If phase transitions are not involved, the auxiliary parameter E_∞ can be

set arbitrarily, for example,

$$E_\infty = E_\infty^0 = \frac{(p + \gamma p_\infty)V}{\gamma - 1} \tag{A.4}$$

to make E vanish at (p, T). Otherwise E should satisfy Eq. (A.2), so to be consistent with the vapor EOS,

$$E_\infty = E_\infty^{ph} = \frac{(p + \gamma p_\infty)V}{\gamma - 1} + L - (E_v + p(V_v - V_l)). \tag{A.5}$$

The POLY EOS has two parameters γ_v and R_v, and the equations are

$$E = \frac{pV}{\gamma_v - 1},$$
$$R_v T = pV.$$

The parameters are determined by the molecular mass (R_v) and structure (γ_v).

A.3 Numerical Examples

A.3.1 Single liquid phase

The thermodynamic quantities and SPOLY parameters for water at $20^o C$ and $100^o C$ under 1 bar pressure are listed in the following table. The units are cm, ms, g, bar, $^o C$ and their combinations. The thermodynamic quantities are

$p(bar)$	$T(^oC)$	$V(cm^3/g)$	$c_p((cm/ms)^2/K)$	$k_T^{-1}(10^3bar)$	$\beta^{-1}(10^3K)$
1	20	1.002	41.8	21.8	4.79
1	100	1.043	42.2	20.1	1.32

the sound speeds in the two cases are 148 and 153 (cm/ms) respectively. All quantities can be found in standard physical and chemical handbooks. Using Eqs. (A.3) and (A.4), the appropriate SPOLY parameters for water are

γ	$c_v((cm/ms)^2/K)$	$p_\infty(10^3bar)$	$Q(10^3bar(cm^3/g)^\gamma)$	$E_\infty^0(10^3(cm/ms)^2)$
1.11	41.5	19.8	168	200
1.42	37.7	15.8	25.6	55.7

A.3.2 Both phases near equilibrium

For water and water vapor near equilibrium at 20^oC and 100^oC, the thermodynamic quantities and EOS parameters are listed below. The saturation pressure at those temperatures are 0.0234 and 1.013 bar respectively. The thermodynamic quantities for water are virtually the same as those in the previous examples. So the only different parameter in the SPOLY EOS for water is the E_∞, which should be set to E_∞^{ph} as in Eq. (A.5). So we will only list the two parameters of the POLY EOS for water vapor and the E_∞^{ph} for water. The thermodynamic quantities are

$T(^oC)$	$P_{sat}(bar)$	$L(10^3(cm/ms)^2)$	$V_v(10^3cm^3/g)$
20	0.0234	24.5	57.8
100	1.013	22.6	1.67

The EOS parameters are

165

$R_v((cm/ms)^2/K)$	γ_v	$E_\infty^{ph}(10^3(cm/ms)^2)$
4.61	1.33	219
4.54	1.33	71.5

The γ_v in the table is defined to be c_p/c_v of water vapor (for vapor at higher temperature $c_v > R/(\gamma - 1)$).

As a reference, the thermal conductivity throughout the thesis is $5.98 \times 10^{-5} gcm^4/(ms^3 K)$ for water and $1.82 \times 10^{-6} gcm^4/(ms^3 K)$ for water vapor.

Bibliography

[1] Status report on mercury target development and related issues. Report No. SNS-101060100-TR0006-R00, Spallation Neutron Source Project, July 2002.

[2] C. E. Brennen A. Preston, T. Coloius. Toward efficient computation of heat and mass transfer effects in the continuum model for bubbly cavitating flows. *CAV2001*, session B4.002, 2001.

[3] T. Alty and C. A. Mackay. The accommodation coefficient and the evaporation coefficient of water. *Proc. R. Soc. London, Ser. A*, 149:104–116, 1935.

[4] A. E. Beylich and A. Gülhan. On the structure of nonlinear waves in liquids with gas bubbles. *Phys. Fluids A*, 2(8):1412–1428, 1990.

[5] C. E. Brennen. *Cavitation and bubble dynamics*. Oxford University Press, 1995.

[6] R. E. Caflisch, M. J. Miksis, G. C. Papanicolaou, and L. Ting. Effective equations for wave propagation in bubbly liquids. *J. Fluid Mech.*, 153:259–273, 1985.

[7] S. L. Ceccio and C. E. Brennen. Observations of the dynamics and acoustics of travelling bubble cavitation. *J. Fluid Mech.*, 233:633–660, 1991.

[8] R. B. Chapman and M. S. Plesset. Thermal effects in the free oscillation of gas bubbles. *ASME J. Basic Eng.*, 93:373–376, 1971.

[9] N. Chodes, J. Warner, and A. Gagin. A determination of the condensation coefficient of water from the growth rate of small cloud droplets. *J. Atmos. Sci.*, 31:1351, 1974.

[10] P. Collela. A direct eulerian muscl scheme for gas dynamics. *SIAM J. Sci Stat. Comput.*, 6(1):104–117, 1985.

[11] P. Collela and P. Woodward. The piecewise parabolic method (ppm) for gas-dynamics. *J. Comput. Phys.*, 54:174–201, 1984.

[12] K. W. Commander and A. Prosperetti. Linear pressure waves in bubbly liquids: Comparison between theory and experiments. *J. Acoust. Soc. Am.*, 85(2):732–746, 1989.

[13] Y. Kuhn de Chizelle, S. L. Ceccio, and C. E. Brennen. Observations and scaling of travelling bubble cavitatio. *J. Fluid Mech.*, 293:99–126, 1995.

[14] H. Fan and M. Slemrod. Dynamic flows with liquid/vapor phase transitions. In S. Friedlander and D. Serre, editors, *Handbook of Mathematical Fluid Dynamics*, volume 1. North-Holland, 2002.

[15] R. D. Finch and E. A. Neppiras. Vapor bubble dynamics. *J. Acoust. Soc. Am.*, 53:1402–1410, 1973.

[16] F. E. Fox, S. R. Curley, and G. S. Larson. Phase velocity and absorption measurements in water containing air bubbles. *J. Acoust. Soc. Am.*, 27(3):534–539, 1955.

[17] J. P. Garnier, Ph. Ehrhard, and Ph. Mirabel. Water droplet growth study in a continuous flow diffusion cloud chamber. *Atmos. Res.*, 21:41–52, 1987.

[18] J. Glimm, J. Grove, X. L. Li, W. Oh, and D. H. Sharp. A critical analysis of rayleigh-taylor growth rates. *J. Comput. Phys.*, 169:652–677, 2001.

[19] J. Glimm, J. Grove, X. L. Li, and D. C. Tan. Robust computational algorithms for dynamic interface tracking in three dimensions. *SIAM J. Sci. Comput.*, 21:2240–2256, 2000.

[20] J. Glimm, J. Grove, B. Lindquist, O. A. McBryan, and G. Tryggvason. The bifurcation of tracked scalar waves. *SIAM J. Sci. Statist. Comput.*, 9:61–79, 1988.

[21] J. Glimm, J. Grove, and Y. Zhang. Interface tracking for axisymmetric flows. *SIAM J. Sci. Comput.*, 24(1):208–236, 2002.

[22] J. Glimm, M. N. Kim, X. L. Li, R. Samulyak, and Z. L. Xu. Jet simulation in a diesel engine. *MIT Conf. on Comp. Fluid and Solid Mechanics (submitted)*, 2004.

[23] D. E. Hagen, J. Schmitt, M. Trueblood, J. Carstens, D. R. White, and D. J. Alofs. Condensation coefficient measurement for water in the umr cloud simulation chamber. *J. Atmos. Sci.*, 46:803, 1989.

[24] Y. Hao and A. Prosperetti. The dynamics of vapor bubbles in acoustic pressure fields. *Phys. Fluids*, 11(8):2008–2019, 1999.

[25] S. Hatamiya and H. Tanaka. A study on the mechanism of dropwise condensation. *Tras. Jpn. Soc. Mech. Eng. (in Japanese)*, 52(477B):2214, 1986.

[26] R. Hickling and M. S. Plesset. Collapse and rebound of a spherical bubble in water. *Phys. Fluids*, 7(1):7–14, 1964.

[27] D. Y. Hsieh. Some analytical aspects of bubble dynamics. *J. Basic Engineering*, 87:991–1005, 1965.

[28] H. Jin, X. F. Liu, T. Lu, B. Cheng, J. Glimm, and D.H. Sharp. Rayleigh-taylor mixing rates for compressible flow. *Phys. Fluids*, 17:024104, 2005.

[29] D. Juric and G. Tryggvason. Computation of boiling flows. *Int. J. Multiphase Flow*, 24:387–410, 1998.

[30] V. Kamath and A. Prosperetti. Numerical integration methods in gas-bubble dynamics. *J. Acoust. Soc. Am.*, 85:1538–1548, 1989.

[31] J. B. Keller and I. I. Kolodner. Damping of underwater explosion bubble oscillations. *J. Appl. Phys.*, 27:1152–1161, 1956.

[32] J. B. Keller and M. J. Miksis. Bubble oscillations of large amplitude. *J. Acoust. Soc. Am.*, 68:628–633, 1980.

[33] R. Levy and M. Shearer. Kinetics and nucleation for driven thin film flow. *Physica D (submitted)*, 2005.

[34] J. D. Macpherson. The effects of gas bubbles on sound propagation in water. *Proc. Phys. Soc. London*, B70:85–92, 1957.

[35] Y. Matsumoto and F. Takemura. Influence of internal phenomena on gas bubble motion. *JSME International Journal*, B37:288–296, 1994.

[36] R. Menikoff and B. J. Plohr. The riemann problem for fluid flow of real materials. *Reviews of Modern Physics*, 61(1):75–130, 1989.

[37] M. S. Plesset and S. A. Zwick. The growth of vapor bubbles in superheated liquids. *J. Appl. Phys.*, 25:493–500, 1954.

[38] A. Prosperetti, L. A. Crum, and K.W. Commander. Nonlinear bubble dynamics. *J. Acoust. Soc. Am.*, 83:502–514, 1988.

[39] A. Prosperetti and A. M. Lezzi. Bubble dynamics in a compressible liquid. part 1. first-order theory. *J. Fluid Mech.*, 168:457–478, 1986.

[40] A. Prosperetti and M. S. Plesset. Vapor bubble growth in a superheated liquid. *J. Fluid Mech.*, 85:349–368, 1978.

[41] Lord Rayleigh. On the pressure developed in a liquid during the collapse of a spherical cavity. *Phil Mag.*, 34:94–98, 1917.

[42] E. Silberman. Sound velocity and attenuation in bubbly mixtures measured in standing wave tubes. *J. Acoust. Soc. Am.*, 29(8):925–933, 1957.

[43] Z. H. Teng, A. J. Chorin, and T. P. Liu. Riemann problems for reacting gas, with applications to transition. *SIAM J. Appl. Math*, 42(5):964–981, 1982.

[44] M. Watanabe and A. Prosperetti. Shock waves in dilute bubbly liquids. *J. Fluid Mech.*, 274:349–381, 1994.

[45] S. W. Welch. Local simulation of two-phase flows includind interface tracking with mass transfer. *J. Comp. Phys.*, 121:142–154, 1995.

[46] L. Van Wijngaarden. One-dimensional flow of liquids containing small gas bubbles. *Ann. Rev. Fluid Mech.*, 4:369–396, 1972.